Effect of non-axisymmetric casing on flow and performance of an axial turbine

Thesis submitted for the degree of

Doctor of Philosophy

at the University of Leicester

by

Hakim T. K. Kadhim

Department of Engineering

University of Leicester

2018

Effect of non-axisymmetric casing on flow and performance of an axial turbine

Hakim T. K. Kadhim

Advances in computer based optimization techniques can be used to enhance the efficiency of energy conversions processes, such as by reducing the aerodynamic loss in thermal power plant turbomachines. One viable approach for reducing this flow energy loss is by endwall contouring. This thesis implements a design optimization workflow for the casing geometry of a 1.5 stage axial flow turbine, towards mitigating secondary flow losses.

In this thesis, a new non-axisymmetric endwall design method for the stator casing is implemented through a novel surface definition that draws from observations of the typical secondary flow pattern over the casing. The new casing design technique focuses on manipulating specific flow structures directly while also influencing the surrounding pressure field. This approach is tested on a three-dimensional axial turbine RANS model built in OpenFOAM Extend 3.2, with k-ω SST turbulence closure. Computer-based optimization of the surface topology is demonstrated towards automating the design process. This is implemented using Automated Process and Optimization Workbench (APOW) software. The designs are optimized using the total pressure loss across the full stage as the target function. The optimization and its sensitivity analysis give confidence that a good predictive ability is obtained by the Kriging surrogate model used in the prototype design process.

The casing surface parametrization was shown to produce topologically smooth interfaces with the rest of the passage geometry. This was achieved by using the Beta distribution function to design a smooth casing groove path, which is a first application of the Beta distribution function to the contouring of a turbomachine casing. The flow analysis confirms the positive impact of the optimized casing groove design on the turbine isentropic efficiency compared to a reference diffusion based endwall design and compared to the benchmark axisymmetric design, at design and at off design conditions.

Acknowledgements

I would like first to express my deepest thanks and sincere gratitude to my supervisor, Dr. Aldo Rona, who guided, with friendly patience, the development of this work. His advice and constructive criticism helped the investigation and the writing up of this thesis. I would like also to thank Emeritus Prof. J. Paul Gostelow and Dr. Katrin Leschke for their support and invaluable advices. I am grateful to Dr. Shian Gao for being my co-supervisor.

My appreciation goes to my colleagues and to all staff of the department of engineering, especially to the Computational Engineering & Control Research Group, for their help and their support during my research.

This thesis has been undertaken under the auspices of the GE & Alstom Energy - University of Leicester framework agreement. I would like to acknowledge the support and advices from Dr. N. Z. Ince and Dr Mark Willetts from the methods and tools group, GE Power.

I would like to thank the Higher Committee for Education Development in Iraq (HCED) for financially supporting the project by the award number D1201303.

The supply of experimental data for the 1.5 stage axial flow turbine "Aachen Turbine" under license by RWTH Aachen is gratefully acknowledged.

Finally, I am indebted so much to my parents, my sister and my brothers who have supported me for a long time. Then I would like to thank my dearest wife and my daughter for the support and encouragement I received through the course of my research.

Hakim T. Kadhim

Contents

Nomenclature

English Symbols

a	Inflated blade distance / m
c	Chord / m
C_{Pts}	Stator row total pressure loss coefficient
C_{Ptr}	Stage total pressure loss coefficient
C_{ske}	Secondary kinetic energy coefficient
C_{Pt}	Total pressure loss coefficient
c_x	Chord fraction
D_i	Inflated blade profile on casing surface / m
d_p	Cubic spline interpolation along the pressure side
d_s	Cubic spline interpolation along the suction side
f	Beta probability density function
g	Polynomial function of degree 4
h	Blade span / m
h_o	Groove depth / m
L_1	Upstream extent of the computational domain / m
L_2	Downstream extent of the computational domain / m
M_0	Inlet Mach number
N_{exp}	Number of experimental measurements along the span
n_i	Unit normal vector
k	Specific turbulent kinetic energy / $\mathrm{m}^2\ \mathrm{s}^{-2}$
p	Order of a curve
P_i	Casing surface point
p^{opt}	Optimized design
R	Specific gas constant / J kg^{-1} K^{-1}
r	Radial distance / m
R_d	Groove radial depth / m
Re_x	Reynolds number
r_h	Hub radius / m

r_{ht}	Casing groove radius / m
R_i	Casing diffusion control points / m
r_t	Casing radius / m
S	Parametrized surface
s	Pitch / m
$U_{comp,i}$	Computed circumferential velocity along the span / m s^{-1}
$U_{exp,i}$	Measured circumferential velocity along the span / m s^{-1}
U_r	Radial component of velocity / m s^{-1}
U_{sec}	Secondary flow velocity / m s^{-1}
U_{ups}	Reference stage inlet velocity / m s^{-1}
V_{cv}	Corner vortex
w	Casing groove width / radians
w_{le}	Groove width at the blade leading edge / radians
w_{te}	Groove width at the blade trailing edge / radians
x	Axial coordinate / m
x_i	x-coordinate of the i^{th} point / m
y^+	Dimensionless wall distance
y_i	y-coordinate of the i^{th} point / m
Y_{tran}	Pitchwise transition distance / m
z_i	z-coordinate of the i^{th} point / m

Greek Symbols

α	Shape factor
α_1	Stator exit absolute yaw angle / degrees
α_2	Rotor exit absolute yaw angle / degrees
β	Scale factor
β^*	$k-\omega$ model closure coefficient
Γ	Gamma probability density function
γ	Specific heat ratio
δ	Boundary layer thickness over the casing / m
ε	Specific dissipation rate / m^2 s^{-3}
ϵ	Relative error based on CFD and Kriging

ϵ_i	Relative error based on Richardson's extrapolation
ϵ_1	Percentage error based on the initial sampling points
ϵ_2	Percentage error based on the initial and adaptive sampling points
η	Minimum distance
η_{stage}	Stage isentropic efficiency
θ	Pitchwise angular coordinate / radians
θ_g	Groove pitchwise angle / radians
$\dot{\theta}$	Design shaft angular speed / r.p.m.
θ_i	θ coordinate of the i^{th} point / radians
μ	Maximum groove depth location
ξ	Groove path curve
σ_k, σ_ω	Turbulent Prandtl numbers
ω	Specific turbulent kinetic energy dissipation rate / s^{-1}
ω_x	Axial vorticity / s^{-1}

Acronyms

APOW	Automated Process and Optimization Workbench
DOE	Design of experiment
LE	Leading Edge
NURBS	Non-Uniform Rational B-Spline
GCI	Grid convergence index
PS	Pressure Side
SS	Suction Side
TE	Trailing Edge
UNFCCC	United Nations Framework Convention on Climate Change
MAE	Average absolute error
RMSE	Root mean square error
RANS	Reynolds Averaged Navier-Stokes
RNG	Re-Normalization Group
SST	Shear Stress Transport

Chapter 1

Context and Aim

1.1 Introduction

The demand for electrical energy is projected to continue rising at substantial rates, due to the world's population growth and to increased industrial activities. As most electrical energy is currently produced in thermal power plants, advances in the design of thermal cycles and of their individual components are required to ensure that this energy supply remains sustainable and affordable. The axial turbine is a key component in a thermal power plant, as shown in Figure 1-1. The overall cycle efficiency is significantly affected by the turbine performance (Al Jubori et al., 2017) and its gain has an important role in limiting the CO_2 emissions towards meeting the UNFCCC emissions goals. In 2016, the UK used 337 TWh of electricity, 44% produced by firing 25 M tonnes of natural gas (Department for Business, 2017). The impact of improving the thermal efficiency of electricity production by natural gas alone by 1% in the UK is equivalent to an annual reduction of 600 M tonnes of CO_2 in emissions and a cost saving of £25.3 M, based on a reference gas price of 50 pence/therm.

Mixing and viscous stresses in an axial turbine generate performance loss through a variety of complex mechanisms of flow interaction. These losses are classified according to their origin, namely profile loss, tip leakage loss, and endwall or secondary flow loss. A comprehensive and detailed description of the origins of these sources is presented by Denton (1993). The main concern of this thesis is the loss contribution by secondary flows. The interaction of secondary flows with the main passage flow results in entropy generation; this accounts for considerable losses in turbomachines. Mitigating techniques for secondary flows are commonly applied in the design of axial turbomachines to manage the performance loss due to them. Low aspect ratio blades in an axial turbine lead to a high degree of secondary flow losses. The reduction of secondary flow losses is an active research area in industrial turbo-engine design, as these losses represent approximately 40% to 50% of the estimated total aerodynamic losses in an axial turbine (Schobeiri, 2005). Understanding the physics and the ability to predict these secondary flow structures is the first step to control and reduce the loss and further achieve an increase in efficiency in axial turbines.

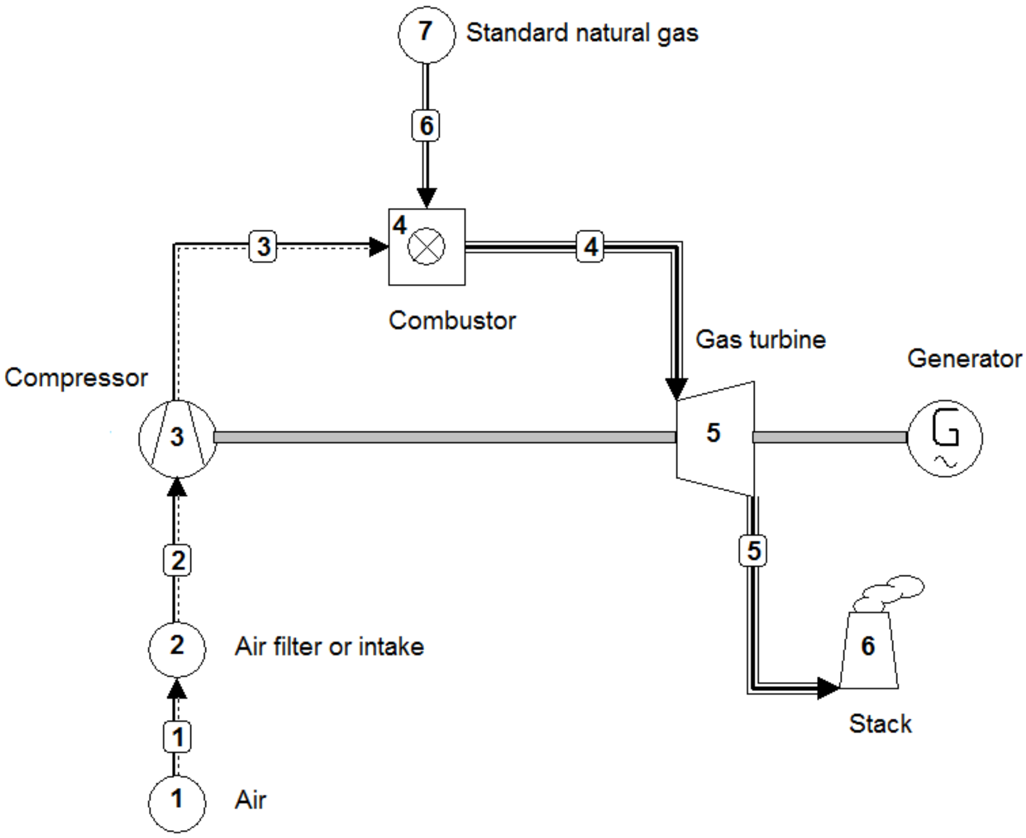

(a)

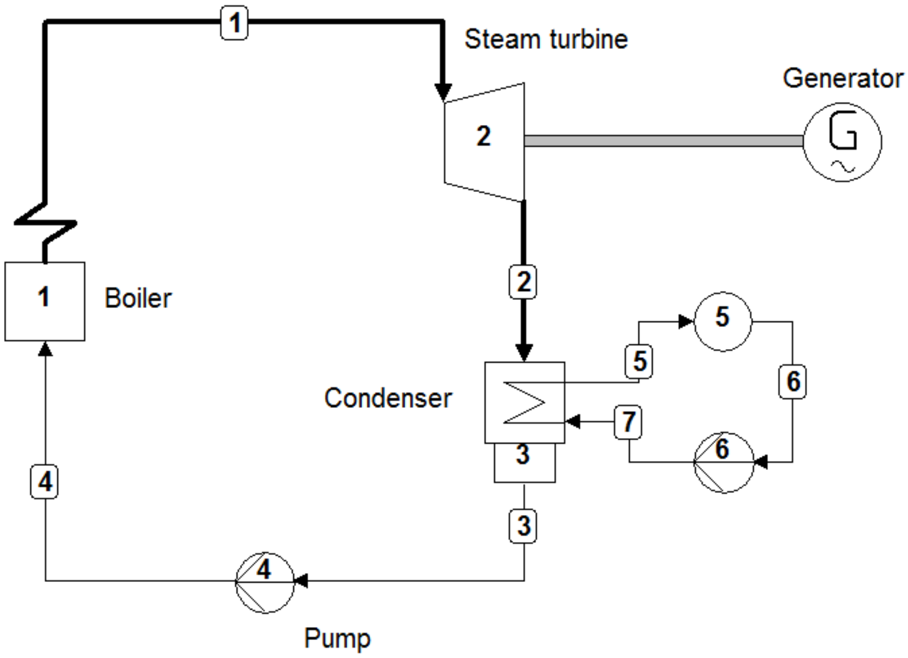

(b)

Figure 1-1: Simple (a) gas and (b) steam cycles.

A variety of toolchains is used by axial turbine designers, in which the performance and the cost of the design are significantly affected by the parametrization and optimization stages in the workflow. Advances in manufacturing techniques allow greater freedom in designing axial turbine stage passages, including non-axisymmetric endwalls. Non-axisymmetric endwall(s) contouring is one of the few effective methods that has been shown as being successful for reducing the secondary flows in a turbine stage. Therefore, furthering research on contoured endwalls, for enhancing the aerodynamic performance of power turbines, is both timely and relevant for the energy industry.

1.2 Aims and objectives

This thesis is a result of a three-year programme of research at the University of Leicester in collaboration with GE Power (ALSTOM Energy Limited). The main aims of the work programme were:

1- To minimize the secondary flow losses by the optimization of the casing endwall geometry based on three-dimensional CFD simulations. The casing design was implemented using Automated Process and Optimization Workbench (APOW) software, which provides an assessment of the sensitivity of the design parameters. It also makes the design process compatible with that of GE Power.

2- To identify a small set of free parameters in the endwall definition method that is attractive for applications to power generation at design and at off design conditions.

The experimental measurements of a one-and-half stage axial turbine "Aachen Turbine" were used for establishing a baseline CFD model of the passage flow. These measurements were provided by Walraevens and Gallus (1997). The measurements on the test case "Aachen Turbine" were carried out at the Institute of Jet Propulsion and Turbomachinery at the RWTH Aachen, Germany.

The project main aims were pursued by working through the following specific objectives:

1- To provide a validated OpenFOAM Extend 3.2 RANS model for the baseline axial turbine stator row and then for the baseline one-and-half stage axial turbine.

2- To define a new surface parameterization method of the casing endwall contouring by drawing from specialist knowledge from the Department of Mathematics, University of Leicester, where pure research on surfaces and their properties is pursued.

3- To implement the selected surface parameterization method on the casing, to provide a smooth connection at the perimeter with the remainder of the passage geometry, so that this surface definition is fully compatible with the NURBS geometrical representation used by contemporary CAD software.

4- To implement a non-axisymmetric casing design workflow flow in batch mode using the Automated Process and Optimization Workbench (APOW).

5- To compare the performance of the new casing design with an established diffusion design technique for this endwall.

6- To identify the changes in the flow structure that are responsible for the performance gains with a contoured casing.

7- To investigate the performance of the optimized turbine casing contour at off design conditions.

8- To show that a surface definition method with a small number of free parameters can give attractive increases in stage isentropic efficiency for applications to power generation at design and off-design conditions.

From a design optimization workflow perspective, this thesis shows how casing contouring can be effectively integrated in the design workflow of industrial axial turbines. It does so by embedding the new surface parametrization in the Automated Process and Optimization Workbench (APOW), which is a framework used by GE. This demonstrates the compatibility of the parametrization with a representative industry-standard design process.

From a turbomachinery aerodynamic prospective, by examining the flow pattern in some detail, the thesis provides evidence of the mechanisms responsible for the performance gain obtained from the new surface parametrization. It suggests that surface parametrizations that are closely drawn from the flow pattern are likely to deliver good performance even with a comparatively modest parameter optimization effort.

The long-term beneficial impact of this research on the industry and society is to provide an efficient and environmentally sustainable energy conversion in thermal power plants. This will be realized by an improved stage efficiency, which will offer the opportunity for reducing the emissions of carbon dioxide and of other harmful pollutants associated to the power generation process. At the same time, this research brings attractive long-term benefits to the economy by increasing the economic competitiveness of the power generation industry.

1.3 Thesis outline

This thesis is divided into seven chapters, which are listed as follows:

Chapter 1 – this section: This chapter introduces the context, the aims, the objectives, and the expected outcomes of this work.

Chapter 2: This chapter reviews the classification of losses in turbomachinery, the identified loss mechanisms, including tip leakage, and the techniques for loss reduction by endwall modifications, to date. This chapter also reviews the available analytical methods for the parametrization of the axial turbine endwalls.

Chapter 3: This chapter presents four methods of surface parameterization using a Bezier curve, a Gaussian distribution, the Beta distribution, and a cosine curve. This passage identifies the Beta distribution and the cosine curve as the two candidate methods to take onwards for the advanced implantation of chapter five.

Chapter 4: This chapter presents the computational domains of both a single stator row and a one-and-half stage axial turbine. The computational investigations were conducted using ANSYS Fluent and OpenFOAM Extend 3.2 solvers for the turbine stator cascade. The OpenFOAM Extend 3.2 solver was taken onwards for the simulation of the one-and-half stage axial turbine. This chapter also presents the CFD simulation settings, the boundary conditions, the use of the EDDYBL program by Wilcox (2006a) to generate the turbine casing inflow boundary layer, the mesh convergence index, and the converge criteria.

Chapter 5: This chapter presents the numerical optimization procedure of the casing endwall and how to perform the sensitivity analysis of the outcome from the optimization procedure through a quality indicator technique. It then describes the implementation of the optimization and of the sensitivity analysis in the Automated Process and Optimization Workbench (APOW).

Chapter 6: This chapter presents the validation of CFD models of the single row stator and of the one-and-half stage axial turbine. The models are then used to investigate the flow structures that are responsible for the performance loss with an axisymmetric casing. To counter this loss, CFD is used to test four different casings designed with a groove, an optimised groove, and by the reference diffusion design method, tested at design and at off-design conditions. The optimization sensitivity analysis for these designs is presented.

Chapter 7: This chapter draws the conclusions based on the research presented in this thesis and gives suggestions for further research.

Chapter 2

Literature Review

2.1 Introduction

This chapter gives an overview of the published work that is related to the current research. The isentropic efficiency of a contemporary axial compressor stage is around 90% and the isentropic efficiency a contemporary axial turbine stage is up to 95%, as quoted in Chernobrovkin and Lakshminarayana (1999). Further improvements in the turbine stage efficiency become more difficult and require a much deeper understanding of the flow field inside turbomachines. However, advances in manufacturing and in computer-based optimization techniques can be used to enhance the efficiency of energy conversions processes, such as by reducing the aerodynamic loss in thermal power plant turbomachines.

Over the last five decades, different techniques have been developed in order to reduce the secondary flow losses. A selected review of effective techniques related to endwall modifications is presented in this chapter. This includes a focused literature review on non-axisymmetric endwall contouring and on its effect on the secondary flows. This chapter also discusses the loss generation mechanisms and the development of secondary flows in a turbine blade passage. The effect of running the axial turbine off-design is considered. Finally, the interaction between the tip leakage flow and other secondary flows is briefly presented.

2.2 Loss mechanisms in turbomachines

A detailed description of the origins of loss mechanisms in turbomachines is presented by Denton (1993). Denton (1993) asserts that consideration of entropy production provides a good physical understanding to evaluate the loss generated in a turbomachine. The advantage of entropy is that it does not depend on whether the frame of reference is stationary or rotating, like in stators and rotors of axial turbines. However, the change in entropy cannot be measured directly but it is calculated in terms of both temperature and pressure changes of the working fluid as (Schüpbach, 2009):

$$\Delta s = c_p \ln\left(\frac{T}{T_{ref}}\right) - R \ln\left(\frac{P}{P_{ref}}\right) \tag{2.1}$$

There are three main processes that create entropy, namely viscous friction, heat transfer, and non-equilibrium processes. The flow field in a turbine is highly complex and these losses are rarely independent from each other. An understanding of the complex flow fields associated with the turbine efficiency is therefore crucial.

The sources of loss in an axial turbine stage can be divided typically as follow: profile loss, tip leakage loss, and endwall loss (Denton, 1993). The first refers to the loss generated in the blade boundary layers where the flow can be described as two-dimensional. The second category refers to losses resulting from the leakage of flow over the tip of the blades, whether shrouded or unshrouded, and the losses are caused by its interaction with the mainstream flow. The last loss type is classified as secondary flow loss because it arises from the secondary flow structure and the boundary layers within the blade passage. The relative sizes of the above three categories of loss depend on the design of the turbine.

2.2.1 Secondary flows

The secondary flows in turbine blade passages play a significant role in generating aerodynamic performance loss. These flows are responsible for approximately 40% to 50% of the estimated total aerodynamic losses in an axial turbine with a small aspect ratio (Schobeiri, 2005). Understanding the physics and the ability to predict the secondary flow structures is the first step to control and reduce the loss and to achieve an increase in turbine efficiency.

Langston (2001) presented a review of the secondary flow structures, identified either by experiments or by Computational Fluid Dynamics (CFD), without considering tip clearance, in axial turbines. Langston (2001) also reviewed the available approaches to reduce the secondary flow loss. He identified three main vortices, namely the horseshoe vortex, the passage vortex, and the corner vortex. These and other vortices are reported to be mutually interacting and difficult to separate from one another. The axial development and structure of those vortices, as reported in Wang et al. (1997), is shown in the Figure 2-1.

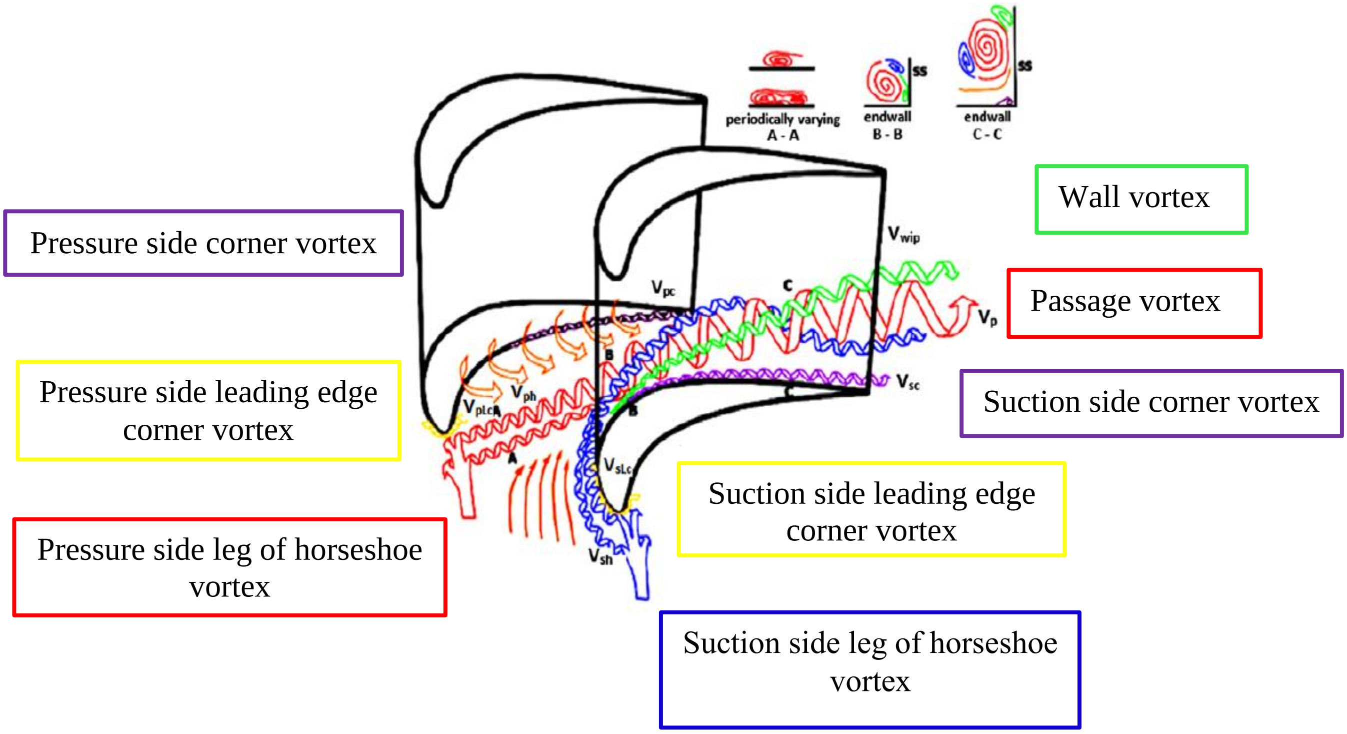

Figure 2-1: Secondary flows through a turbine blade passage, from Wang et al. (1997).

Sieverding and Bosche (1983) and Acharya and Mahmood (2006) provided a detailed explanation of the peculiar flow features near the endwall that are caused by the presence of an upstream inflow boundary layer. These features are identified by the dashed lines shown in the surface flow visualization of Figure 2-2. The upstream boundary layer bifurcates at the leading edge of the blade forming a saddle point. Acharya and Mahmood (2006) defined the saddle point as “the location on the endwall where the zero degree incidence line meets the separation line and corresponds to the lowest friction velocity”.

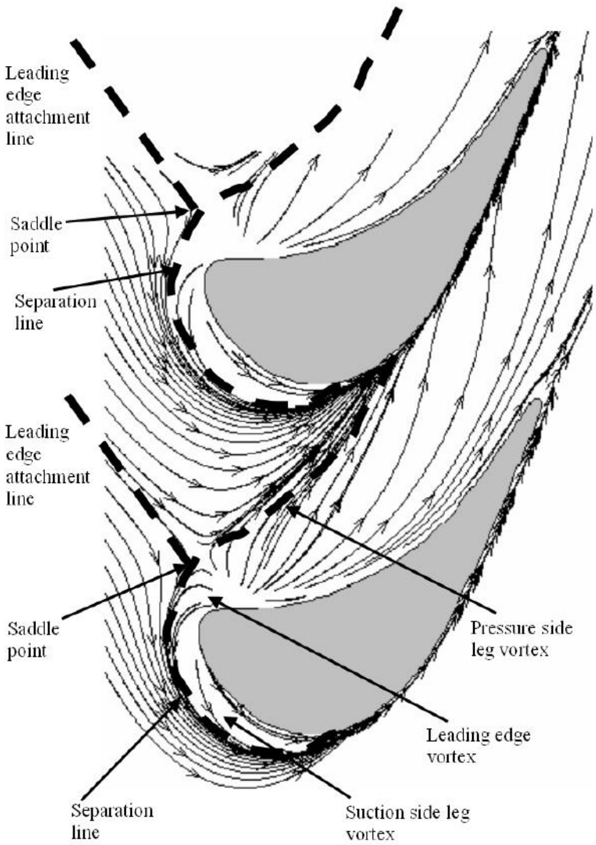

Figure 2-2: Saddle point and separation lines in a near endwall plane of a linear cascade passage, from Acharya Mahmood (2006).

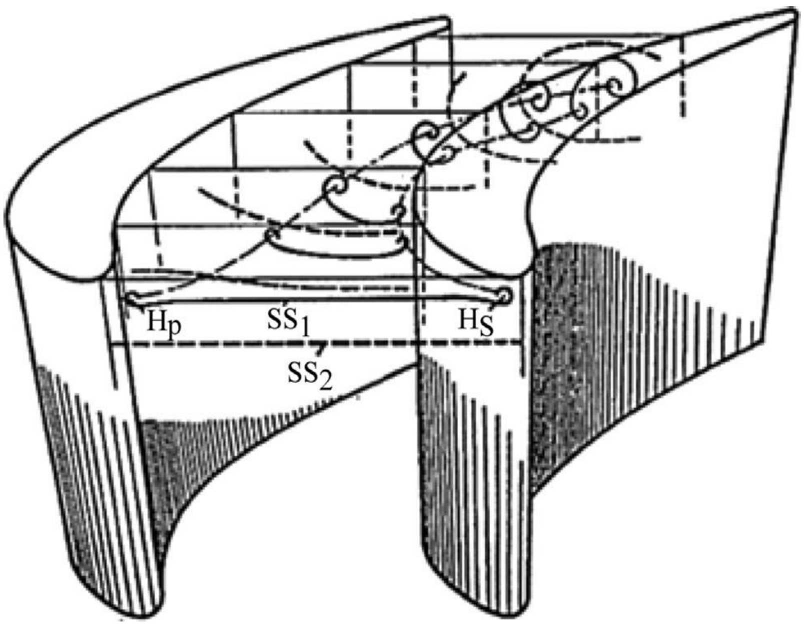

Figure 2-3: Streamwise evolution of horseshoe and passage vortices, from Sieverding and Bosche (1983).

Due to the interaction of the endwall boundary layer with the adverse pressure gradient from the blade potential pressure field, a horseshoe vortex is generated near the junction of the blade leading edge and the endwall. Gostelow et al. (2012) showed the horseshoe vortex by surface flow visualisation and a sample of this visualisation is shown in Figure 2-4. The horseshoe vortex left and right are arms bend downstream into the passage on both pressure and suction sides, forming two legs of the early passage flow. The pressure side vortex is swept by the cross-flow that is generated by the passage pressure gradients. At about half way between the passage entry and exit planes, the suction side leg vortex merges with the pressure side leg vortex and both form the passage vortex. This vortex grows in size and strength as it moves along the suction side. Corner vortices are also induced due to the low momentum fluid at the mid-passage region, between the endwall and the blade, which remains low until the stage exit, as shown in Figure 2-1. Sieverding (1985) used a coloured smoke wire technique to visualize the entire stream surface through a turbine cascade and showed how the horseshoe (H) vortex branches (Hp and Hs) rotate about the passage axis, as sketched in Figure 2-3.

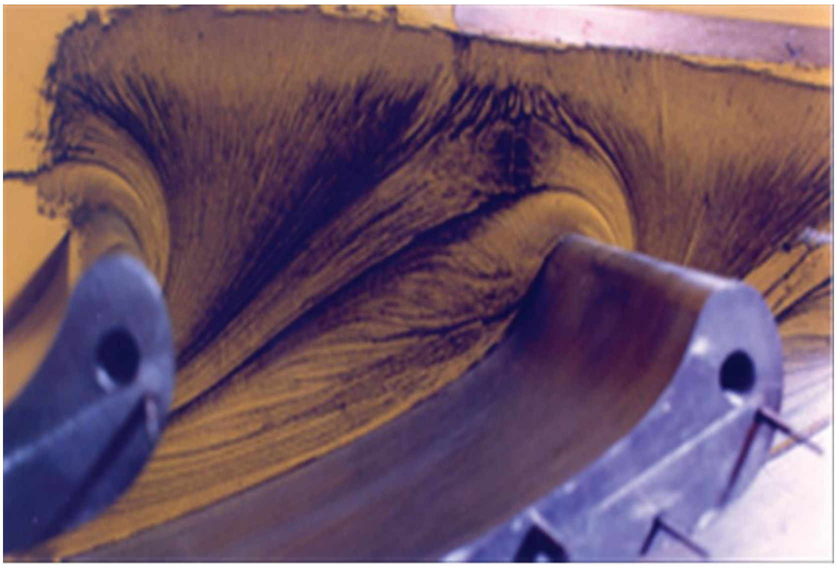

Figure 2-4: Endwall visualisation of the horseshoe vortex in a linear cascade of stator blades, from Gostelow et al. (2012).

As both branches of the horseshoe vortex merge to form the passage vortex, this process provides an important loss generation mechanism, contributing about 15% of the aerodynamic loss in a stage. Thus, it is pertinent to observe the cause of each of the vortices forming the passage vortex. The goal is to modify the development of those vortices in order to reduce the overall passage vortex loss.

Recently, to provide a comprehensive understanding of the turbine endwall loss problem, Coull (2017) performed a parametric design study to examine the impact of key design variables on the endwall loss in turbine linear cascades, which represent a simplified model of real-engine flow. Reynolds-averaged Navier–Stokes calculations were performed for a single aspect ratio and at constant inlet boundary layer thickness. Figure 2-5 shows a diagram based on one of the performed RANS simulations, where vortex structures were visualized. The author demonstrated that endwall loss is a sum of two components: the dissipation associated with the endwall boundary layer and the secondary flows. The streamwise vorticity predicted by classical secondary flow theory is shown to be a good indicator of the secondary-flow-induced loss. A future work was suggested to examine the effects of inlet conditions, aspect ratio, and to relate the turbine cascade endwall loss to the flow through a real turbine blade row.

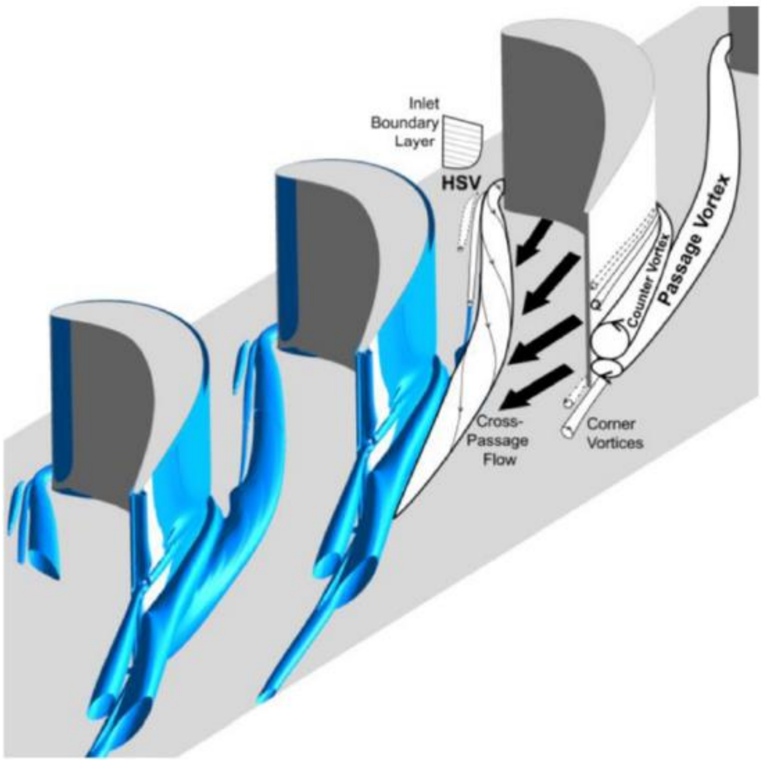

Figure 2-5: The vortex flow pattern through a linear turbine cascade, from Coull (2017).

2.3 Effect of off design conditions

The experimental results from a linear turbine cascade for two positive incidences were reported by Benner et al. (1997) who found that the saddle point shown in Figure 2-2 moves toward the mid-pitch with increased incidence. The blade pressure distribution changed from mid-loaded to front loaded. This results in a significant effect on secondary flows at 20° incidence, at which the total pressure loss is doubled. A more modest effect on secondary flows was observed at 10° incidence.

Another experimental study of the rotor flow in a single stage of the Aachen Turbine (Walraevens and Gallus, 1997) was performed by Gallus and Zeschky (1992). The structure of the rotor secondary flows was investigated at increased and decreased rotor blade loading. The mass flow and shaft speed of the turbine were varied to change the rotor blade loading. The results showed that increasing the blade loading results in lowering the turbine isentropic efficiency due to rising secondary flow losses.

Snedden et al. (2010) examined the application of a non-axisymmetric endwall to a turbine rotor across a range of loads using both experiment and CFD. The spanwise extent of the rotor hub secondary flows increased as the load increased. The results showed that stage efficiencies were improved for all conditions.

2.4 Effect of tip leakage flows

Most rotating turbine blades are either shrouded or unshrouded. In an unshrouded turbine blade, the flow leaks through the gap between the blade tip and the casing, due to the pressure difference between the blade pressure side and the blade suction side. The leakage flow induces a thin boundary layer, local flow separation, and reattachment over the casing. Furthermore, it forms a tip leakage vortex by its interaction with the mainstream flow and with the passage vortex. Those complex flow phenomena induced by the tip leakage flow and by the leakage vortex cause significant aerodynamic losses and high heat load to the near-tip region of the blade.

Tallman and Lakshminarayana (2001a, 2001b) performed three-dimensional numerical simulations of a linear turbine cascade to study the effects of turbine inflow and shape parameters on the tip leakage flow and vortex development. To understand the detailed flow physics, the effects of tip clearance spacing, inlet conditions, and relative endwall motion were simulated and modified sequentially. The authors highlighted additional secondary flows that exist near the casing region of the axial turbine. These are generated by the effect of the passage vortex and the wall jet type flow as the blade passes over the casing. The results showed that the reduction in tip clearance height and in the relative motion in the endwall result in less mass flow passing the gap and a smaller leakage vortex. Conversely, increasing either parameter increases the losses associated with the near casing secondary flow.

The main tip leakage loss is generated by a mixing process between the leakage flow and the mainstream flow. Ingram et al. (2005) studied a non-axisymmetric endwall in a high aspect ratio turbine cascade assuming the effect of the tip clearance is negligible compared to other sources of loss. However, a later study by Snedden et al. (2010) reported that an apparently strong interaction occurs between non-axisymmetric endwalls and the tip clearance flow in a rotating rig. Based on this evidence, in this thesis, it was decided to model the rotor tip clearance in the CFD simulation corresponding to the experimental measurements of the Aachen turbine test case.

2.5 Endwall modifications

2.5.1 Endwall fences

Chung et al. (1991) stated that a boundary layer fence in the turbine passage can reduce the aerodynamic losses and improve the performance of film cooling on the suction surface near the endwall region. The fence changes the endwall flow as sketched in Figure 2-6.

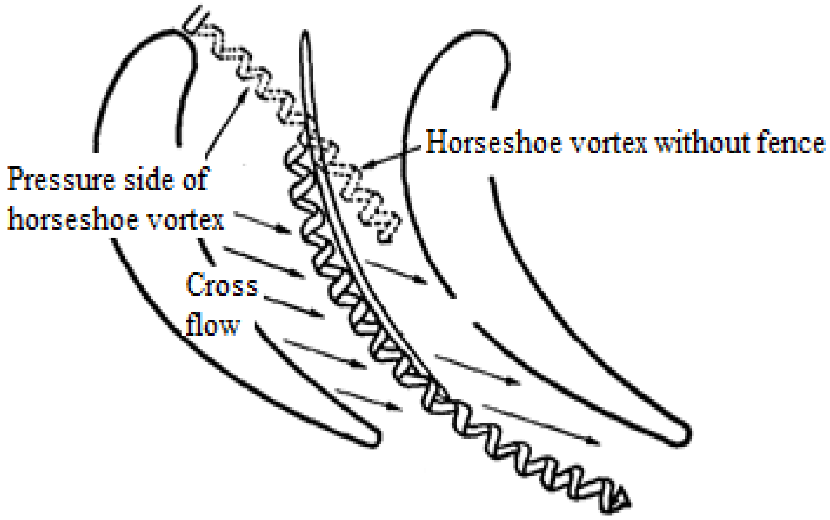

Figure 2-6: Secondary flows in the endwall region with and without a fence, from Chung et al. (1991).

To reduce secondary flow losses in a linear turbine cascade, Kumar and Govardhan (2011) applied a streamwise endwall fence. They optimised the fence geometry by performing numerical experiments. They identified an optimum fence geometry located in the middle of the flow passage with the fence height varying linearly from the leading edge to the trailing edge. By introducing this fence, the exit flow angle deviation, secondary flow losses, and the magnitude and spanwise penetration of the passage vortex were reduced.

Kawai et al. (1989) showed that using endwall fences can result in a considerable attenuation of secondary flows, an improvement of the flow quality entering downstream stages, and a 26% reduction in the total pressure loss.

Fences have shown good promise in laboratory experiments. Their application to engines is not yet matured, possibly due to concerns about their integrity from a long-term exposure to the high-temperature flows.

2.5.2 Air injection or suction

Bloxham and Bons (2010) tested blowing and suction in a low pressure turbine cascade that resulted in a reduced loss of up to 28%. 23% of this performance gain was required to power the flow control system. The flow was controlled either by the removal of the boundary layer, by suction, or by near-wall flow redirection, as shown in Figure 2-7.

The removal approch gives a direct control on the passage vortex, while the redirection appoach is used to alter the trajectory of the passage vortex.

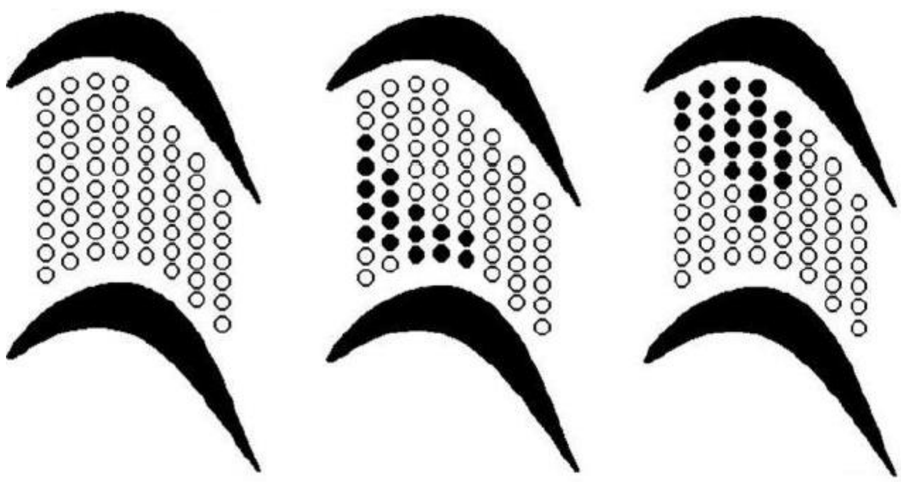

Figure 2-7: Control of secondary flows with two different endwall suction approaches, from Bloxham and Bons (2010).

A computational investigation into injecting air through a cylindrical hole in the endwall of the nozzle guide vane was performed by Dhilipkumar (2016). The effects of this air injection on the formation of the leading edge horseshoe vortex and on the consequent passage vortex were modelled. The results indicate that an appropriate selection of the air injection parameters weakens the leading edge horseshoe vortex and delays the migration of the passage vortex across the guide vanes.

Funazaki et al. (1996) investigated experimentally the air suction approach to reduce the secondary flow effects for applications to gas or steam turbine nozzles. This included sucking the working fluid to reduce the upstream boundary layer thickness, which resulted in an attractive reduction of the cascade loss by controlling the passage vortex developed within the blade passage.

Suction and blowing enables the intermittent operation of the endwall treatment, as well as the implementation of feedback control techniques. The main challenges for this technique are the handling of hot gasses through the aspiration slots and the additional cost of providing mass injection, for instance by using flow bled from an upstream blade row.

2.5.3 Axisymmetric contouring

The practice of using RANS simulations with experimental measurements to evaluate endwall modifications is relatively recent. In Dossena et al. (1999), detailed experimental measurements and three-dimensional (3-D) numerical simulations were performed to investigate the effect of a radially profiled axisymmetric casing contour on the turbine nozzle guide vane performance. The comparison between the radially profiled and cylindrical endwalls showed a significant improvement in the performance of the cascade with the radially profiled casing. This cascade not only achieved lower secondary losses but also exhibited a reduction in the profile losses.

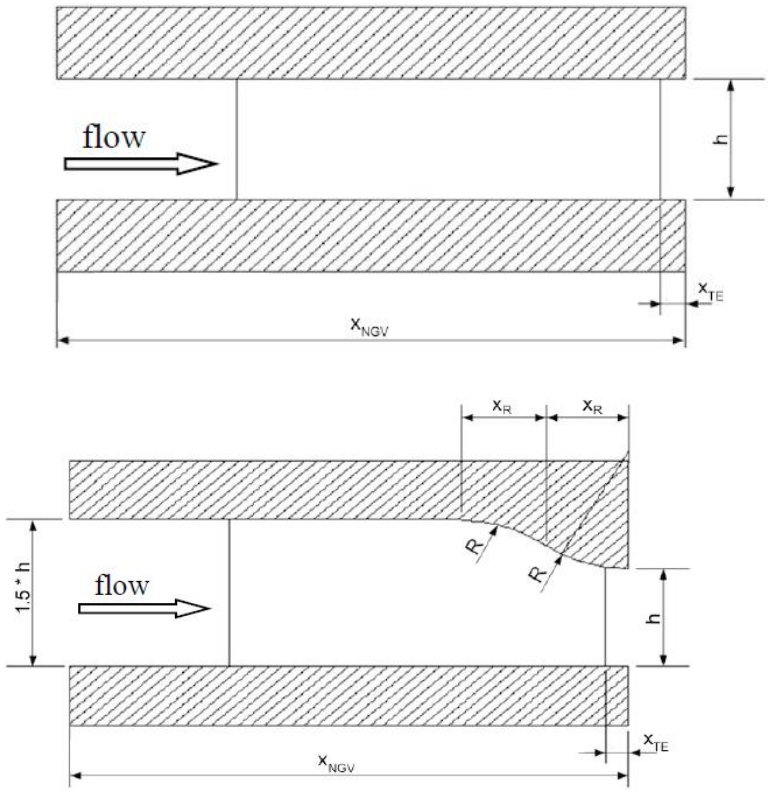

Figure 2-8: Illustration of the refrence shroud geometry and the radially-profiled endwall geometry, from Moser et al. (2013).

Moser et al. (2013) applied an optimization technique to design a new radially profiled axisymmetric shroud for a guide vane of a steam turbine stage as shown in Figure

2-8. An evolutionary algorithm was used to drive the changes in the radial dimension of the casing. The numerical results indicated that the axisymmetric profiling produced a significant beneficial effect on the stage loss over a wide range of pressure ratios, with some adverse effects at extreme partial loads.

Barigozzi et al. (2010) reduced the overall loss associated with the contoured passage of a linear cascade of turbine stator blades by 20% compared to the overall loss of the passage with flat endwalls. Most of this reduction was attributed to a reduction in the profile loss as there was a reduction in the secondary flow losses on the flat wall side while an increase of about the same amount on the contoured side.

Axisymmetric radially-profiled endwalls may have originally been designed for the use in highly loaded turbines with a substantial flow velocity increase through the passage. Modern turbines for power tend to use less aggressive flow expansions and peak Mach numbers, for efficiency, which may limit the pressure recovery that is achievable from using axial variations in the radius of the endwalls.

2.5.4 Non-axisymmetric endwall contouring

A survey of some developments related to three-dimensional endwall contouring is now presented to set the baseline for formulating new surface definition methods. Different surface definition methods are used in the literature to parametrise non-axisymmetric endwalls. By using non-axisymmetric walls, it has been shown that losses can be reduced, which in turn leads to an increase in the isentropic thermal efficiency of axial flow turbines. The reason behind this is the reduced heat generated over the blade pressure surface. This heat is generated due to friction in shear layers and in the boundary layers.

Endwall profiling aims to reduce the aerodynamic losses or heat transfer rates by shaping the endwalls of the turbine hub and casing. The shaping either accelerates the flow, which decreases the local static pressure, or decelerates the flow, which increases the static pressure, as shown schematically in Figure 2-9. This way, the endwall cross-passage flow can be reduced by altering the pitchwise pressure gradient to reduce the associated secondary flows (Ingram, 2003).

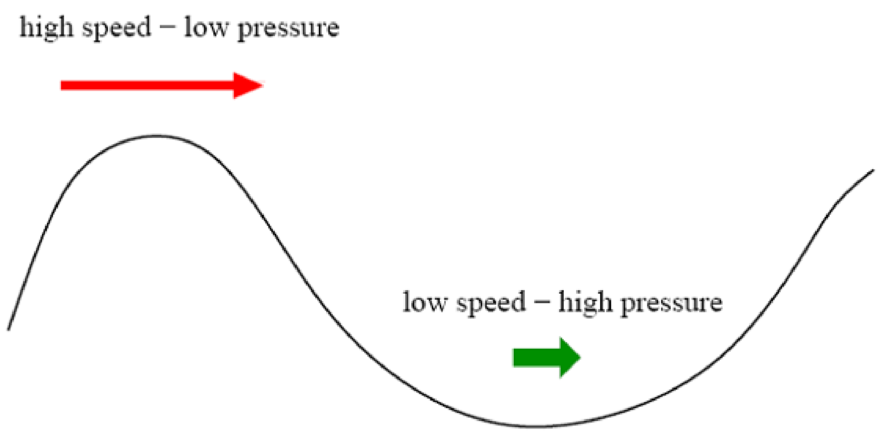

Figure 2-9: Streamline curvature effect on the local static pressure, from (Ingram, 2003).

Hartland et al. (1999), Ingram et al. (2002) and Ingram (2003) described the design and testing of a profiled endwall in the Durham University linear cascade that achieved reductions in secondary flow loss of 24% (Ingham et al., 2002) and of about a 30% (Ingham, 2003). Similarly, Brennan et al. (2003), Harvey et al. (2002) showed that using the non-axisymmetric contouring of Figure 2-10 results in a one-third reduction in the endwall loss or a 0.59% increase in the stage efficiency for the high pressure turbine and a 0.9% efficiency increase in the intermediate pressure turbine of the Rolls-Royce Trent 500 engine.

A numerical simulation of a nozzle guide vane passage with a profiled hub was first performed by Rose (1994). About 20 years later, Dunn et al. (2015) modelled the unsteady flow and the performance of a 1.5 stage turbine test rig with a profiled rotor hub endwall. Their results indicate that, at the selected test conditions, this flow does not warrant the added computational expense of an unsteady simulation, unless the nature of the flow is substantially more unsteady or transient boundary conditions are used.

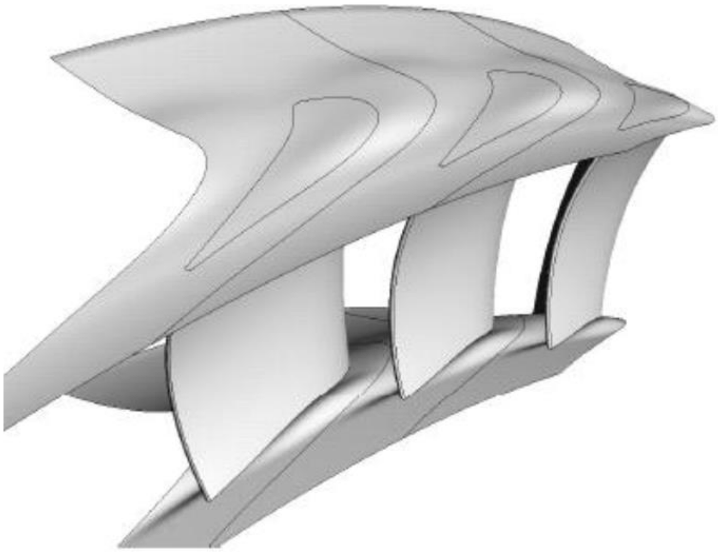

Figure 2-10: High pressure NGV with non-axisymmetric endwall contouring, from Brennan et al. (2003).

Germain et al. (2010) improved the efficiency of a one-and-half stage high work axial flow turbine using non-axisymmetric endwall contouring. The improvement was not only achieved by the reduction in the secondary losses but also by the weakening of the mid-span flow losses. The comparison between CFD predictions and measurements indicated that further modelling work is needed to improve the overall loss predictability. Schuepbach et al. (2010) furthered the work by Germain et al. (Germain et al., 2010) by analysing the time-resolved flow physics experimentally and numerically. Schuepbach et al. (2010) confirmed the predicted efficiency improvements and showed that the profiled endwall also reduced the blade trailing edge shed vorticity.

A detailed numerical and experimental investigation was performed by Poehler et al. (2010) to determine the effects of non-axisymmetric stator endwall contouring on the isentropic efficiency of a turbine stage. The results showed an aerodynamic improvement in terms of efficiency and a reduction in the secondary kinetic energy.

Miyoshi et al. (2013) developed a non-axisymmetric endwall contouring technology of an air turbine nozzle. A reduction of secondary flow losses was achieved at both the casing and at the hub. The area mass-averaged total pressure loss coefficient decreased by 27% in the numerical simulation and by 35% in experiment compared to the original blade performance.

How the endwall geometry is parametrized has a crucial importance in the design optimization process. Harvey et al. (2000) and Turgut and Camci (2015) adopted beta-spline and Fourier series based curves in the streamwise and pitchwise directions to define the profiled endwall shapes. They demonstrated a clear reduction in secondary flows and further achieved an increase in the turbine efficiency. They demonstrated that non-axisymmetric endwall contouring is a powerful tool to reduce secondary flows, particularly to reduce the secondary kinetic energy and the exit angle deviations.

Germain et al. (2010) used a combination of a pitch-wise shape function and a stream-wise decay function that, when multiplied and scaled, define the contoured endwall surfaces. Although Germain et al. (2010) had shown by experiment a significant efficiency benefit from using this endwall contouring technique, of 1% $\pm$ 0.4%, Praisner et al. (2013) argued that there were disadvantages in using shape functions to parametrise a contoured endwall. Simple shape functions, such as a sinusoidal curve, imply a preconceived notion of the resulting geometry and the design will be limited to these shapes, while the optimal contour geometry could be quite different. More complex geometries can be defined by using more complicated shape functions, such as those involving Fourier series, although, typically, the relationship between the performance and the geometry parameters becomes more difficult to understand. Accordingly, the challenge is to find an optimal endwall parametrization that achieves the objectives of reducing losses and increasing the efficiency.

Praisner et al. (2013) therefore proceeded to parametrize their geometry using two-dimensional cubic splines in the pitchwise and streamwise directions. The splines were controlled by a matrix of control points distributed along the endwall at the crossings of upstream, downstream, half-pitch, and mid-pitch lines between adjacent blades. This removed some of the restrictions from the prescribed shape of the guide curves used in the previous work.

Many researchers have used computer-based optimization methods to enhance the system performance of axial and radial turbines (Da Lio et al., 2016, Meroni et al., 2017, Song et al., 2017, Al Jubori et al., 2016). This includes the application of computer-based optimization to contoured endwalls of axial turbines. For instance, Sun et al. (2014) improved the aerodynamic performance of a highly loaded turbine stator using non-axisymmetric hub and shroud endwalls. This study used an optimization technique based on combining endwall profiling parametrization, global optimization, and aerodynamic performance evaluation methods. Both the experimental and numerical results demonstrated that the secondary flow losses and the profile loss with the optimized endwall were significantly reduced compared to the reference axisymmetric case.

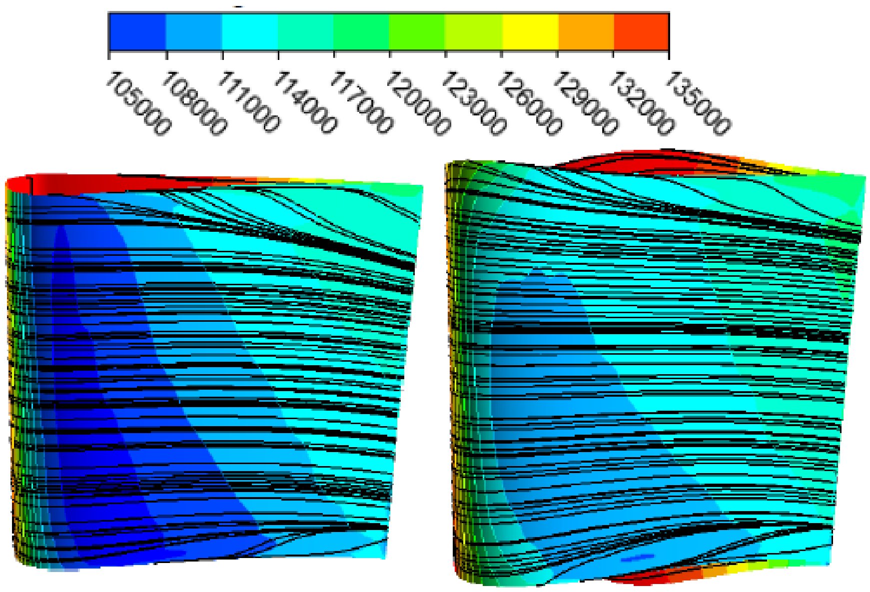

(a) (b)

Figure 2-11: Colour iso-levels of static pressure (Pa) with limiting streamlines over a blade with (a) axisymmetric and (b) optimized contoured endwalls, from Tang et al. (2014).

An optimization procedure was implemented by Tang et al. (2014) to design the profiled endwalls in a one-and-half stage high-work axial turbine. The effects of the optimum profiled endwalls on the turbine were analysed by steady simulations and the results confirmed by unsteady simulations. A sample of their prediction is shown in Figure 2-11. This figure gives some insight into how shroud contouring affects the relevant flow features, such as the weakening of the passage vortex close to the turbine shroud. They found that a 10.7% total pressure loss decrement across the first stator and a 4.1% total pressure loss reduction across the rotor gave an overall 0.4% stage efficiency increase. Furthermore, both the secondary loss and the profile loss were significantly reduced.

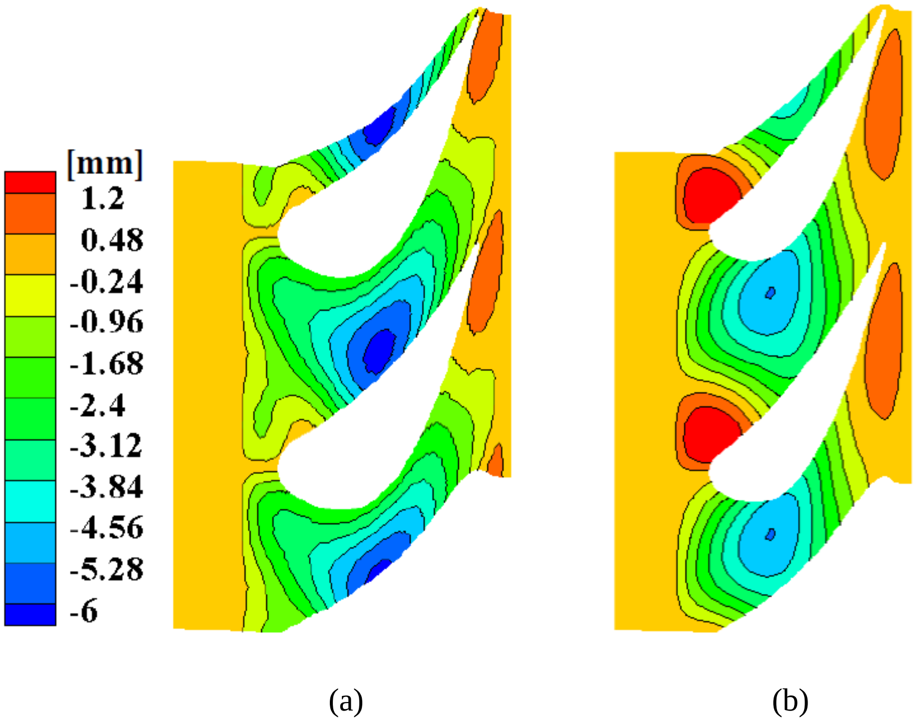

Figure 2-12: Radial height changes of the optimum profiled endwalls for the first stator: (a) hub and (b) shroud, from Tang et al. (2014).

Figure 2-12 shows the height deviation of the optimum profiled endwall surfaces. It can be clearly seen that the changes in the surface radial position in the hub is quite different compared to the shroud. A later study by Tang et al. (2015) investigated the effects of these profiled endwalls on the turbine unsteady flow field using unsteady simulations. The numerical results showed that the profiled endwalls on the first stator not only reduce the losses from the secondary flows and trailing edge shed vorticity of the stator, but also improve the performance of the rotor. However, the profiled endwall of the rotor had almost no effect on the performance of the first stator, but was predicted to introduce significant unsteady effects to the turbine as the fluctuations of the flow fields were predicted to become stronger over time.

Na and Liu (2015) optimised the non-axisymmetric contoured endwalls for the hub and shroud of a high pressure turbine stator. The numerical results showed that the optimized non-axisymmetric endwalls have merit in reduceing the flow losses in the stator as indicated in Figure 2-13 (a). However, Figure 2-13 (b). showed that they can also affect the flow parameters at the stator exit, such as the flow angle, so that the flow losses at the rotor exit were predicted to increase from changes in the incidence angle of the rotor. As a result, the turbine stage performance was not improved.

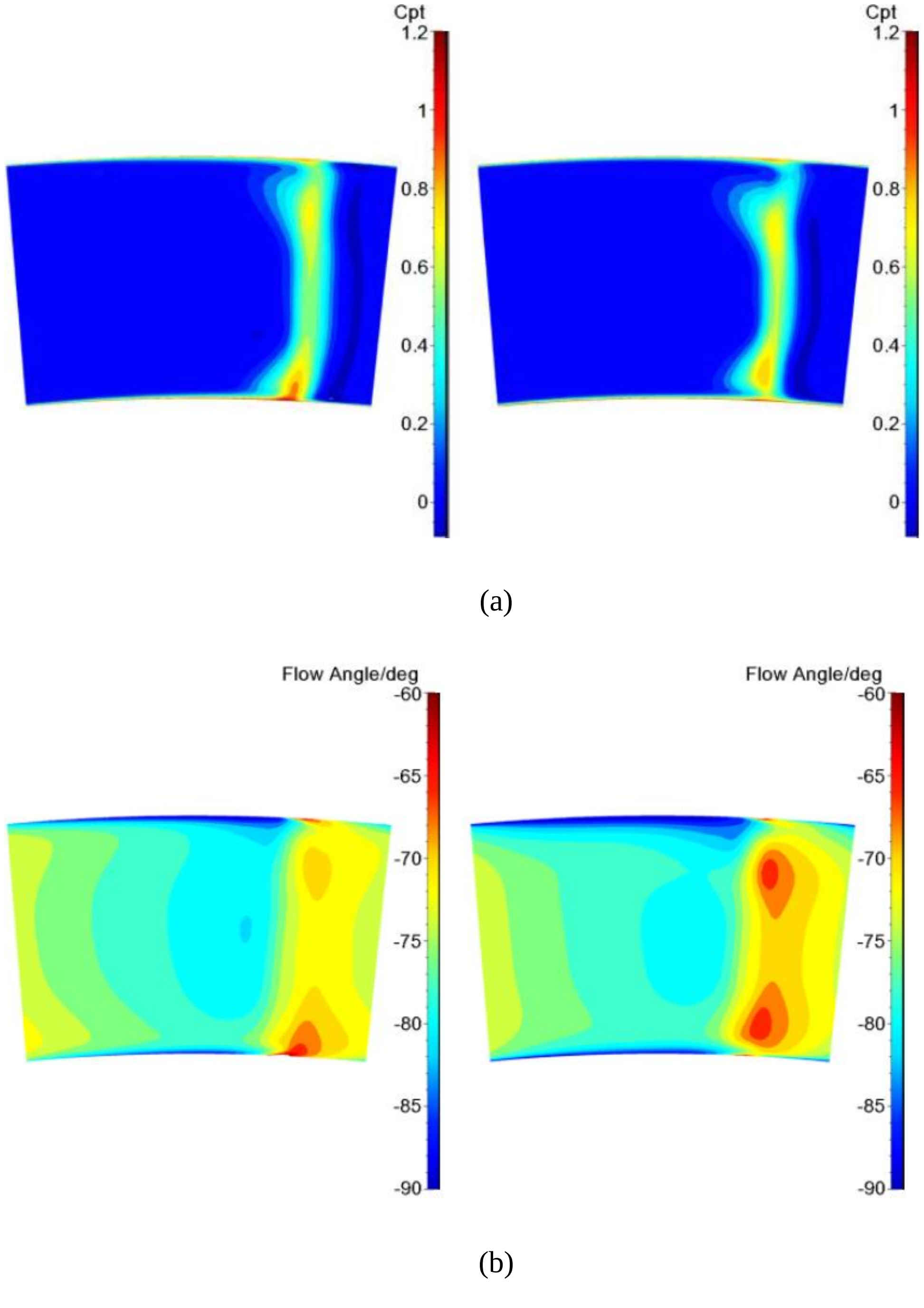

Figure 2-13: Colour iso-levels of the baseline and contoured endwalls at the stator exit. (a) total pressure loss coefficient (b) flow angle, from Na and Liu (2015).

Kim et al. (2016) optimized individually a non-axisymmetric shroud and hub of a 1-stage high pressure transonic turbine. The response surface was created using a Kriging technique. The optimum solution was found using a Genetic Algorithm with the stage efficiency as the objective function. The results indicated that the optimal casing profile reduced the loss significantly more than the optimal hub. The efficiency was improved by 0.4% based on the optimal shroud geometry while by 0.39% based on both the optimized hub and shroud. The lower rotor loss reduction resulted from the application of both the hub and shroud designs. Adding just the hub design led to a negative effect on the performance.

An optimazation procedure for profiling the endwall of an axial compressor cascade was performed by Reutter et al. (2014) to reduce the total pressure loss and to improve the flow angle. This procedure used the DLR in-house tool AutoOpti and the RANS-solver TRACE. The authors used the NACA-65 K48 cascade profile with and without a fillet with six splines defined by control points at the endwall, as shown in Figure 2-14. Different operating points were considered to examine the effect of the optimized design over a representative operating range of the axial compressor cascade.

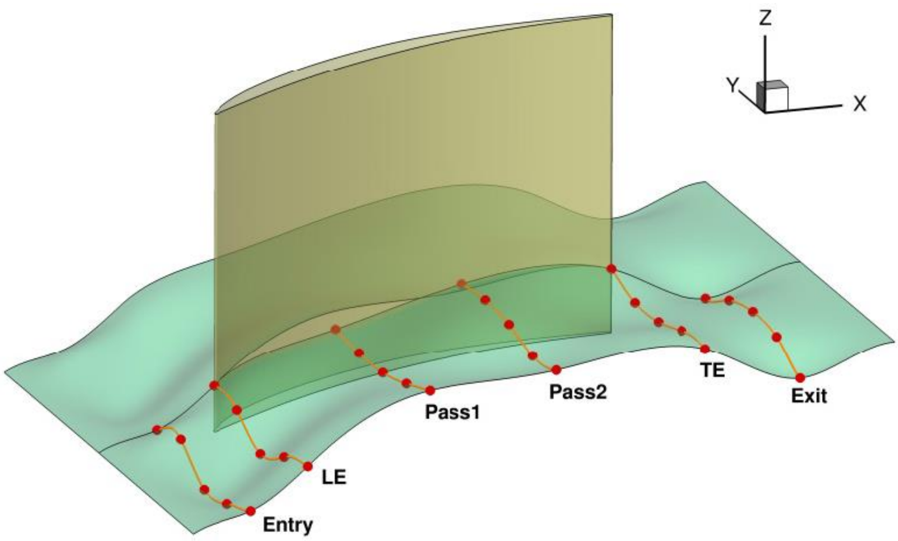

Figure 2-14: Six splines consisting of the control points used to define the hub endwall, from Reutter et al. (2014).

Poehler et al. (2015) studied numerically the effect of non-axisymmetric endwalls and of three-dimensional aerofoils on the secondary flows of a one-and-half axial turbine stage. A contoured endwall for the hub and shroud, a bowed profile stacking and a combination of both were applied to the first stator. In addition, a contoured endwall was developed for the hub of the unshrouded rotor. The stage efficiency was used as the target function to optimize all designs. The results from this global optimization showed an increase in the stator total pressure loss and in the secondary flow. However, these designs led to a more uniform exit flow angle distribution and thus to a subsequent reduction of the rotor losses that overcompensated the higher stator losses. Part two of this paper (2015) reported on the experimental validation of the numerical results. A good agreement was observed with the numerical results as the mechanical efficiency increased as predicted. The experimental results also demonstrated that the new designs still work satisfactorily at off-design conditions.

More recent investigations adopted a more holistic design approach to endwall contouring, including considerations of heat transfer, seal flow, and off-design operations. Lynch et al. (2011) and Puetz et al. (2015) investigated the effect of using contoured endwalls on the heat transfer characteristics, Cao et al. (2014) and Gier et al. (2002) studied their use in conjunction with three-dimensional turbine blades, and Hu and Luo (2014) considered their effect on the rim seal flow. Reising and Schiffer (2009) optimized the stator endwalls in a transonic compressor at several operating point. They found that, even though the shroud was optimised at off design conditions, it resulted in a 0.03 % additional efficiency improvement at the design point.

Non-axisymmetric endwall contouring was found to be comparatively the more mature technology for axial turbines. It has shown good performance at design conditions and off-design.

2.6 Summary and prospective

The literature survey has indicated that the application of non-axisymmetric contouring to the endwall surface of axial turbomachines has been shown in general to reduce the interaction among the secondary flows in the stator passage and therefore to reduce the total pressure loss. One of the main benefits from using contoured endwalls is the reduction in the endwall cross-passage flow that is obtained by reducing the pitchwise pressure gradient. This is found to reduce the associated secondary flows. However, the existing literature pays limited attention to the design of non-axisymmetric endwalls at the stator casing and on its interaction with the rotor tip leakage flow.

For the optimization problems, the reduction in the numberof parameters that define the endwall surface is still a challenge. With this reduction, the optimization process will become be more treatable. Most optimizations in the literature treat both hub and casing. For the purpose of making this PhD research tractable from a time management perspective, attention will be given to the casing treatment only, which is more applicable to high aspect ratio low pressure turbine stages. It is acknowledged that, in industrial applications, the simultaneous contouring of hub and tip is likely to be implemented.

Different methods have been used for the parametrization of the contoured endwall. There is not yet consensus on the best design practice for non-axisymmetric endwalls. Techniques implemented in industry use a significant number of design parameters requiring substantial computer-based optimization. In the next chapter, a full analysis of four approaches is presented in order to obtain a smooth surface casing geometry. This resulted in the selection of a preferred parameterization approach in consulation with GE power.

Chapter 3

Non-axisymmetric Casing Wall Parametrization

3.1 Introduction

A variety of toolchains is used by axial turbine designers, in which the performance and the cost of the design are significantly affected by the parametrization of the flow passage. In investigations on profiled endwalls, the parameterization of the geometry is of crucial importance, irrespective of whether a simple linear cascade or a more complex full stage is considered. Turbine stator endwalls can be parameterised by different methods. In general, the endwall structure can be considered as a composite geometrical surface, depending on the radial coordinate, the axial coordinate, and the pitch fraction between two blades in a passage.

This chapter presents details about a mathematical procedure to define the axisymmetric casing passage geometry parametrically. This chapter also aims to describe different parametric techniques that can be used to generate a non-axisymmetric casing design surface. The Gauss distribution function and the Beta distribution function are used to define a non-axisymmetric casing of new design. In order to compare the new design of this thesis with another non-axisymmetric parametric surface design, Bezier curve and cosine curve techniques are used to define a casing surface shaped according to a more established controlled diffusion design approach. These parametric surface definition methods are compered in terms of their surface smoothness and of the way they integrate with the turbine design toolchain of the industrial collaborator GE and two preferred parametric surface definition techniques are selected. Matlab codes are generated to evaluate the axisymmetric parametric equations and to implement these techniques.

3.2 Baseline casing parametric surface definition

In this work, the RWTH Aachen Turbine test case is adopted as be baseline geometry for evaluating the effectiveness of different casing treatments. The baseline geometry and test conditions of the Aachen Turbine are given in Chapter 4. This test case uses untwisted blades, the profiles of which are available from RWTH Aachen as a dataset. The RWTH Aachen dataset of points P_i in (x, r, θ) is re-stated in 3 D Cartesian coordinates as

$$P_i = (x_i, r_t \, cos \, \theta_i, r_t \sin \theta_i) \tag{3.1}$$

for compatibility with ANSYS ICEM CFD, as stated in Chapter 4. Three surfaces are modelled mathematically to represent the upstream stator casing delimiting one flow passage. These are referred to as the blade to blade passage surface, the extended inlet surface, and the extended outlet surface. 65 points define the blade pressure side and 47 points the blade suction side. In order to facilitate the definition of an axisymmetric casing surface, the blade profile in Cartesian coordinates (x, y, z) is remapped to the cylindrical coordinates (r, θ, z). The blade profile points are then projected on the casing cascade plane in MATLAB by the function

$$P_i = \left[x_i, \frac{\pi}{2} - \arctan\left(\frac{y_i}{z_i}\right)\right] \tag{3.2}$$

The passage inlet casing surface is defined in MATLAB based on the following parametric surface function:

$$f\,(u, v\,) = \begin{pmatrix} (1-u)d_1 \\ r_c \cos\left(\theta_1(1-v) + \theta_2 v\right) \\ r_c \sin\ \left(\theta_1(1-v) + \theta_2 v\right) \end{pmatrix} \tag{3.3}$$

where r_c = 0.3 m, d_1= -0.143 m, θ_1=1.4264595 rad, and θ_2= =1.600992 rad. When restricting the parameters to $u \in [0, 1]$ and $v \in [0, 1]$, the passage inlet area is generated as shown in the Figure 3-1.

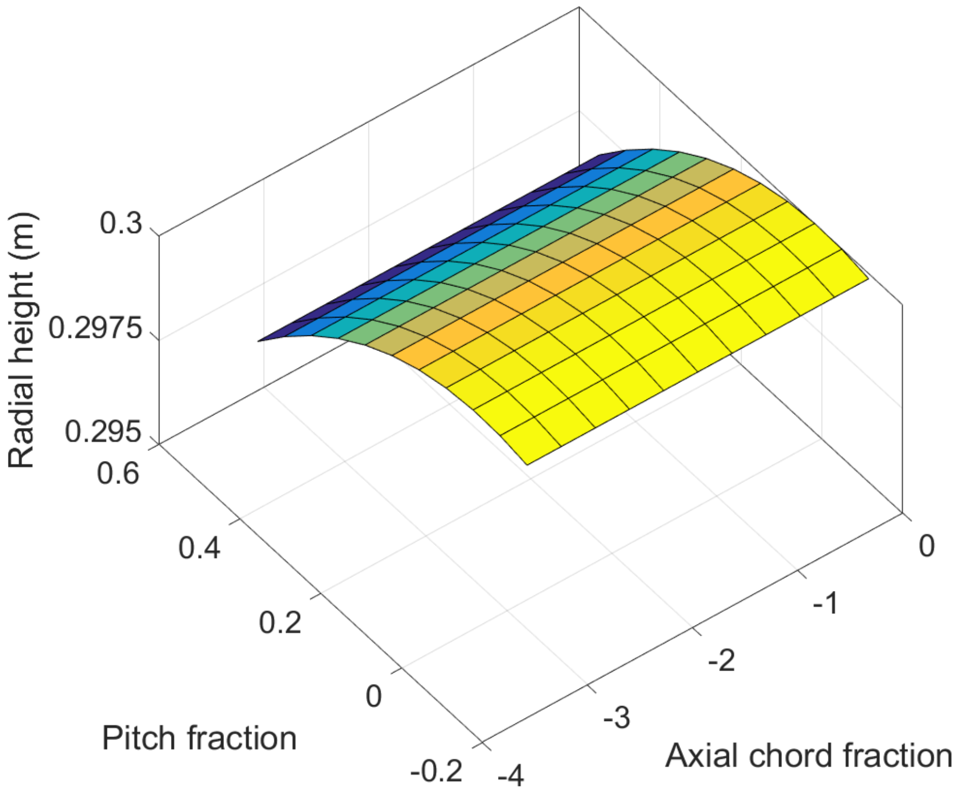

Figure 3-1: Casing passage inlet surface.

The projected points of the turbine stator profile are interpolated using smoothing cubic splines. Separate cubic splines are used to define the pressure side edge and the suction side edge. The cubic spline coefficients are obtained by the MATLAB functions csaps and ppval. The function determining the cylindrical blade to blade passage, as shown in Figure 3-2, is

$$f(u, v) = \begin{pmatrix} u d_3 \\ r_c \cos\left(\alpha_1(u)(1-v) + \alpha_2(u)v\right) \\ r_c \sin\left(\alpha_1(u)(1-v) + \alpha_2(u)v\right) \end{pmatrix} \quad (3.4)$$

where $d_3 = 0.04397947$ m, while α_1 and α_2 are interpolating functions along the pressure side and the suction side respectively.

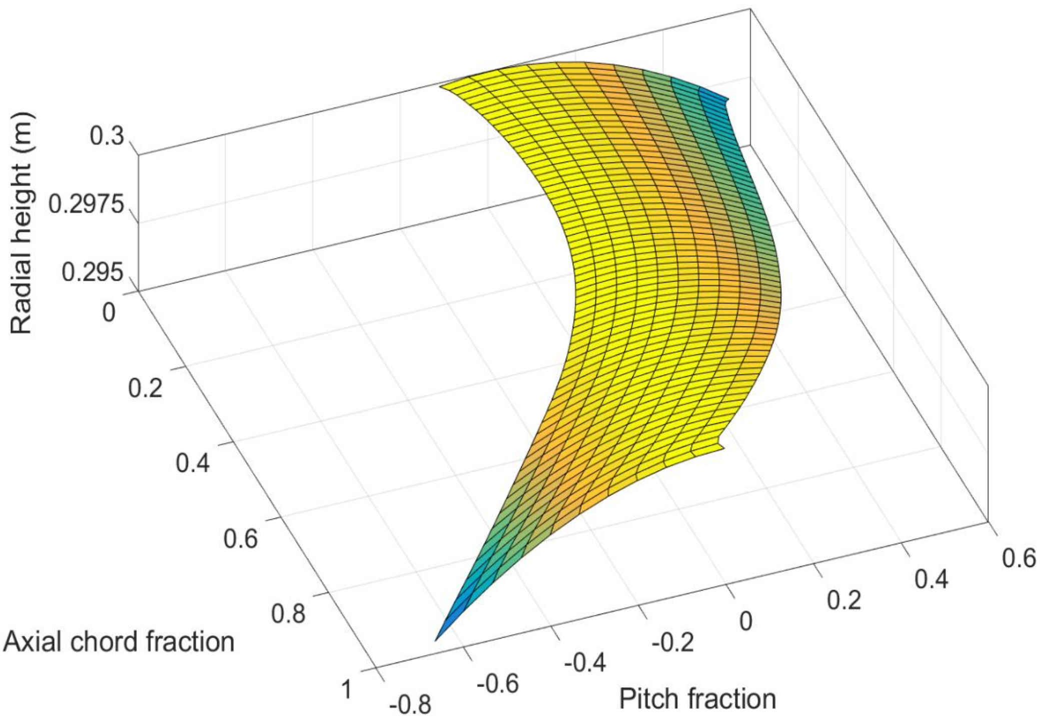

Figure 3-2: Blade to blade casing passage.

Similarly to the inlet casing surface, a third parametrized casing surface of smaller axial extent, 10 mm downstream the stator exit, is implemented to define the casing surface between the stator turbine exit and the location of the mixing plane 1 in Figure 4-5. Figure 3-3 shows this third surface that is defined as:

$$f\ (u, v\ ) = \begin{pmatrix} (1-u)d_3 + u\ d_4 \\ r_c \cos\left(\theta_3(1-v) + \theta_4 v\right) \\ r_c \sin\ \left(\theta_3(1-v) + \theta_4 v\right) \end{pmatrix} \tag{3.5}$$

where $d_4 =$ 0.22997504 m, θ_3=1.5707963 rad and θ_4= 1.745329 rad. The parameters are restricted as $u \in [0, 1]$ and $v \in [0, 1]$. The functions of (3.3), (3.4) and (3.5) are given in Leschke, (2015).

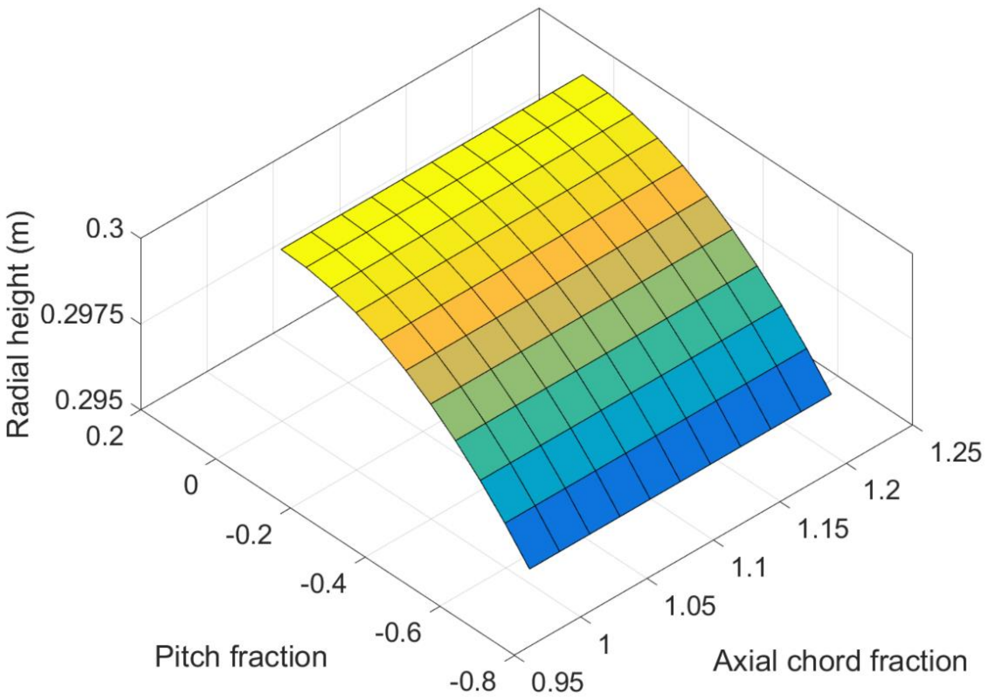

Figure 3-3: Casing passage outlet surface.

Equations (3.3)-(3.5) define a compound cylindrical casing surface $S(u, v)$, which is shown in Figure 3-4 and that has the generalised parametric form:

$$S(u, v) = [u, r_t \cos(v), r_t \sin(v)] \tag{3.6}$$

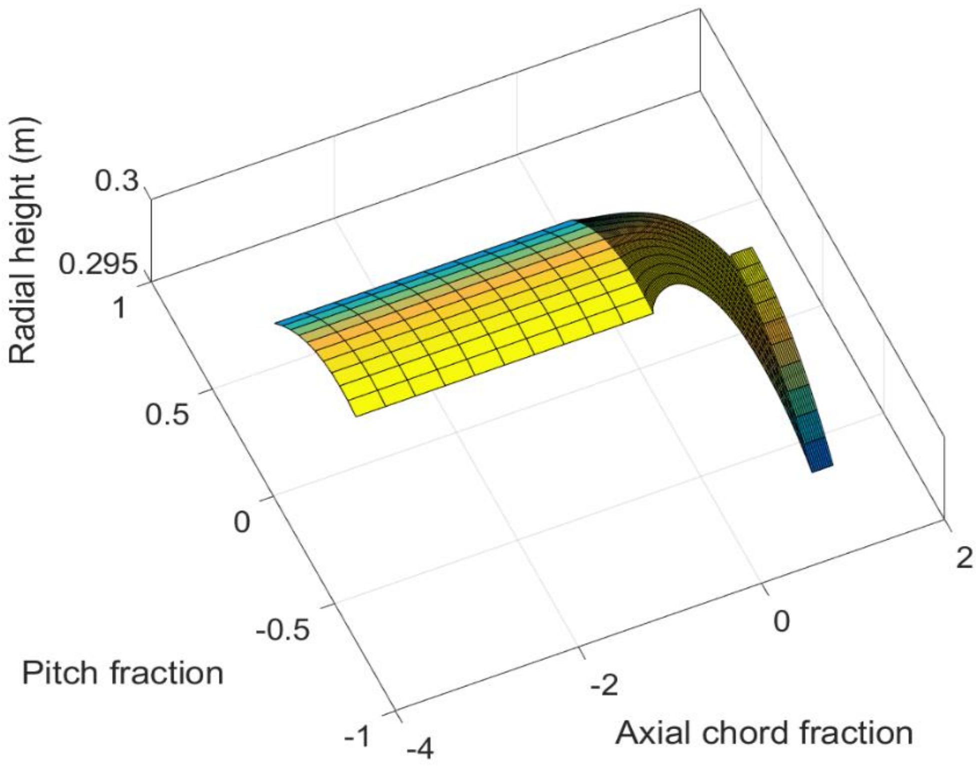

Figure 3-4: The upstream stator casing delimiting one flow passage.

3.3 Non-axisymmetric design requirements

Non-axisymmetric casing surface definitions are sought that satisfy the following five constraints, in order to obtain a smooth and effective geometry output:

1. A surface structure is to be made above a sector of a truncated cylinder, characterised by a tip radius r_t, and an axial length c_x.
2. The maximum surface radial height (r_{tg}) is a small variation of r_t, so that it can be created as a height variation of the truncated cylinder. The mathematical domain of the surface is limited both in the streamwise direction and in the pitchwise direction. The surface is axially confined to start close to the blade leading edges and to end at the mixing plane 1. The pitchwise limits are the blade pressure and suction sides. The geometry is pitchwise periodic, with N blades.

3. The surface radial height and its slope have to be zero at the perimeter. This results in a continuous transition between the profiled endwall and the rest of the passage geometry.
4. The surface structure should be a continuous analytical function $r_{tg} = f(x, s)$ so that it can be evaluated at any position along the axial and pitchwise directions.
5. The surface height distribution should be a real number, and in practice $r_{tg} \leq 3$ mm.

3.4 Guide curves techniques

The guide groove techniques as implemented in this work provide a non-axisymmetric radial deformation of the casing in the blade to blade passage area, as shown in Figure 3-5. The casing surface radial height change shown in Figure 3-5 is produced by guiding curves of the type reviewed in Chapter 2.

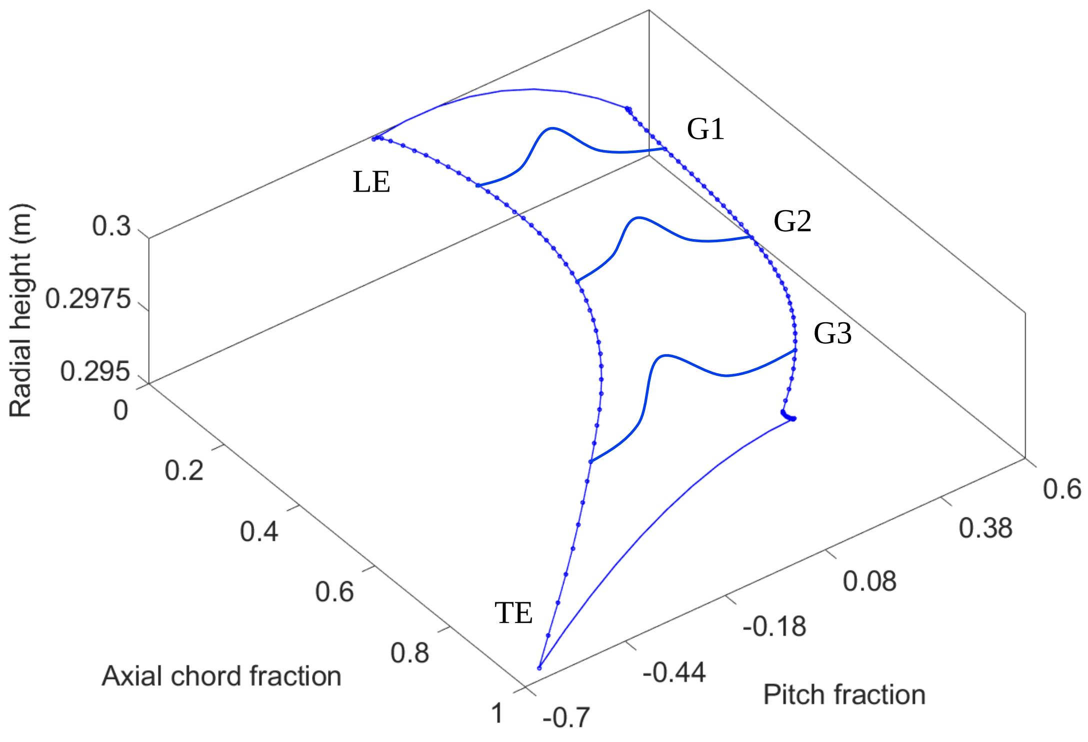

Figure 3-5: Non-axisymmetric radial deformation of the blade to blade casing based on guide curves.

The guide curves are defined using continuous statistical distribution functions, as a discrete statistical distribution function does not meet the constraint number 4 of Section 3.3 (Devore, 2015). As such, the Gauss distribution function and the Beta distribution function are used and their advantages and drawbacks are compared. For the purpose of comparing the geometry obtained by these two continuous statistical distribution functions, the casing is re-sharped just between the leading edge and the trailing edge by a groove running through the middle of the passage pitch. Finally, the surface definition method involving a Beta distribution function is used to define the casing through the full passage of the Aachen turbine, by three abutting Non-Uniform Rational B-spline Surfaces (NURBS).

Three guide curves are distributed axially along the blade passage to construct the turbine casing groove shown in Figure 3-5. Each guide curve is defined by three parameters, namely the pitchwise position of the groove $\mu\ (x)$, the groove pitchwise width σ, and the groove radial depth R_d. These three parameters are illustrated in the Figure 3-6. Based on these parameters, the casing surface groove is defined as depending on 9 adjustable parameters. To construct the complete casing surface, a polynomial curve fit is used between consecutive guide curves in the axial direction, starting from the turbine blade leading edge and ending at the turbine blade trailing edge.

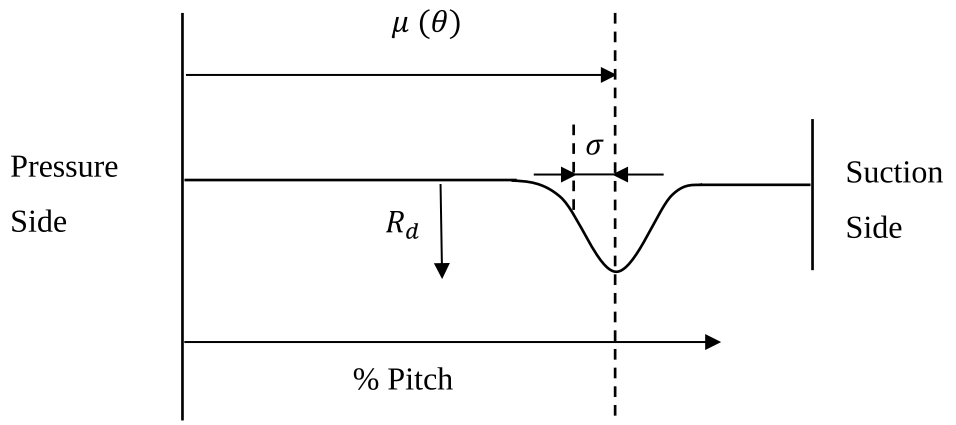

Figure 3-6: Guiding curve parameters.

3.4.1 Gauss guide curve (Gaussian distribution)

The Gaussian (or Normal) distribution is a very common continuous statistical distribution used for numerous applications (Ma, 2011). The casing groove is defined in pitch based on the general form of the probability density function for the Normal distribution:

$$f(l \mid \mu, \sigma) = \frac{1}{\sigma\sqrt{2\pi}}\, e^{-\frac{(l-\mu)^2}{2\sigma^2}} \tag{3.7}$$

where (σ) represents the width of the groove and (μ) is the position of the maximum groove depth at the pitch fraction (l) on the axial plane. It is usual to parametrize this surface as the value of the radius (r_{tg}) in the (x, θ) plane. That is, for any given (x, θ) coordinates, r_t is the casing surface radius on a given axial plane and by substituting θ for x equation (3.7) becomes:

$$f(\theta \mid \mu, \sigma) = \frac{1}{\sigma\sqrt{2\pi}}\, e^{-\frac{(\theta-\mu)^2}{2\sigma^2}} \tag{3.8}$$

Following the procedure reported in Reutter et al. (2013), the groove is defined based on the general form of the Normal probability density function:

$$g(x, s, \mu, \sigma, R_d) = R_d\, e^{-\frac{(s-\mu_x)^2}{2\sigma_x{}^2/\sqrt{n}}} \qquad -\infty < s < \infty \tag{3.9}$$

where $\mu\ (x)$, σ and R_d are the groove parameters of the turbine casing surface and n is an arbitrary number of evenly distributed points along the pitch s. Figure 3-7 shows a sample output from this surface definition method, using R_d = 0.003 m and σ = 0.14, to obtain a casing surface with a groove running down the passage mid-pitch of the Aachen Turbine from RWTH Aachen.

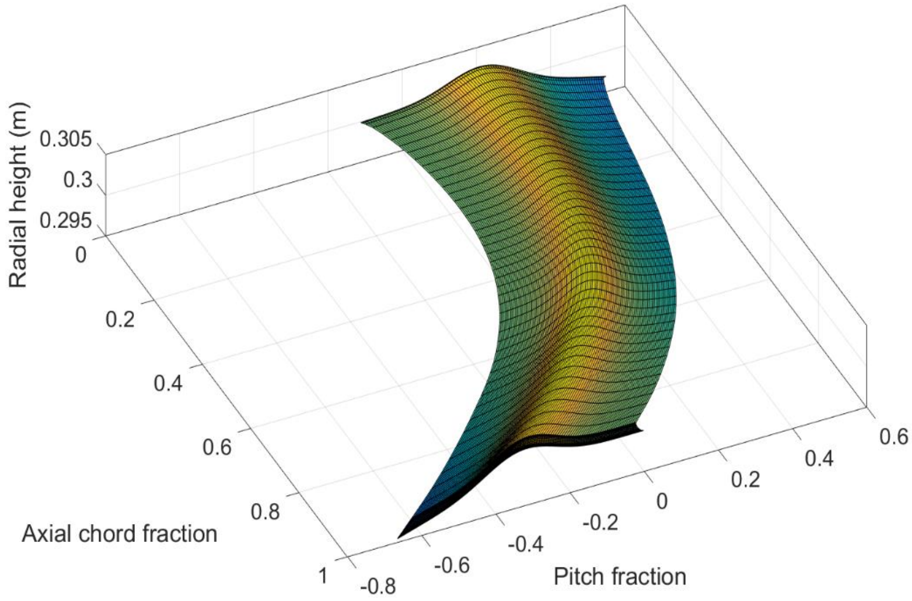

Figure 3-7: Turbine casing surface with a wide groove in the shape of the Normal probability density function.

Figure 3-8 shows the casing contoured using the Normal probability density function to define a narrow groove width down the passage mid-pitch, using R_d = 0.003 m and σ = 0.04.

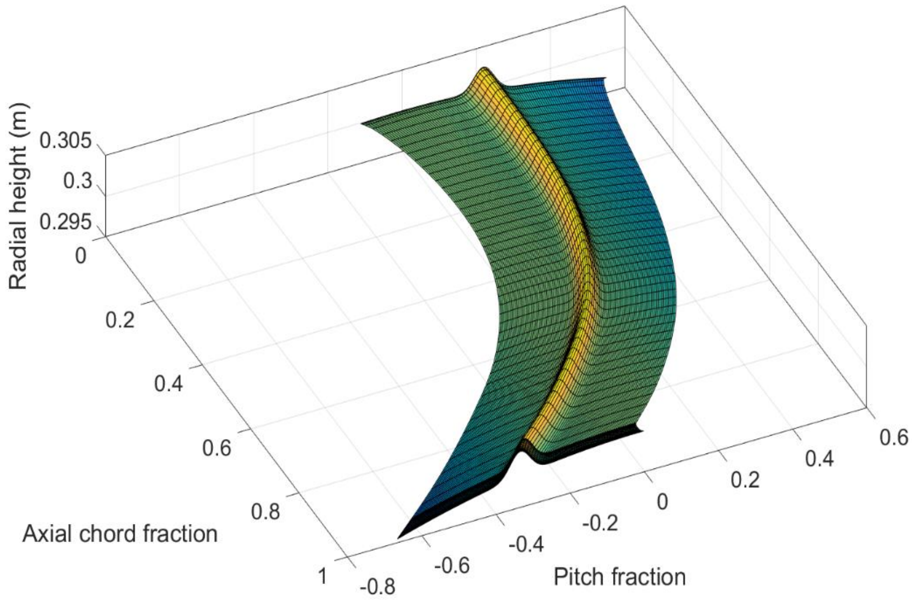

Figure 3-8: Turbine casing surface with a narrow groove in the shape of the Normal probability density function.

3.4.2 Beta guide curve (Beta distribution)

The standard Beta distribution (Devore, 2015) is defined as a function of the shape factor ($\alpha > 0$) and of the scale factor ($\beta > 0$). A variant to the endwall contouring procedure used by Reutter et al. (2013) is considered by replacing the Normal probability density function by the standard Beta distribution function, which is

$$f(x, s, \alpha, \beta) = \frac{\Gamma(\alpha+\beta)}{\Gamma(\beta).\Gamma(\alpha)} s^{\alpha-1} (1-s)^{\beta-1} \qquad 0 < s < 1 \tag{3.10}$$

where $\Gamma(\alpha)$ is the Gamma function defined as

$$\Gamma(\alpha) = \int_0^\infty x^{\alpha-1} e^{-x} dx \tag{3.11}$$

The shape factor (α) and the scale factor (β) can be written in terms of the mean and variance for the Beta probability density function as:

$$\mu = \frac{\alpha}{\alpha+\beta} \tag{3.12}$$

$$\sigma = \frac{\alpha \beta}{(\alpha+\beta)^2 (\alpha+\beta+1)} \tag{3.13}$$

Surface contouring based on the Beta distribution function as a guide curve is applied to the casing of the Aachen Turbine, as shown in Figure 3-9. The contoured casing wall is obtained with the Beta distribution function using $\alpha = 3$ and $\beta = 4$. These parameters generate a groove that is similar to that from using a Normal probability density function with R_d = 0.003 and σ = 0.14, which is shown in Figure 3-7.

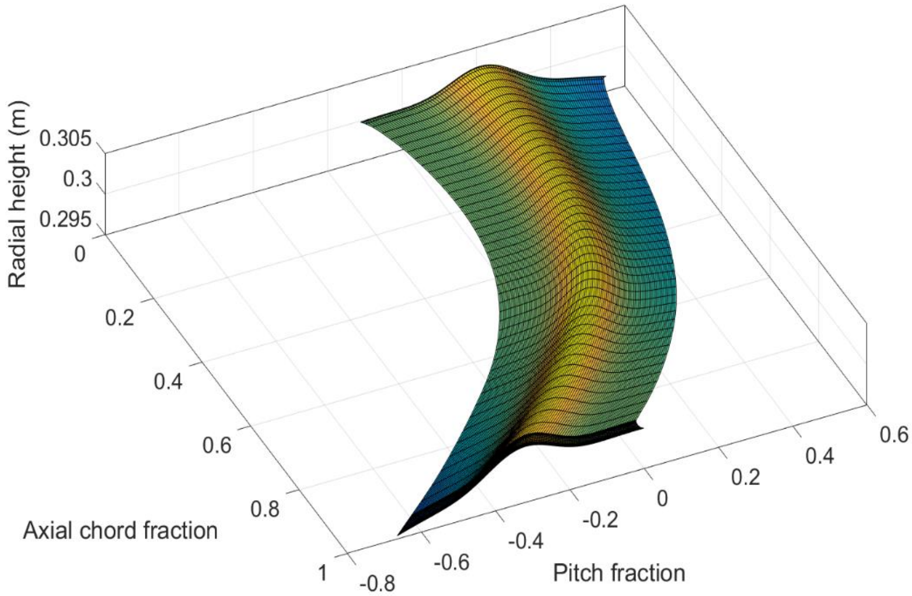

Figure 3-9: Casing surface using a wide groove in the shape of the Beta probability density function.

Similarly, Figure 3-10 shows a narrow groove casing based on the Beta distribution function, corresponding to the groove parameters of the Normal distribution function shown in Figure 3-8.

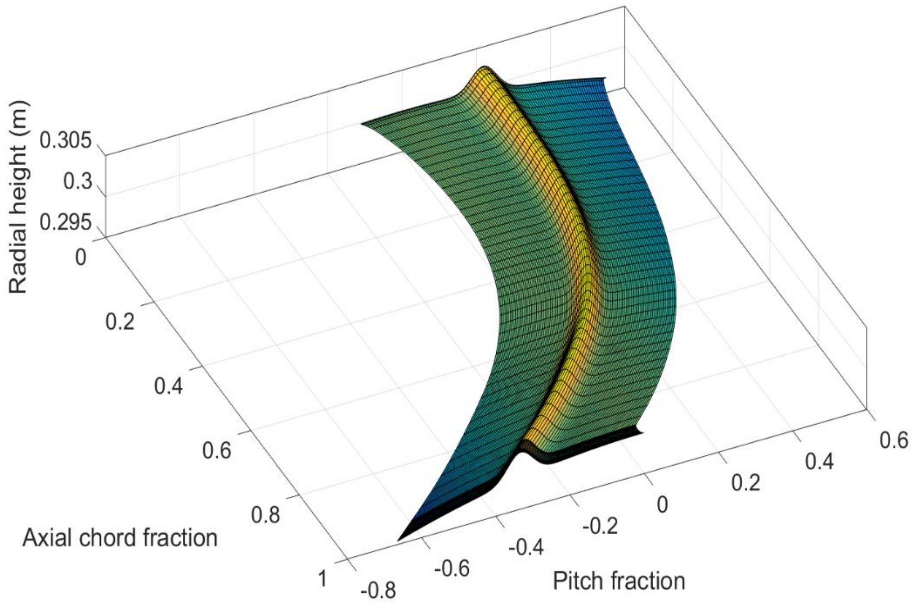

Figure 3-10: Casing surface using a narrow groove in the shape of the Beta probability density function.

3.5 Diffusion design techniques

The upstream and downstream passage inlet and outlet surfaces are parametrized as for an axisymmetric casing in Section 3.2. A parametric diffusion design is applied to the Aachen Turbine casing surface by the use of Bezier curves and of the cosine curve. This generates a hump close to the blade suction side that mitigates the circumferential pressure gradient over the turbine casing passage.

3.5.1 Bezier curves

The Bezier curve is a special case of a NURBS curve that is determined by a control polygon. This curve is found within the convex hull of the control polygon. The control polygon vertices define the largest convex polygon. Three and four point Bezier polygons and the resulting quadratic and cubic curves are used here to create a diffusion casing. Mathematically, a parametric Bezier curve of n-th degree is defined in David (2001) as

$$P(t) = \sum_{i=0}^{n} B_i \, J_{n,i}(t) \qquad 0 \le t \le 1 \qquad (3.14)$$

in which the Bernstein or Bezier basis or blending function is

$$J_{n,i}(t) = \binom{n}{i} t^i (1-t)^{n-i} \qquad (0)^0 \equiv 1 \qquad (3.15)$$

The quadratic Bezier curve is used to define a scaling factor, shown in Figure 3-11, that changes the casing radial height in the pitchwise direction.

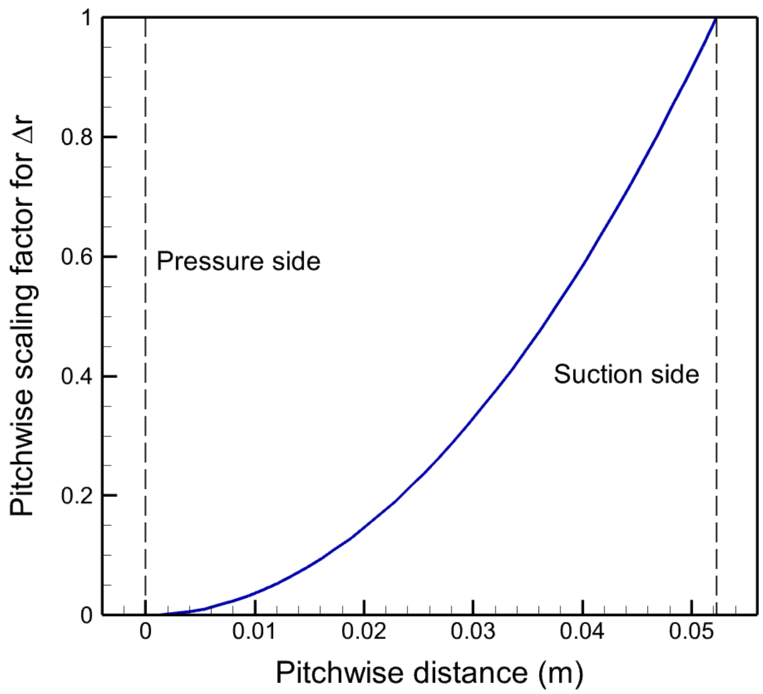

Figure 3-11: The distribution of the pitchwise quadratic Bezier curve.

The cubic Bezier curve of four control points is used to generate a distribution in the streamwise direction, starting from the blade leading edge and ending at the blade trailing edge, as shown in Figure 3-12.

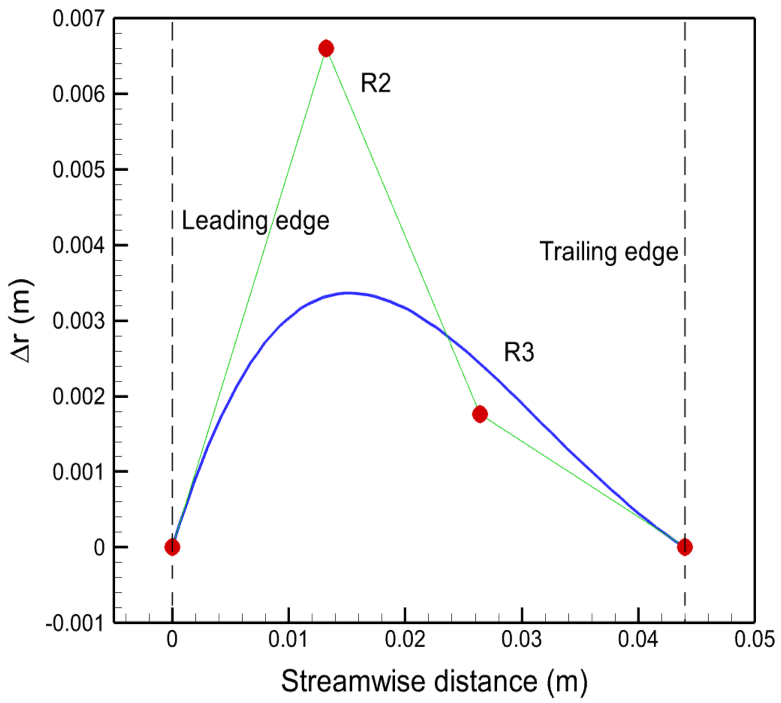

Figure 3-12: Streamwise cubic Bezier curve with control points.

The Bezier surface is determined as the product of the two Bezier functions (cubic and quadratic functions) starting from zero to one:

$$S(t,v) = \sum_{i=0}^{n} \sum_{j=0}^{m} J_{i,n}(t) J_{j,m}(v) B_{i,j} \qquad 0 \le (t,v) \le 1 \qquad (3.16)$$

The cubic curve follows the axial coordinate (x) and the quadratic curve follows the circumferential direction (θ).

Let $t = x$ and $v = \theta$, accordingly equation (3.16) becomes:

$$S(x,\theta) = \sum_{i=0}^{n} \sum_{j=0}^{m} J_{i,n}(x) J_{j,m}(\theta) B_{i,j} \qquad 0 \le (x,\theta) \le 1 \qquad (3.17)$$

The MATLAB software is used to evaluate equation (3.17) to define the casing diffusion design close to the suction side as shown in Figure 3-13.

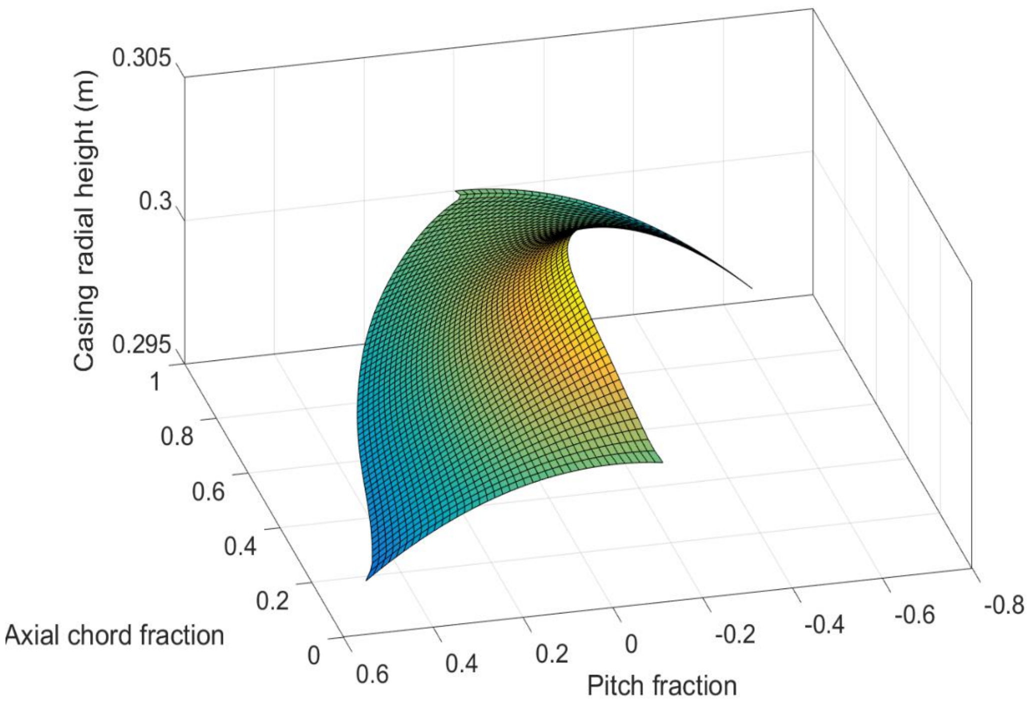

Figure 3-13: Casing surface shape defined by Bezier curves; diffusion design approach.

3.5.2 Cosine curve

The parametric diffusion design method for turbine endwalls reported in Sun et al. (2014) is applied to the Aachen Turbine casing. This design uses a cosinusoidal curve of half period in the circumferential direction as shown in Figure 3-14 (a). The streamwise curve of Figure 3-14 (b) defines the maximum amplitude of the cosinusoidal curve on different axial planes. This streamwise curve is defined as

$$C(R_0, R_1, \dots R_{m-1}, Y_{tran}) = \sum_{i=0}^{k} B_{i,k}(u)\, R_i + (0, Y_{tran}) \tag{3.18}$$

which is a non-uniform B-Spline with 7 control points R_i that are design variables. $B_{i,k}$ is the B-Spline basis, which is defined as

$$B_{i,0}(u) = \begin{cases} 1, u_i \le u \le u_{i+1} \\ 0, \; u \notin [u_i; u_{i+1}] \end{cases}$$
$$B_{i,k}(u) = \frac{u-u_i}{u_{i+k}-u_i} B_{i,k-1}(u) + \frac{u_{i+k+1}-u}{u_{i+k+1}-u_{i+1}} B_{i+1,k-1}(u), k \ge 1 \tag{3.19}$$

u is the knot vector and Y_{tran} is the transition distance in the circumferential direction. The knot vector u and its values u_i are discussed by details in Section 3.6. The B-Spline in the axial direction u combines with the cosinusoidal curve in the circumferential direction v to generate the parametric surface $S(u, v)$.

As shown in Figure 3-14, two control points (R_3 and R_6) are selected as the design variables. These two points control the maximum depth location of the diffusion design, which is most important for mitigating the pitchwise pressure gradient over the casing. A similar placement for R_3 and R_6 is given in Sun et al. (2014), from considerations of the static pressure coefficient distribution. The resulting diffusion parametric surface of $S(u, v)$ is shown in Figure 3-15. More details on the surface parametric equations can be found in Sun et al. (2014).

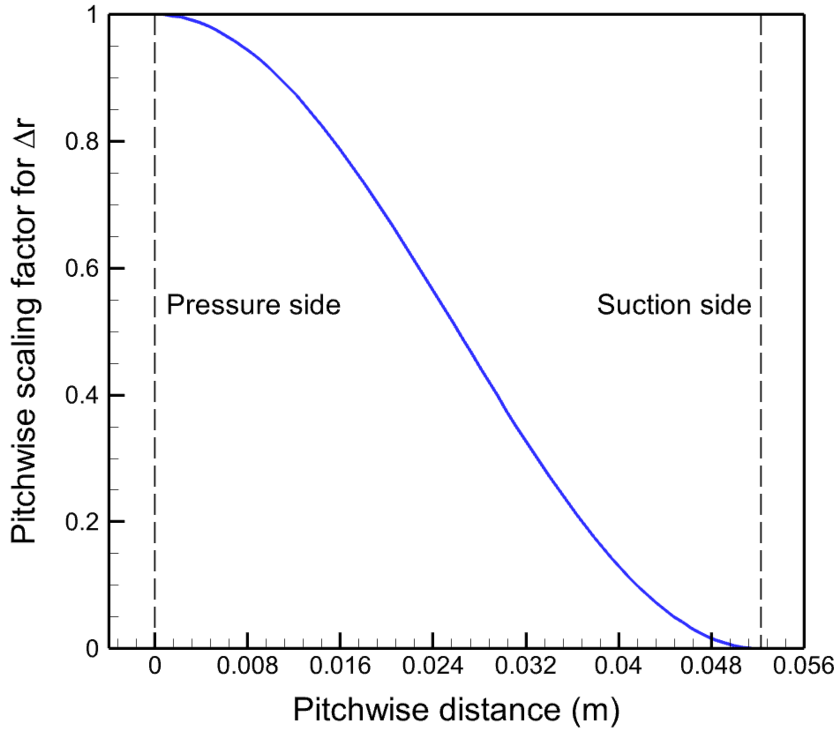

(a)

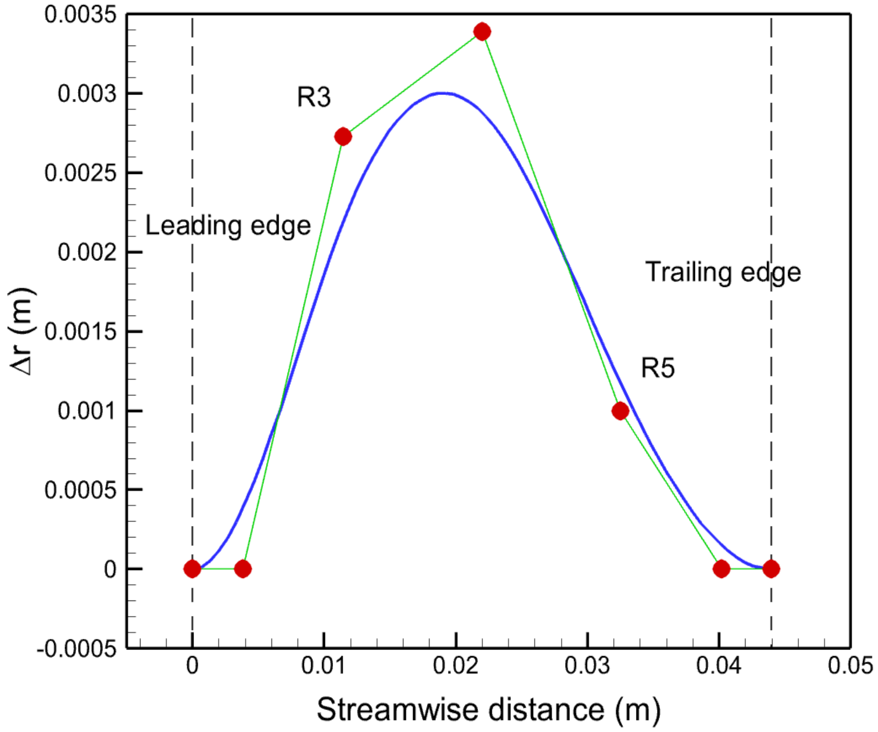

(b)

Figure 3-14: Curves used to generate the casing diffusion surface in the (a) pitchwise and (b) streamwise directions.

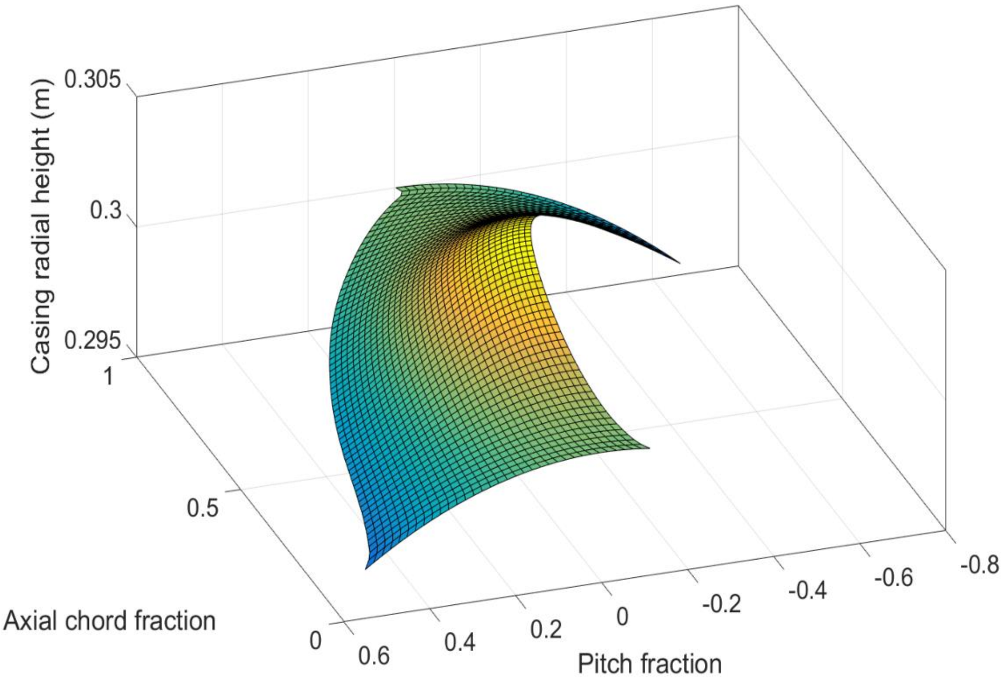

Figure 3-15: Casing surface rendered as a $S(u, v)$ parametric surface, defined to generate a controlled diffusion, as in Sun et al. (2014).

3.6 Non-axisymmetric casing design with a Beta probability density function

The generalized surface $S(u, v) = [u, r_t \cos(v), r_t \sin(v)]$ from Section 3.2 is exported from MATLAB to the ANSYS ICEM CFD based on the NURBS approach.

This approach involves exporting the casing surface as a non-uniform rational B-spline (NURBS) surface. For this purpose, two open uniform knot vectors are used. The number of knots $m + 1$ and of the control points $n + 1$ on the NURBS are related as $m = n + p$, where p is order of the NURBS surface which is restricted to 2 in ICEM CFD. The internal knot values are equally spaced and identified using the parametrization weight according to Piegl and Tiller (2012). The knot vector values are defined as:

$$u_i \ (0 \leq i \leq n + p) \tag{3.20}$$

$$u_i = 0 \text{ if } i < p \tag{3.21}$$

$$u_i = i - p + 1 \text{ if } p \le i \le n \tag{3.22}$$

$$u_i = n - p + 2 \text{ if } i > n \tag{3.23}$$

Three NURBS surfaces were generated and exported as IGES format files, which is a supported input file format of ICEM CFD. By using NURBS surfaces, the cylindrical casing is represented as an exact geometry as it is shown in Chapter 4.

The next step is to define a casing surface with groove with the minimum number of design parameters that still provides a good control on the flow. This entails using a guide flow curve along the streamwise direction rather than that the three pitchwise guides curves that were shown in Section 3.4. The path of the guide curve is defined based on the natural path of the secondary flow features over the turbine casing, which are shown in Chapter 6. This path is defined based on the profiles of the turbine blades, inflated in the cascade plane as shown in Figure 3-16. This is achieved by offsetting the blade perimeter by a set distance a, normal to the blade perimeter as

$$D_i = P_i + n_i a \tag{3.24}$$

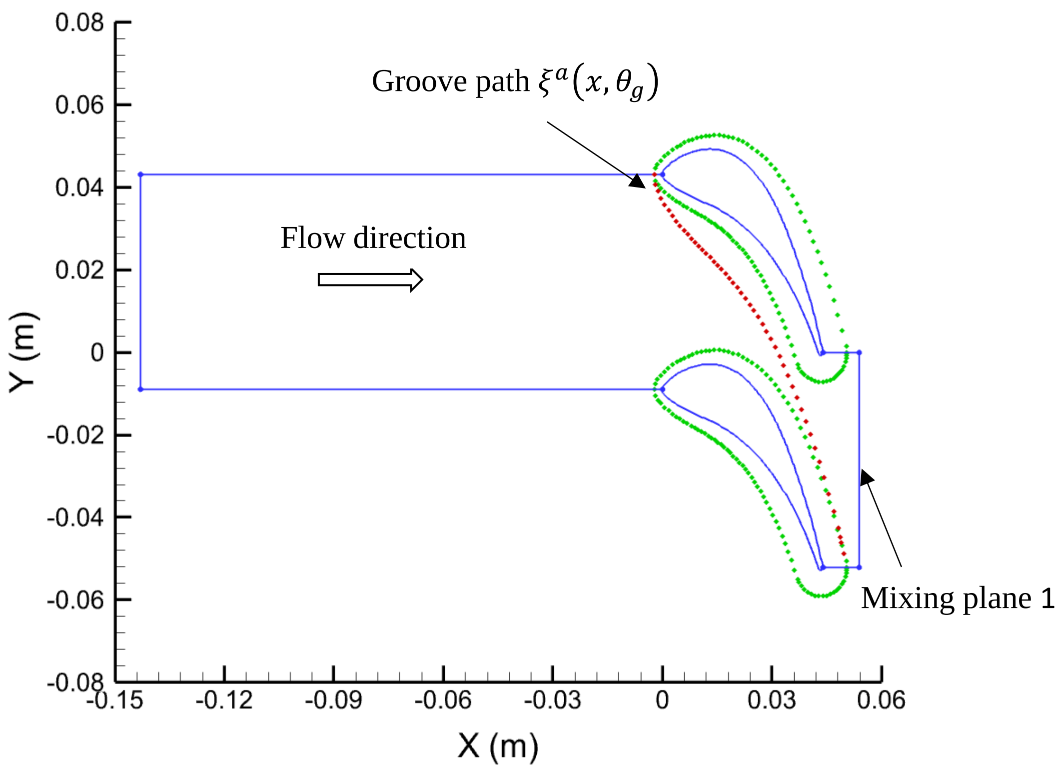

Figure 3-16: Stator blade profiles 'inflated' in the annular cascade casing plane (green) and interpolated groove path (red).

where n_i is the normal vector to casing blade perimeter, defined based on the secant between the lines defined by (P_{i-1}, P_i) and (P_i, P_{i+1}). The subset of D_i is then interpolated using two smoothing splines $d_p(x)$ and $d_s(x)$ on $r = r_t$ to represent respectively the equivalent to the blade pressure side and to the blade suction side.

The groove path $\xi^a(x, \theta_g)$ is then defined by a linear interpolation between the inflated profiles as $\xi^a = c_x d_s(x) + (1 - c_x) d_p(x)$, where c_x is the chord fraction. For each point $P(x, \theta)$ on the casing plane $r = r_t$, its normal distance to the groove path is

$$\eta(x, \theta) = \| \xi^a(x) - P(x, \theta) \| \tag{3.25}$$

The groove depth is defined as

$$g(d, \eta) = h_o d^{-4} (\eta^2 - d^2)^2 \tag{3.26}$$

where d is a set angle in radians from the curve path. The groove width $w = 2d$ varies along the groove path $\xi^a(x, \theta_g)$ as a user-defined free parameter. The groove path starts from upstream of the leading edge and ends at the stator 1 to rotor mixing plane. The mid-width groove depth $h_o(\xi^a)$ along the groove path $\xi^a(x, \theta_g)$ is defined by the Beta distribution function (c.f. Devore (2015)) defined in Section 3.4.2. The maximum groove depth is $r_{tg}/c_x = 0.0682$ and it is located at $\xi^a = \mu$, where $\mu = \alpha(\alpha + \beta)^{-1}$. From this, the stator 1 casing radius is defined as

$$r_{tg}(x, \theta) = \begin{Bmatrix} r_t, & |\eta| > d \\ r_t + g[d, \eta(x, \theta)], & |\eta| \leq d \end{Bmatrix} \tag{3.27}$$

and the stator 1 casing parametric surface is defined as

$$S(u, v) = \left[u, r_{tg}(u, v) \cos(v), r_{tg}(u, v) \sin(v)\right] \tag{3.28}$$

The work aimed at defining a groove depth that could be machined in existing hardware without compromising the passage mechanical integrity and safety. The $r_{tg}/c_x = 0.0682$ maximum groove depth was recommended by industrial collaborator GE Power. Whereas the maximum depth can also be varied, a smaller depth was not tested as it may reduce the guide groove aerodynamic effectiveness, since the geometry reverts back to an axisymmetric surface.

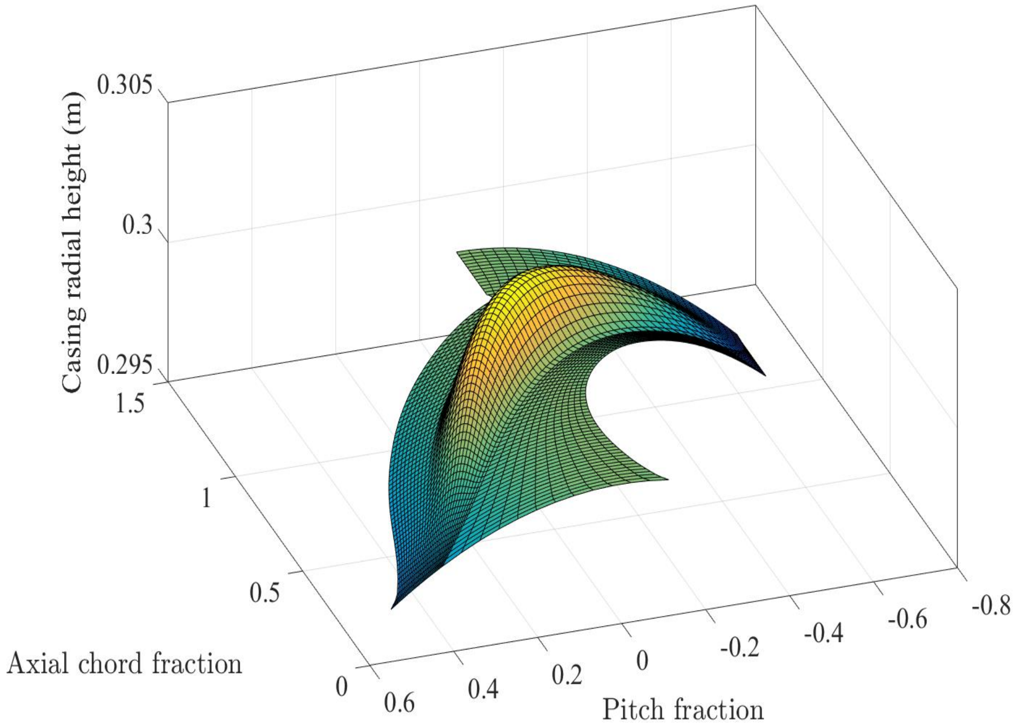

Figure 3-17: Example of casing surface delimiting the upstream stator blade-to-blade passage and the upstream stator passage exit. Composite of two $S(u, v)$ surfaces of which one features a guide groove.

An example of the parametric surface defined by equation (3.28) is shown in Figure 3-17. In the optimization study presented in Chapter 5, three features of the parametric surface are varied, which are the maximum groove depth location along the groove path $\mu\,(x, \theta)$, the groove width at the blade leading edge $w_{le}(x, \theta_g)$, and the groove width at the blade trailing edge $w_{te}(x, \theta_g)$.

3.7 Evaluation of the surface definition methods

The supports or domains of the Normal probability density function and of the Beta probability density function represent an important difference between these two functions. The Beta probability density function domain is defined within the interval $[0, 1]$, while the domain of the Normal probability density function is the interval $(-\infty, \infty)$. As such, the Beta probability density function can taper the groove to zero height at the left and the right bounds (suction and pressure sides) for different values of both α and β. The Normal probability density function can only approximate a zero height at the same bounds within a tolerance of 10^{-16} for the limited range of the groove widths $0 \leq \sigma \leq 0.06$.

This limitation is first illustrated in Figure 3-8 and in Figure 3-10, where the radial height of the casing wall with a groove running down the mid-pitch is shown. Figure 3-8 shows the casing contoured by using the Normal probability density function and Figure 3-10 shows the corresponding result obtained with the Beta probability density function. The two surface definition methods, when used within the above stated groove width limits for the Normal-based surface, give results that are similar in terms of surface smoothness and of the overall surface shape. In practice, either surface definition method can be used for defining the casing wall of the selected test case of Section 4.2.

Using a larger groove width in conjunction with the Normal probability density function as the surface definition method, such as $\sigma = 0.14$, results in an appreciable difference between the pitchwise surface cross-section with respect to the equivalent surface obtained using a Beta probability density function. Figure 3-18 shows this difference $\epsilon = (f_s - g_s)\delta^{-1}$ normalized by a representative surface manufacturing machining tolerance δ = 0.01 mm, which was defined by consultation with the University of Leicester mechanical workshop staff. The groove maximum depth is matched in both surfaces at 50% pitch. Either side of the groove maximum depth, the shoulders of the Normal probability density function are slightly broader than those of the Beta probability density function. The discrepancy between the two profiles remains positive up to the blade suction side and the blade pressure side. However, the profile discrepancy is within the stated manufacturing tolerance and could therefore be ignored for the purpose of the manufacturing of a test cascade.

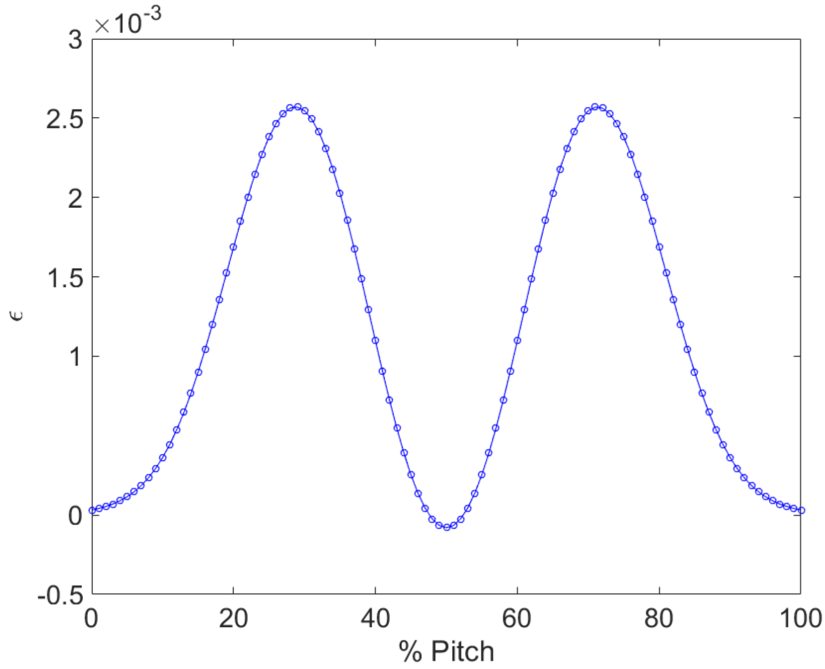

Figure 3-18: Normalized radial difference between casing surfaces generated by the Beta and the Normal probability density functions.

Based on the consideration of the manufacturing tolerance, both the Normal and the Beta probability density functions are available for the next stage of the design process, which is the application of the groove to the casing of the Aachen Turbine. Given that both functions have similar computer wall time costs in MATLAB, it appeared sensible to select the Beta probability density function. This prevented the generation of a 'numerical' gap in the passage geometry which, upon being imported in the mesh generator, would have required patching up, as not to generate voids in the computational domain boundaries.

Section 3.5.1 presented an alternative way of generating a non-axisymmetric casing by a Bezier curve, an example of which was shown in Figure 3-13. The Bezier curve has the elliptic type property that changing any one of its control points will change the entire shape of the curve. This due to the fact that every point on the curve is defined by all control points. This feature may be considered a disadvantage for its application in a design optimization process, as it makes the search for optimized control points a more implicit process. Figure 3-11 and Figure 3-13 show that the Bezier curve has a sharp groove close to the suction side. This causes a discontinuity in slope at the pitchwise periodic boundary, as one casing passage surface abuts to the casing surface of the pitcwhise consecutive passage. Figure 3-14 (a) and Figure 3-15 show that the cosine curve instead provides a zero slope at the suction and pressure sides, therefore avoiding this slope discontinuity at the pitchwise periodic boundaries. The Bezier curve is likewise slope discontinuous at the blade leading edge and the blade trailing edge, as shown in Figure 3-12. The issue of slope discontinuity along the perimeter of the Bezier curve may be alleviated by increasing the order of the Bezier curve. However, this would increase the number of the design parameters and may still not deliver an exact continuity of slope at the axial and pitchwise connections along its perimeter.

The parametric cosine curve method provides a more direct control on the location of the casing maximum height, so that it is possible to define a constant maximum height for the diffusion design, which is more difficult to impose using the Bezier curve. The maximum diffusion height is restricted to 3 mm in this work, as advised by the industrial collaborator GE. The definition of the cosine curve uses a non-uniform B-spline curve in the streamwise direction. The B-spline curve is a composite of a number of segments that are slope continuous at their connections. Due to this segmentation, changing one control point result in changing only part of the curve. This partially decouples the problem of determining the optimal values of the set of control points in the sense that it makes solving for these points a less implicit process.

The review of the parametrization methods presented in this section drew out the main advantages and disadvantages of the different formulations. Based on this analysis, non-axisymmetric casings designed using a groove made by the Beta probability density function and the one defined by the cosine curve using a diffusion approach are identified as the two candidate methods to take onwards to the optimization stage in Chapter 5. These two casing surfaces are both generated as Non-Uniform Rational B-spline Surfaces (NURBS) so that they can be seamlessly imported in ANSYS ICEM CFD, without any surface re-approximation, as is shown in Chapter 4.

Chapter 4

Numerical Models

4.1 Introduction

A numerical approach is pursued for testing the effectiveness of different casing treatments, for which specific numerical models are developed of the flow through a benchmark axial turbine, the Aachen Turbine (Walraevens and Gallus, 1997). Therefore, the salient technical specifications and the running conditions of the Aachen Turbine test case, which was provided by RWTH Aachen, are presented. The computational domains of both the upstream stator cascade and of the one-and-half stage Aachen Turbine are built and discretized by ANSYS ICEM CFD software. The flow solvers of the commercial CFD code ANSYS FLUENT 18 and of the freeware OpenFOAM 3.2 Extend are used to predict the aerodynamic performance of the upstream stator cascade. The OpenFOAM Extend 3.2 solver is then taken onwards for the simulation of the one-and-half stage axial turbine to obtain the three-dimensional (3-D) turbomachinery flow predictions that are presented in Chapter 6. Detailed information on these codes is given in their respective user manuals (ANSYS Inc., 2011) and (OpenFOAM, 2014), in Sanders et al. (2009), and in Jasak and Beaudoin (2011). Therefore, only the information relevant to the specific CFD simulation settings and to the boundary conditions used in this work are provided. The EDDTBL program by Wilcox (1998) is used to generate the turbine casing inflow boundary layer.

The convergence of the computational results is verified through the grid convergence index (GCI) and the convergence criteria defined in section 4.5.1. The CFD predictions are post-processed by bespoke user-defined functions to obtain pitch-averaged profiles of the same format and at the same locations as the ones given in experiment (Walraevens and Gallus, 1997), for comparison. The numerical averaging procedure that is used for this purpose is detailed at the end of this chapter. The computational results are compared with experimental measurements from the Aachen Turbine by RWTH Aachen in Chapter 6.

4.2 The Aachen Turbine test case

Walraevens and Gallus (1997) provide measurements in a 1.5 stage axial turbine that are used for establishing a baseline CFD model of the passage flow. These measurements were acquired downstream of the exit plane of the first stator, of the rotor, and of the second stator, at the stations labelled 1, 2, and 3 in Figure 4-1. Both stators and the rotor have untwisted blades. The geometry of the second stator, the stagger angle, and the number of blades are the same as for the first stator. The rotor blades are unshrouded and have a tip clearance of 0.4 mm. The low aspect ratio blading and the axisymmetric hub and casing geometry result in strong secondary flows. The second stator is clocked three degrees in the direction of rotation. The 1.5 stage was tested at the design point, at a rotational speed of 3500 rpm and at a mass flow rate of 7 kg/s. Cascade and meridional plane schematics of the Aachen Turbine are given in Figure 4-1 and key design data are listed in Table 4-1.

Walraevens and Gallus (1997) report that the rotor speed variation was less than 0.2 percent during testing. They also report that small variations in pressure and in temperature occurred due to the fact that the turbine was controlled in open loop. Pneumatic probes were used to measure the steady-state flow field properties behind all blade rows (stator 1, rotor, and stator 2). This includes the use of five-hole probes in the core flow region and of three-hole probes close to the hub and casing walls. Walraevens and Gallus (1997) moved the probes in the circumferential and radial directions in the measurement planes 1-3 to survey the local flow. These probes are placed 8.8 mm downstream the exit planes of stator 1, of the rotor, and of stator 2 as shown in Figure 4-1. The probes are traversed in a pitchwise sector to cover 17 radial lines with a height of 53 mm. Each probe line has 38 radial points, ranging from a radius of 246 mm to a radius of 299 mm. Each 38-point dataset constitutes one pitchwise averaged radial line. The measurements at plane 0, located 143 mm upstream of the inlet plane of the stator 1, were taken from a radius of 249 mm to a radius of 296 mm, therefore no measurement is available across the inflow endwall boundary layers. The probe measurements have an uncertainly of $\pm$ 1% in velocity and of $\pm$ 0.5 degrees in flow outlet angle.

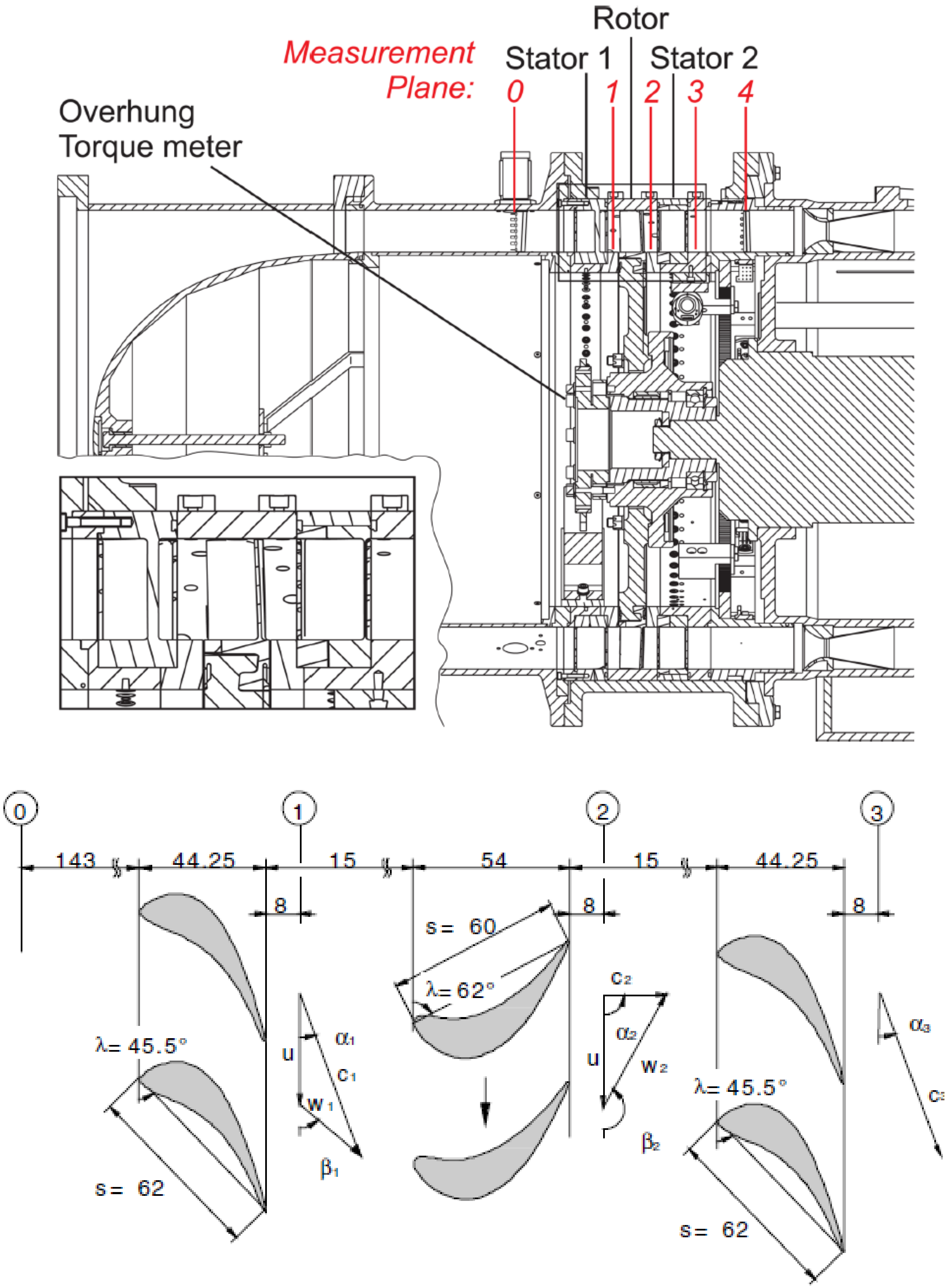

Figure 4-1: Schematic of the cross-sectional view of the Aachen Turbine and detailed geometry, from Walraevens and Gallus (1997). All dimensions are in mm.

Table 4-1

Design data of the Aachen Turbine test case.

Parameters	Values	
	First and second stator	Rotor
Tip diameter	600 mm	600 mm
Hub diameter	490 mm	490 mm
Passage height, h	55 mm	55 mm
Aspect ratio, h/s	0.887	0.917
Blade number	36	41
Tip clearance	-	0.4 mm
Midspan blade pitch, s	47.6 mm	41.8 mm
Inlet flow angle measured from the axial plane	90.0°	20.0°
Design rotational speed, $\dot{\theta}$	-	3500 r.p.m.
Exit Reynolds number	6.8×10^5 and 6.9×10^5	4.9×10^5
Exit Mach number	0.4298 and 0.5048	0.1544

4.3 Computational domains and mesh generation

In order to perform numerical simulations of the Aachen Turbine, a case, or input file, needs to be prepared by performing appropriate pre-processing steps that include the geometry and mesh generation. The pre-processing steps are performed for both a single stator row and a one-and-half stage axial turbine respectively in Section 4.3.1 and in Section 4.3.2.

4.3.1 Upstream stator cascade of the Aachen Turbine

The computational domain of a single stator row is generated using ANSYS ICEM CFD 18 software. The stator blade profile is obtained by fitting a B-spline through the profile geometry points provided by RWTH Aachen. The blade profile is stacked radially at the trailing edge so that the stagger angle ζ is constant, due to the absence of blade twist in the spanwise direction.

The stator blade profile is tabulated in Walraevens and Gallus [16] as 116 points in two dimensions, each is given by a set x, y and z coordinates. These are mapped to a cylindrical reference system (x, r, θ), where x is the axis of rotation, r is the radial distance from x, and θ = 0 is through the stator blade trailing edge. The blade geometry is defined by two aerofoils that are located on the blade tip at r_t and on the hub at r_h.

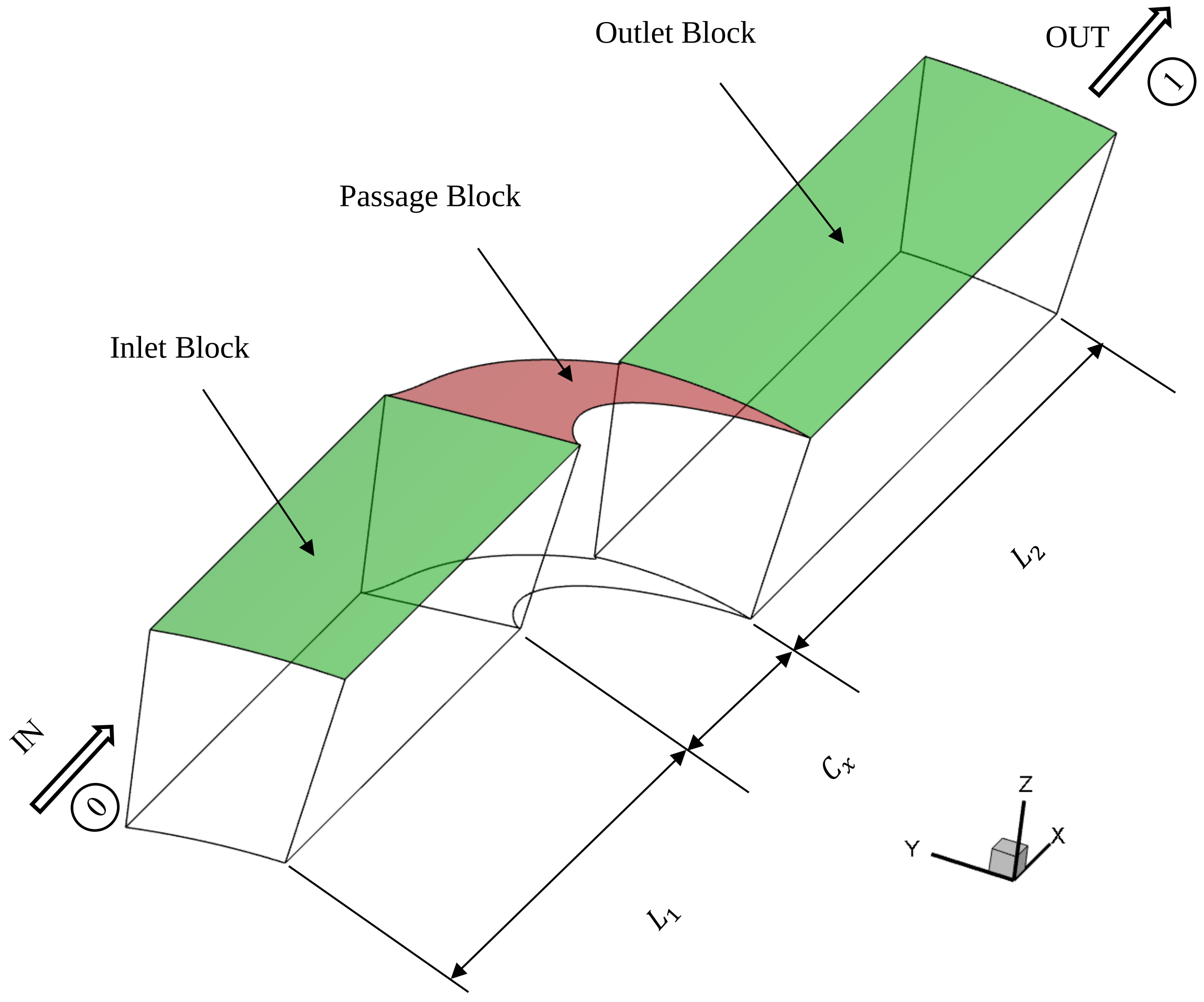

Figure 4-2: Mesh blocks with cylindrical casing surface as a composite of three $S(u, v)$ parametrized surfaces imported in ICEM CFD.

The computational domain is pitchwise periodic and only one blade pitch around the annulus is modelled, in order to reduce the computational effort. Following this approach, pitchwise boundaries and the axisymmetric hub and casing that define the stator passage geometry are generated. The passage volume is initially divided into three blocks to obtain a structured mesh topology, which typically lends itself to a better near-wall mesh quality control than an unstructured mesh set-up. The three blocks are referred to as the inlet, passage, and outlet blocks in Figure 4-2. The domain extends by $L_1 = 3.25$ axial chords upstream of the stator blade leading edge, and by $L_2 = 4.23$ axial chords downstream of the stator blade trailing edge. The axisymmetric casing parametric surface which is generated in Chapter 3, Section 3.2, is exported as an IGES format file and imported to ANSYS ICEM CFD as shown in Figure 4-2. The imported casing consists of three surfaces located within the passage volume blocks: the inlet surface, the blade to blade passage surface, and the outlet surface, respectively.

The computational domain is built in ICEM CFD as the volume enclosed by the inlet, outlet, hub, casing, blade, and periodic boundaries, as shown in the Figure 4-3. This computational domain is then discretised into an assembly of control volumes, or unit cells, to form the computational mesh. A fine mesh is required to capture all three-dimensional flow features with an acceptable level of accuracy at an affordable computational cost. This is usually not easy to accomplish, particularly for highly twisted turbine blades. The structured and unstructured mesh generation options in ICEM CFD were both considered in order to achieve a mesh of satisfactory quality. Whilst an unstructured mesh enables to discretize more complex geometries, it is often considered not as good as a structured mesh for boundary layer calculations, since the latter enables to align the numerical fluxes tangent to the wall with the unit cell boundary normal vectors. This enables the spatial differentiation scheme to attain its formal accuracy, in the absence of shocks. In ICEM CFD, there is a helpful feature that allows the production of a hybrid mesh, which includes a prism mesh, or structured mesh, near walls to satisfy the y^+ requirements. However, the casing wall optimization procedure described in Chapter 5 requires the selection of a mesh that attracts a relatively low computational cost, so that a large number of flow simulation can be afforded. Although the hybrid mesh provides a reasonably good surface mesh, the computational time was estimated to be longer compared to a structured mesh topology. In addition, the use of periodic boundaries with an unstructured mesh is more difficult than with a structured mesh, as it requires identical cyclic mesh boundaries. Therefore, a hybrid mesh was not used in this work.

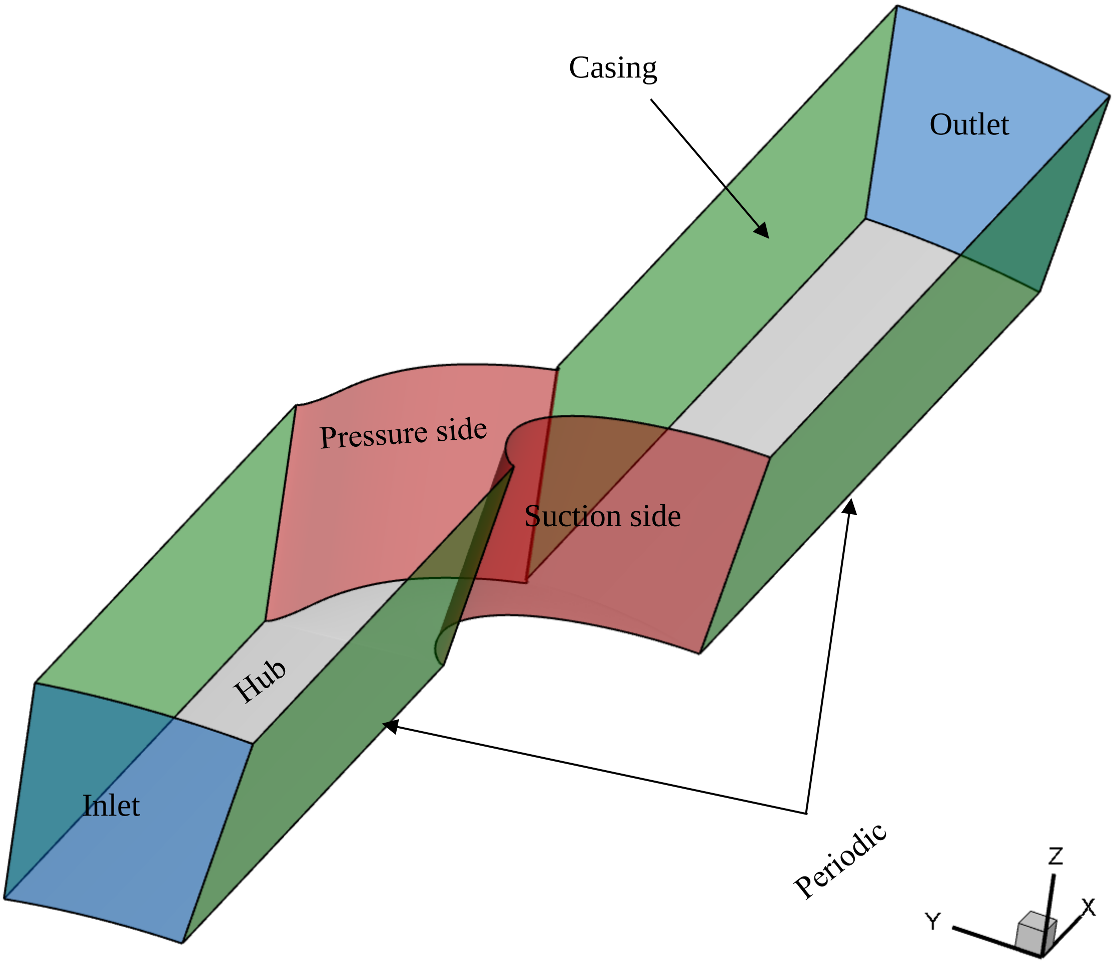

Figure 4-3: Illustration of the computational domain for the stator 1 of the Aachen Turbine.

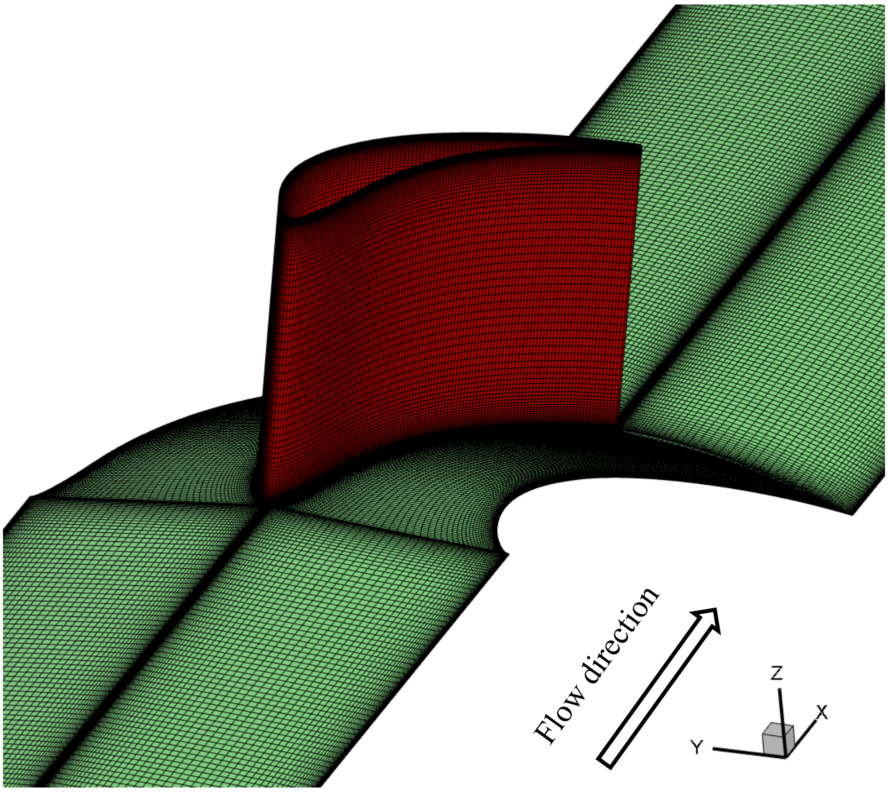

Figure 4-4: Detail of the 3-D computational mesh for the Aachen Turbine stator 1.

ANSYS ICEM CFD 18 is used to discretize the computational domain using hexahedral unit volumes. Whereas the mesh topology is structured, the mesh is exported in the .msh unstructured mesh format to ANSYS Fluent, which is the mesh input format required by this software. A simple H-mesh topology is applied to these passage blocks as shown in Figure 4-4. This covers one blade passage per blade row and a second passage is added in Figure 4-4 for clarity.

To minimise the numerical error associated to the spatial discretization, the mesh points are clustered near the leading edge and near the trailing edge. Furthermore, mesh points are clustered with a starching ratio of no more than (1.1) in order to resolve the boundary layers over the blade, the hub, and the casing. The cells adjacent to solid walls have a wall-normal height of 0.00005 m, for spanwise-normal walls, and of 0.00007 m, for pitchwise-normal walls. This gives an average value of $y^+ \approx 1$, which is the recommended y^+ value in the Fluent and OpenFOAM user manuals.

4.3.2 The one and half stage Aachen Turbine

The computational domain of a one and half stage Aachen Turbine is also generated using ANSYS ICEM CFD 18 software. This computational domain is shown in Figure 4-5. The rotor blade geometry is obtained following the same procedure to obtain the blade geometry of the stator 1 turbine cascade. The rotor blade is stacked radially at its centroid that is located at x = 25.265 mm and y = 13.456 mm from the blade leading edge. The rotor blade profile is tabulated in Walraevens and Gallus [16] as 133 points in two dimensions. The second stator profile has the same profile as the first stator. The second stator passage is divided into three blocks as for the stator 1 turbine cascade. Four blocks are used to define the rotor flow passage, three of which are arranged as for the stator 1 turbine cascade. The computational domain pitchwise and radial boundaries for the second stator blade passage are the same as the one used for the upstream stator cascade passage of Figure 4-3. The computational domain boundaries for the rotor blade passage are shown in Figure 4-6.

A simple H-mesh topology defines the first and second stator blade passages. The multi-block topology of an H-mesh combined with an O-mesh defines the rotor blade passage. The rotor tip clearance is accounted for by adding a block pitchwise, as shown in Figure 4-5, labelled as ‘Tip clearance block’. The tip clearance block uses a combination of an H-mesh and of an O-mesh similar to the one around the rotor blade. The O-mesh surrounds the rotor blade aerofoil in the cascade plane and the H-mesh fills the remainder of the rotor blade passage. In order to be able to calculate the flow through the rotor tip gap, a good local spatial resolution is required. This is achieved by defining 17 equally spaced cells in the radial direction between the rotor blade tip and the rotor casing to capture the tip leakage flow. The mesh points of the rest of the rotor passage and for the stator 1 and stator 2 are clustered close to the solid walls in the same way as for the stator 1 cascade simulation described in Section 4.3.1. This is done to resolve the boundary layer flow over the blade, the hub, and the casing of each passage. The stretching ratios and the first cell size in the spanwise and pitchwise directions are similar to the ones used for the stator turbine cascade mesh. These mesh clustering criteria provide a near-wall resolution of $y^+ \approx 1$, as verified by the yPlusRAS -compressible utility function of OpenFOAM 3.2 Extend.

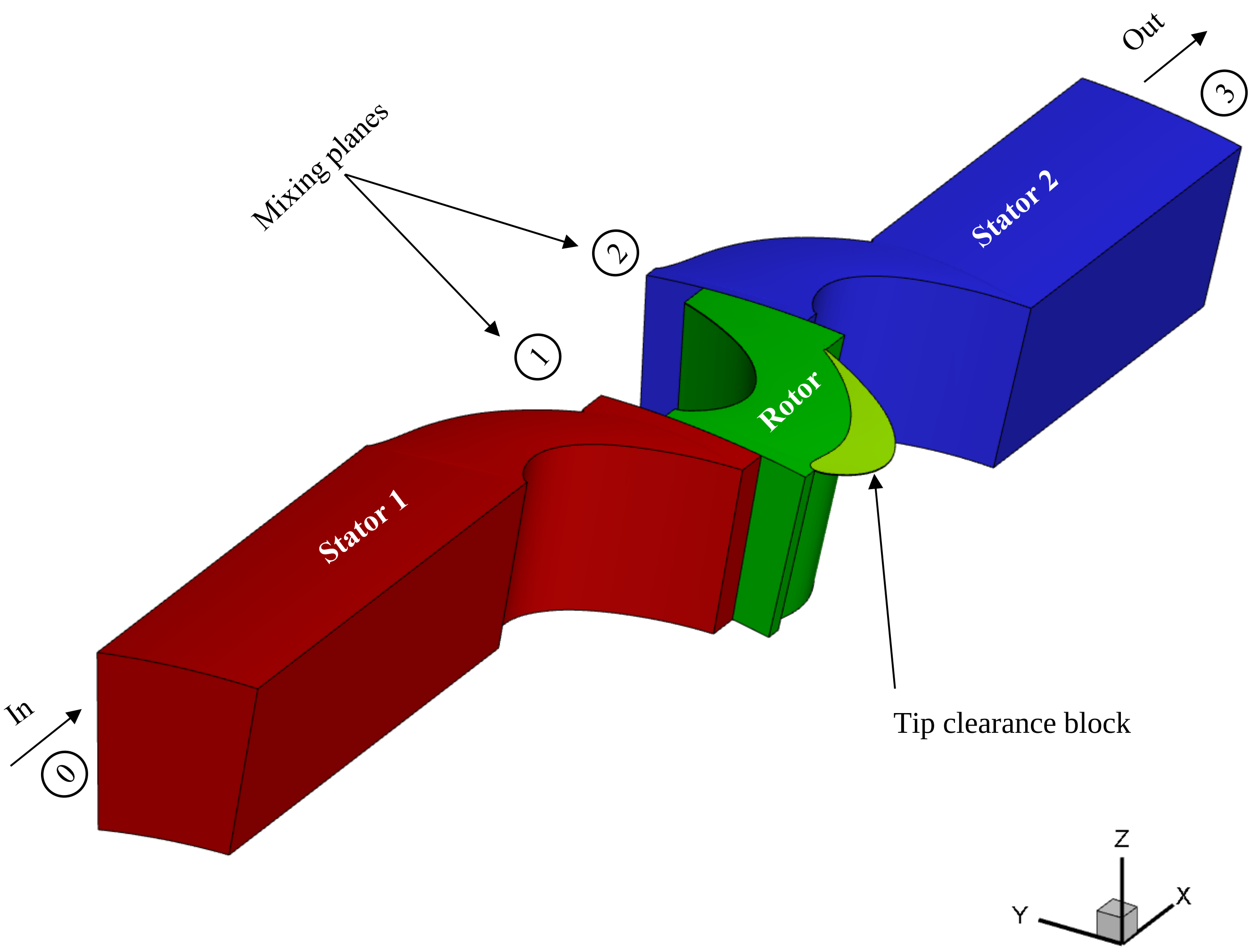

Figure 4-5: Schematic of the 1.5 stage turbine flow passage of the Aachen Turbine.

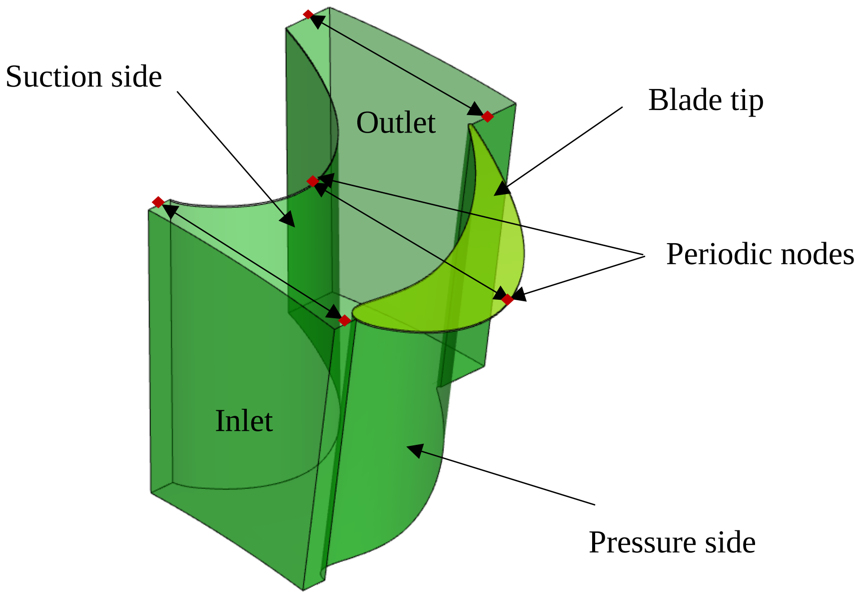

Figure 4-6: Computational domain boundaries of the rotor passage of the Aachen Turbine.

Figure 4-7 shows the resulting computational mesh. This covers one blade passage per blade row and a second passage is added in Figure 4-7 for clarify. The mesh has 5,699,688 cells and it has about the same spatial resolution at that of the intermediate mesh for the turbine cascade of Section 4.3.1.

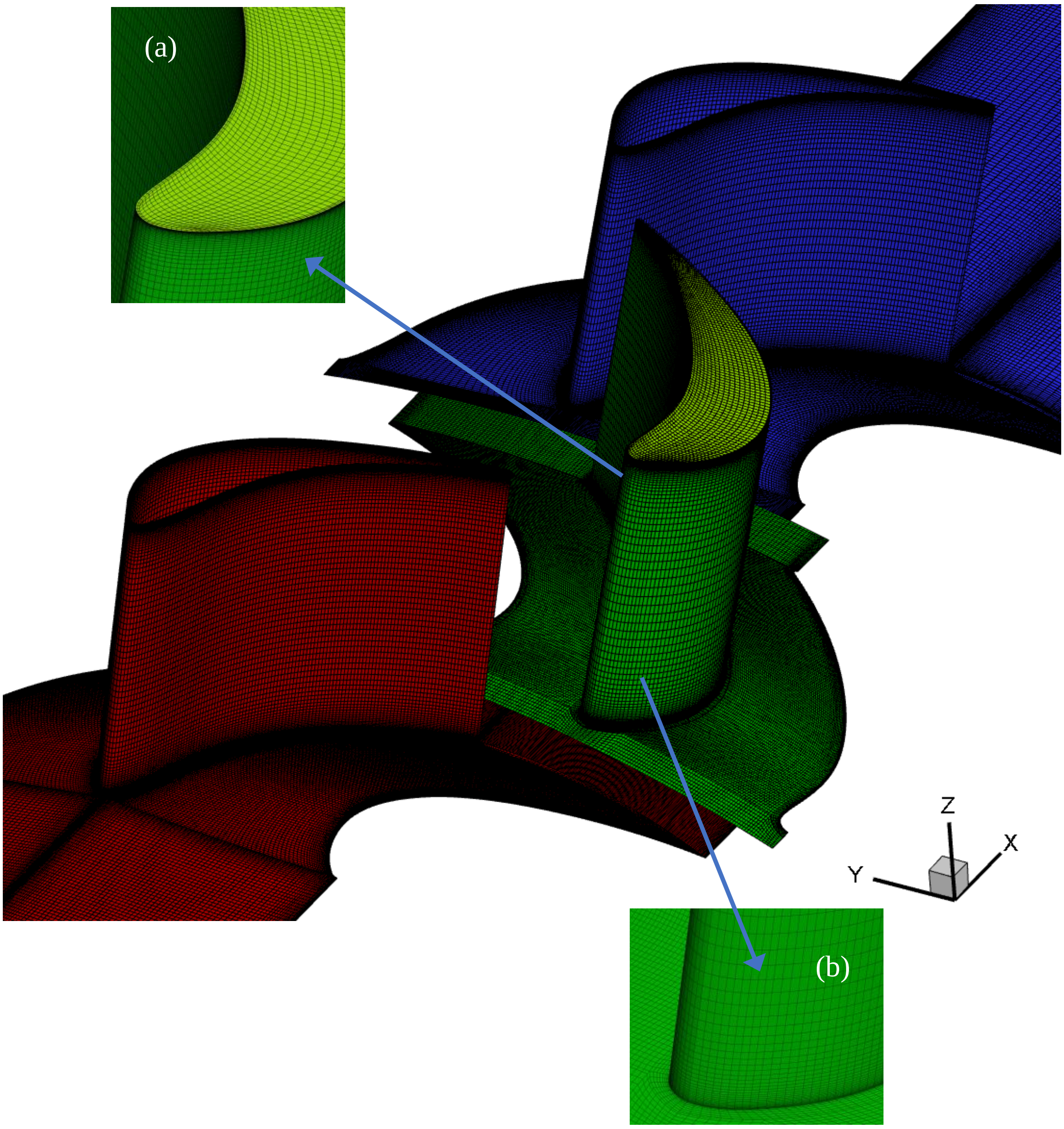

Figure 4-7: Three-dimensional computational mesh for the Aachen Turbine RANS simulation. Mesh details close to the rotor (a) casing and (b) hub.

The mesh shown in Figure 4-7 discretises the baseline Aachen Turbine passage with an axisymmetric casing. Non-axisymmetric casing variants of the baseline Aachen Turbine are built by replacing the axisymmetric casing by its non-axisymmetric equivalent from Chapter 3. This is generated as a complement of three Non-Uniform Rational B-spline Surfaces (NURBS) and it is imported in ANSYS ICEM CFD as shown in Figure 4-8 and Figure 4-9. Figure 4-8 shows a non-axisymmetric casing with a guide groove, designed according to Section 3.6, bounding the computational domain of Aachen Turbine. Figure 4-9 shows a non-axisymmetric casing, shaped by the diffusion design technique of Section 3.5.2, bounding the same computational domain. Insets are used to provide an enlarged view of the casing surface mesh at the guide groove leading and trailing edges and at the corresponding locations over the diffusion designed casing. These enlargements give a qualitative appreciation of the author's effort of resolving the guide groove shape with a dense carpet mesh as well as of building as smooth as possible mesh junctions between blocks.

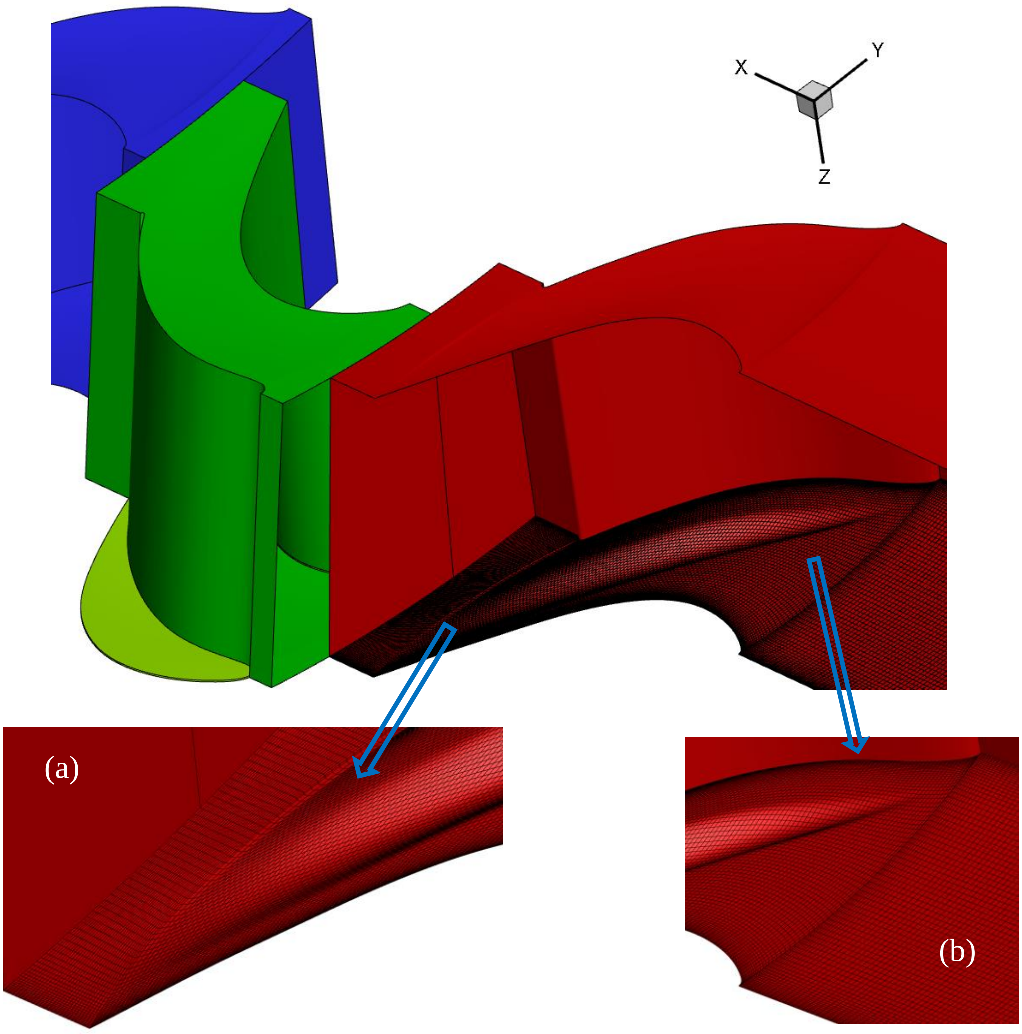

Figure 4-8: Non-axisymmetric groove casing NURBS imported in ANSYS ICEM CFD. Mesh details close to (a) the groove trailing edge and (b) the groove leading edge.

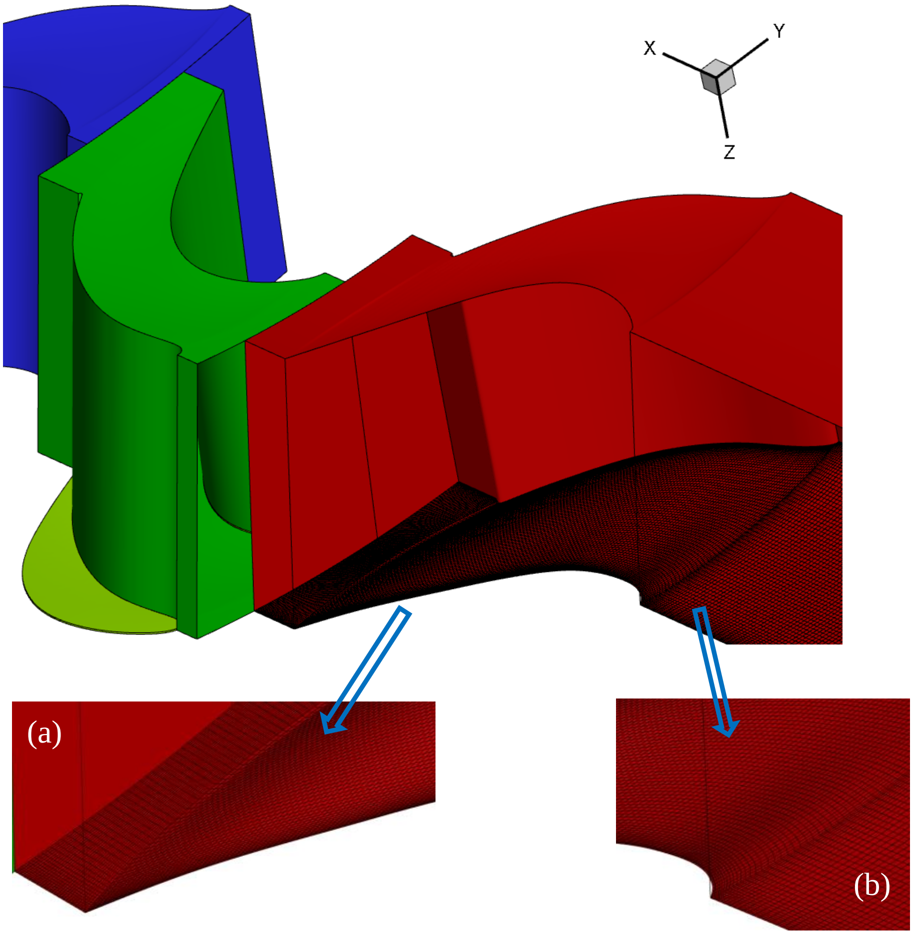

Figure 4-9: Non-axisymmetric diffusion casing NURBS imported in ANSYS ICEM CFD. Mesh details close to (a) the blade trailing edge and (b) the blade leading edge.

4.4 RANS Solver: ANSYS Fluent and OpenFOAM

The motion of a fluid is governed by three partial differential equations that represent the conservation laws of mass, motion, and energy. A direct numerical solution approach to these equations is, at present, computationally too expensive, given the Aachen Turbine flow Reynolds number reported in Table 4.1 and that the cost of such a computation scales approximately as Re^3. To circumvent this problem, the conservation laws are Reynolds averaged in time, so that only the time-invariant flow state is resolved in space and the unsteady flow effects on the mean flow are simulated by a turbulence model. The simultaneous solution of the Reynolds averaged conservative laws is required to solve a turbine flow field.

ANSYS Fluent 18 and OpenFOAM 3.2 Extend are used to solve the Reynolds Averaged Naiver-Stokes (RANS) equations for the turbine flow field of the stator cascade. ANSYS Fluent 18 is an implicit, finite-volume solver, which includes two kinds of solvers; the pressure based solver and the density based solver. The pressure based solver is selected for this simulation as it is applicable from a low speed incompressible flow to a high-speed compressible flow (ANSYS Inc., 2011). The semi-implicit method for pressure-linked equations (SIMPLE) is used with second order upwind scheme by Van Leer (1979) for the discretisation of the governing equations.

OpenFOAM is a licence-free open source library for Computational Fluid Dynamics (CFD) that provides a direct access to the flow models and to the numerical solvers within it (Beaudoin et al., 2014). OpenFOAM 3.2 Extend is a community-driven version of the CFD package OpenFOAM. Similar features to that mentioned in ANSYS Fluent 18 are available in OpenFOAM Extend, together with other tools developed for handling turbomachinery flow analysis, such as a Multi-Reference Frame (MRF) and a General Grid Interface (GGI). The pressure-based steadyCompressibleMRFFoam solver is implemented with the pressure-correction procedure PIMPLE. Turbine cascade predictions from OpenFOAM 3.2 Extend and from ANSYS Fluent 18 are compared against published experimental measurements from RWTH Aachen in Chapter 6. The discrepancy between the measurements and the predictions from OpenFOAM 3.2 Extend is marginally lower than that from ANSYS Fluent 18, as shown in Chapter 6. Whereas in practice these discrepancies are comparable, OpenFOAM 3.2 Extend is taken onwards for the simulation of the one-and-half stage axial turbine of Chapter 6, also in view of the more favourable conditions on the software license that allows OpenFOAM simulations to use more than 16 cores. The 16 cores were a limit of the ANSYS Fluent 18 academic licence.

The MRF library in OpenFOAM 3.2 Extend provides a steady-state modelling tool for turbomachinery simulations (Jasak and Beaudoin, 2011). This library enables to model a rotor passage in its rotating frame of reference as a steady flow. The rotation of the flow is accounted for by adding convective transport terms in the governing equations to the rotating zone cells. These convective transport terms model the centrifugal and Coriolis forces.

GGI is a feature of OpenFOAM designed for handling the communication and the interpolation of the numerical fluxes through non-conformal mesh boundaries. Such boundaries are obtained were mesh nodes mis-match either side of a multi-block domain interface. In turbomachinery, the GGI feature in OpenFOAM is used to reduce the computational cost, by modelling one blade passage. Specifically, a cyclic GGI interface is used to impose pitchwise periodic boundary conditions as sketched in Figure 4-3. This is achieved by coupling corresponding nodes as sketched in Figure 4.6. These pitchwise periodic nodes are determined by the $2\pi/Nb$ rotational symmetry of the blade row, where Nb is the number of blades in the stator, for a pitchwise periodic boundary of a stator row, and in the rotor, for a pitchwise periodic boundary of a rotor.

The ANSYS ICEM CFD unstructured mesh is converted to OpenFOAM by the Fluent3DMeshToFoam pre-processor of OpenFOAM. The mesh is checked for quality and for build errors by the checkMesh utility of OpenFOAM. The boundary conditions and the inter-block connectivity of the multi-block mesh are defined in a 'patch file' written in the system directory of the OpenFOAM simulation. The patch file prescribes the treatment of geometrically discontinuous connectivity patches across the periodic boundaries and the mixing planes. The setSet-batch setBatchGgi utility functions are used to create interface faceSets for the periodic boundaries and at either side of the mixing plane. These sets are transformed into zones by the setsToZones-noFlipMap utility function.

A 4760 cores High Performance Computer (HPC) cluster at the University of Leicester was used for running the simulation. The simulation wall time was reduced compared to a scalar computation by MPI parallelization. The parallel computation was set up in ANSYS Fluent 18 by partitioning the computational domain by domain decomposition in 16 sub-domains, using the METIS algorithm.

In OpenFOAM 3.2 extend, a similar domain decomposition approach was used. The computational domain was first split by the decomposePar utility function, which created a decomposeParDict file created in the system directory of OpenFOAM, to handle the communication across the partitioned domain. Three different domain decomposition tests were carried out with 20, 30, and 50 processors. Using 30 processors was found heuristically to give the fastest combined queue time and execution time on the HPC cluster, which is a shared resource. The MPI version of OpenFOAM 3.2 Extend was used as the flow solver.

Table 4-2

The scalability test results based on different set of processors.

No. of processors	Run time (sec)	Speed-up
1	397939.5	-
20	60424	6.586
30	49308	8.071
50	53340	7.46

The scalability test results were used just as a guidance for the appropriateness of the level of domain decomposition as shown in Table 4-2. The length of the actual runs was affected by concurrent jobs sharing the same nodes and competing for memory resources on the HPC shared cluster, which generated daily variations in the wall time of similar runs. As the scalability test was performed not on a specific segregated set of nodes, as the HPC cluster is in constant use, the results should be considered for guidance purposes only.

The above procedure is used for both the turbine cascade simulations and for the one and half stage turbine simulation. The OpenFOAM steadyCompressibleFoam solver is used for the turbine cascade and the steadyCompressibleMRFFoam solver for the one and half stage turbine.

4.4.1 Turbulence modelling

The selection of the turbulence model is case-dependent in Computational Fluid Dynamics. It typically depends on factors including the target accuracy, the specific application, and the computational resources. Several different turbulence models are available in ANSYS Fluent 18 and in OpenFOAM 3.2 Extend. In this work, turbulence closure is achieved based on the two-equation Shear Stress Transport (SST) turbulence model (Menter, 1994), for both the stator row and the one and half stage turbine. This turbulence closure model was selected as it is relatively computationally inexpensive compared to other turbulence closure approaches, such as LES, and has been validated for turbomachinery flows including flows exhibiting boundary layer separation. It attempts to combine two of the most commonly used turbulence models: the $k - \omega$ model and the $k - \varepsilon$ model. The general idea is for the SST model to follow the behaviour of the $k - \omega$ turbulence model in the near wall regions and that of the $k - \varepsilon$ turbulence model away from the walls.

The $k - \omega$ SST model uses two transport equations, the first for the specific turbulent kinetic energy k and the second for specific turbulent kinetic energy dissipation rate ω:

$$\frac{\partial}{\partial t}(\rho k) + \frac{\partial}{\partial x_i}(\rho k u_i) = \frac{\partial}{\partial x_j}\left[\left(\mu + \frac{\mu_t}{\sigma_k}\right)\frac{\partial k}{\partial x_j}\right] + G_k - Y_k \quad (4.1)$$

$$\frac{\partial}{\partial t}(\rho \omega) + \frac{\partial}{\partial x_i}(\rho \omega u_i) = \frac{\partial}{\partial x_j}\left[\left(\mu + \frac{\mu_t}{\sigma_\omega}\right)\frac{\partial w}{\partial x_j}\right] + G_\omega - Y_\omega + D_\omega \quad (4.2)$$

where G_k represents the production of the specific turbulent kinetic energy k, G_ω represents the production of the specific turbulent kinetic energy dissipation rate ω, Y_k and Y_ω represent respectively the dissipation of k and of ω due to the turbulence. D_w is a cross-diffusion term introduced by Menter (1994). σ_k and σ_ω are turbulent Prandtl numbers.

Whereas the majority of the simulations presented in this thesis use the $k - \omega$ SST model, it was of interest to explore the effect of changing the turbulence closure model on the predictions of the one and half stage Aachen Turbine. For this purpose, the Re-Normalization Group (RNG) $k - \varepsilon$ turbulence model is also used. This model is based on a re-normalisation of the Naiver-Stokes equations that aims to give an improved turbulence closure performance over a wider Reynolds number range compared to the $k - \varepsilon$ model. The RNG $k - \varepsilon$ model has been used to investigate the secondary flows of an axial turbine by many researchers, such as Wang et al. (2014), Hilfer et al. (2012) and Hermanson and Thole (2002). The RNG $k - \varepsilon$ model uses the two transport equations

$$\frac{\partial}{\partial t}(\rho k) + \frac{\partial}{\partial x_i}(\rho k u_i) = \frac{\partial}{\partial x_j}\left[\alpha_k \mu_{eff} \frac{\partial k}{\partial x_j}\right] + G_k - \rho\varepsilon \quad (4.3)$$

$$\frac{\partial}{\partial t}(\rho\varepsilon) + \frac{\partial}{\partial x_i}(\rho\varepsilon u_i) = \frac{\partial}{\partial x_j}\left[\alpha_\varepsilon\,\mu_{eff}\,\frac{\partial\varepsilon}{\partial x_j}\right] + C_{1\varepsilon}G_k\,\frac{\varepsilon}{K} - \rho C_{2\varepsilon}\frac{\varepsilon^2}{k} - R_\varepsilon \qquad (4.4)$$

where G_k, is same term as that of the standard $k-\omega$ turbulence closure model, while α_k and α_ε are inverse effective Prandtl numbers for k and ε. A more comprehensive description of the renormalization group method and of the RNG $k-\epsilon$ model can be found in (Yakhot and Orszag, 1986).

4.4.2 Stator-Rotor interface modelling

Due to the complex geometry of a turbomachine, it is computationally expensive to obtain a numerical mesh of satisfactory quality for the entire turbomachine. Furthermore, rotor and stator blade rows create alternating regions bounded by stationary walls and by mainly rotating walls. Therefore, the computational domain is typically split into more than one region. For instance, the current single passage of a one and half stage axial turbine is simulated based on numerical meshes created for the first stator, the rotor, and for the second stator. The rotor and stator meshes must be connected in a suitable way. This requires the exchange of boundary data between the stator-rotor-stator blade rows. Two methods of modelling the interface between the passages are available in OpenFOAM 3.2 Extend: the direct overlapGgi method and the averaged mixingPlane method. In this thesis, the mixingPlane method is used to model the stator-rotor-stator interfaces, as this approach is widely used for steady-state simulations in turbomachinery.

4.4.2.1 Mixing planes

For the steady-state simulation of axial turbine flows, the mixing plane approach has been used extensively. In this approach, the flow is assumed to be largely mixed out in the gap between two consecutive blade rows (Du and Ning, 2016). The mixing plane technique does not require abutting meshes to match pitchwise either side of the interface. A one-time loss of information associated with mixing results from the application of a mixing plane filter. Nevertheless, this approach is extremely useful in a practical turbomachinery simulation, as it is allows the unsteady flow through a stage to be modelled by steady-state numerical techniques, with the use of MRF (Beaudoin et al., 2014). In this work, the interactions between the first stator passage, the rotor passage, and the second stator passage are modelled using two mixing planes as shown in

Figure 4-5 and in Figure 4-10. Figure 4-10 shows the geometric correspondence between the first stator outlet (red) and the rotor inlet (green) through mixing plane 1. It also shows the layout between the rotor outlet (green) and the second stator inlet (blue) through mixing plane 2. The radial height of corresponding circumferential strips of cells is maintained across the mixing plane, whereas their circumferential positions differ.

Basically, the first stator, the rotor, and the second stator computational domains are solved independently. The flow properties such as static pressure, velocity and temperature are circumferentially averaged at the first stator outlet and the rotor inlet, either side of mixing plane 1. The same circumferential averaging is performed at the rotor outlet and the second stator inlet, either side of mixing plane 2. The circumferential averaged properties are then assembled into numerical fluxes that are exchanged across the mixing planes.

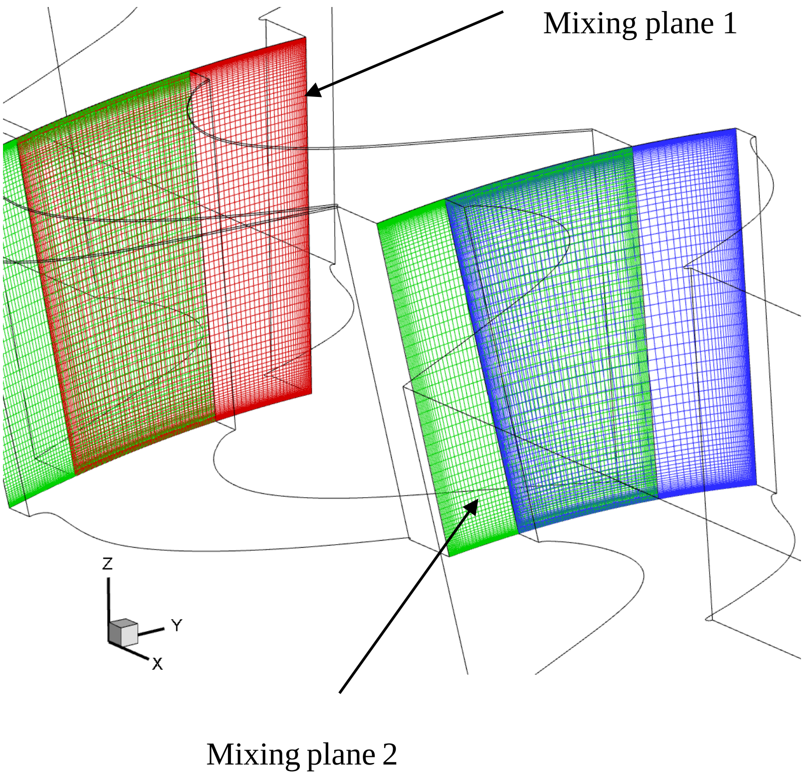

Figure 4-10: Meshes at mixing planes. One and a half stage Aachen Turbine model.

Area averages of the static pressure, velocity, temperature, of the specific turbulent kinetic energy, and of the specific turbulent kinetic energy dissipation rate are performed over circumferential rings one unit cell wide in the radial direction. The mixing planes 1 and 2 are located at 10 mm axially downstream of the first stator and 10 mm axially downstream of the rotor, respectively. This axial positioning of the mixing planes allows monitoring the exit flow from the first stator and from the rotor just upstream of the mixing planes, at the same locations as in the experiment by RWTH Aachen.

4.5 Simulation settings and boundary conditions

The boundary conditions are defined in the computations to closely represent the geometry and the flow conditions in the experiment by RWTH Aachen, as far as possible. The flow is modelled as dry air, under ideal gas and constant specific heat assumptions. The specific heat ratio γ = 1.4, the specific gas constant $R = 287$ J kg^{-1} K^{-1}, and the dynamic viscosity is estimated by Sutherland's law.

At the computational domain inlet, the spanwise distributions of the experimental inlet average total pressure and total temperature are imposed. In addition, a fully developed inflow compressible boundary layer profile is imposed at the inlet over the casing. This profile is generated by the EDDYBL program of Wilcox (1998) and includes profiles of turbulent kinetic energy and of specific dissipation rate of specific turbulent kinetic energy. At the computational domain outlet, the radial profile of static pressure measured in experiment is imposed.

The computational domain inlet velocity is set in the x-direction to give an axial inflow and an absolute inlet flow angle of 90 degrees measured from the axial plane. At the domain outlet, the velocity is extrapolated by the OpenFOAM InletOutlet boundary condition, which is by default a zeroGradient boundary condition.

The hub, the casing, the rotor tip, and the blade surfaces are modelled as no-slip adiabatic walls. Pitchwise periodic boundary conditions are imposed over the remaining boundaries. In particular, pitchwise periodic boundaries are used for modelling the tip leakage flow, as shown in Figure 4-6. The rotor blades are stationary in the rotor frame of reference, which rotates at the constant rotor shaft speed stated in Table 4-1. This includes rotating the rotor blade suction side, the rotor blade tip, and the rotor blade pressure side. The mixing plane formulation by Jasak and Beaudoin (2011) was used downstream of the stator and of the rotor exit planes, as stated in Section 4.4.2.1.

The operating conditions used from the experimental measurements are listed in Table 4-3. Table 4-3 shows the boundary conditions of three experiments as performed at RWTH Aachen. These experiments documented respectively the first stator, the rotor, and the second stator exit flow conditions. The small change in the ambient conditions and/or in the set-up of the test rig results in three different sets of the average inlet total pressure, rotor shaft speed, and of average static exit pressure. Therefore, each experiment represents a separate validation test case for the numerical model.

Table 4-3

Boundary conditions of three validation test cases.

Boundary conditions	Validation test case		
	Stator 1	Rotor	Stator 2
Average inlet total pressure [Pa]	152776.55	155055.45	153786.83
Average outlet static pressure [Pa]	107500	110050	113910
Rotor shaft speed [r.p.m.]	3505	3500	3496

The same inlet and outlet boundary conditions are applied in both ANSYS Fluent 18 and in OpenFOAM 3.2 Extend. For the ANSYS Fluent18 simulation, a boundary profile file is imported to define the inlet boundary conditions. This type of file format is also used to define the outlet boundary condition profile. In OpenFOAM 3.2 Extend, a bespoke subroutine adapted from the CFD Online repository (CFD Online, 2005) was compiled and linked to the OpenFOAM library, to define non-uniform inlet and outlet boundary conditions. This subroutine uses an interpolation procedures to impose profiles of flow properties at all finite-volume faces at the inlet and at the outlet. The profiles are applied to represent the casing inlet boundary conditions as shown in Figure 4-11 (a-c), in which y represents the radial distance from the casing towards the hub. Across the inlet, at $y > \delta$, the uniform conditions of Table 4-3 are used. Figure 4-11 (a) shows the dimensionless velocity and the temperature ratio. Figure 4-11 (b, c) show respectively the dimensionless turbulent kinetic energy and the dimensionless turbulence length scale. The outlet static pressure profile is defined based on the experimental measurements as shown in Figure 4-11 (d).

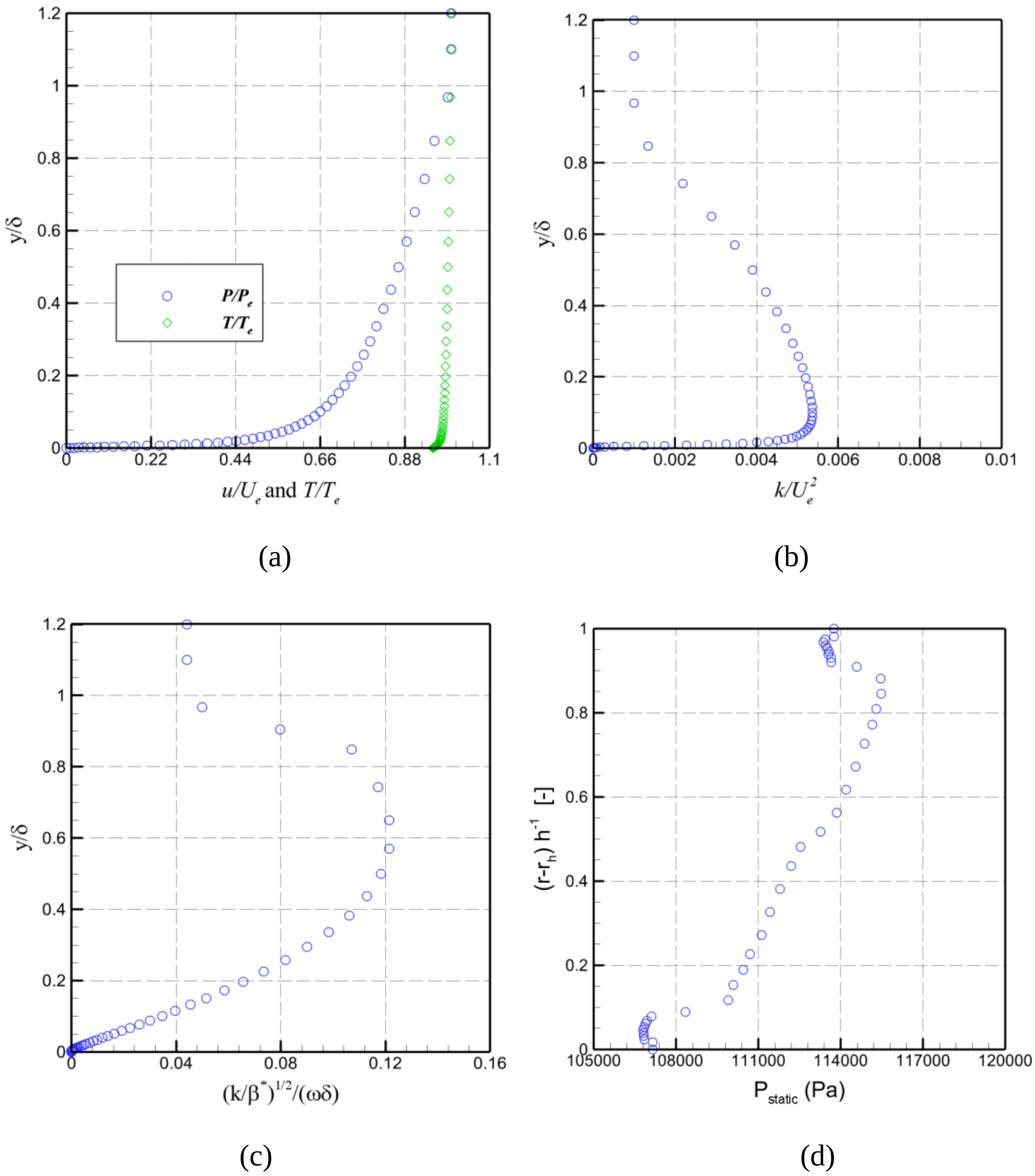

Figure 4-11: Casing boundary layer profiles obtained from the EDDYBL program of Wilcox (1998).

The compressible, two-dimensional, turbulent boundary layer from the EDDYBL program, which provides the axisymmetric inflow profile in the one-and-half stage simulation, is built by using the following experimental measurements as free-stream conditions:

- Inlet average total pressure P_{t0}: 152.776 kPa
- Inlet average total temperature T_{t0} : 307.18 K
- Inlet Mach number, M_0: 0.1181
- Reynolds number, Re_x: 2.14225×10^6

The EDDYBL program also requires to input the momentum thickness Reynolds number, the shape factor, and the skin friction coefficient. These boundary layer integral properties are calculated based on the above free-stream properties and based on correlations as used in (Kundu et al., 2012). The turbulent kinetic energy dissipation rate is calculated based on k and ω according to Wilcox (1998) as $\varepsilon = \beta^{*}\omega\, k$, where β^{*} = 0.09. Detailed information about the EDDYBL program is available in Wilcox (1998).

The inlet boundary layer over the Aachen Turbine casing is much thicker compared to the hub. This is due to the fact that the casing inlet boundary layer develops along the cylindrical entrance of the test rig while the hub boundary layer develops only along the short cone that accelerates the flow in the test rig shown in Figure 4-1. Therefore, the hub boundary layer profile is not modelled in this study, as shown in Figure 4-12, as it is assumed to have a comparatively small effect on the turbine secondary flow features over the casing. Figure 4-12 shows the spanwise inlet boundary conditions of the pressure and temperature. This includes inlet profiles at the casing with a uniform value along the rest of the span.

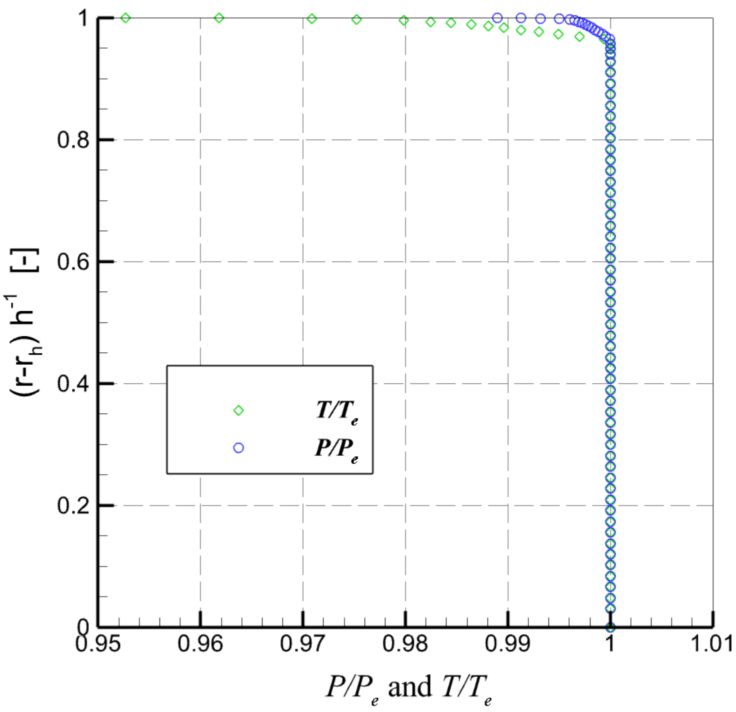

Figure 4-12: Inlet boundary profiles of pressure ratio and of temperature ratio across the Aachen Turbine stage full radial height.

4.5.1 Grid Convergence Index and convergence criteria

To investigate the influence of the spatial discretization on the flow predictions, a mesh convergence study is carried out using Richardson's extrapolation that is generalized by Roache (1994). In this work, three meshes are used with a constant refinement ratio $r = 2$. These are a coarse mesh of 1.75 M nodes (mesh 1), a mesh of intermediate spatial refinement of 3.5M nodes (mesh 2), and a fine mesh of 7 M nodes (mesh 3). The grid convergence index (GCI) identifies to what extent the flow prediction approaches its asymptotic value and therefore gives an assessment of the appropriateness of the spatial resolution level. In the present work, the GCI is based on the yaw angle predictions and the GCI is calculated according to Wilcox (2006b). The average yaw angle of the three meshes respectively are 72.3°, 71.6° and 71.3°. The GCI computed with the coarse mesh and the intermediate mesh is 0.916. This is higher than the GCI computed with the intermediate and the fine meshes of 0.394. This indicates a reduction in the mesh dependence of the numerical simulation when the intermediate and the fine meshes are used. The difference between the yaw angles α_{2_i} predicted using the i^{th} mesh and the one obtained from Richardson's extrapolation ${\alpha_2}_R$ is used to define the relative error as $\epsilon_i = {\alpha_2}_i {\alpha_2^{-1}}_R - 1$.

Figure 4-13 shows the relative error based on Richardson's extrapolation with the normalized mesh spacing. As the mesh is refined, the difference between the simulation and the extrapolated value becomes small. In fact, the relative errors are $\epsilon_1 = 1.72\%$, $\epsilon_2 = 0.73\%$, and $\epsilon_3 = 0.31\%$. As the difference in the relative errors between the intermediate mesh and the fine mesh is below 1%, the mesh of intermediate spatial resolution is selected for the current study.

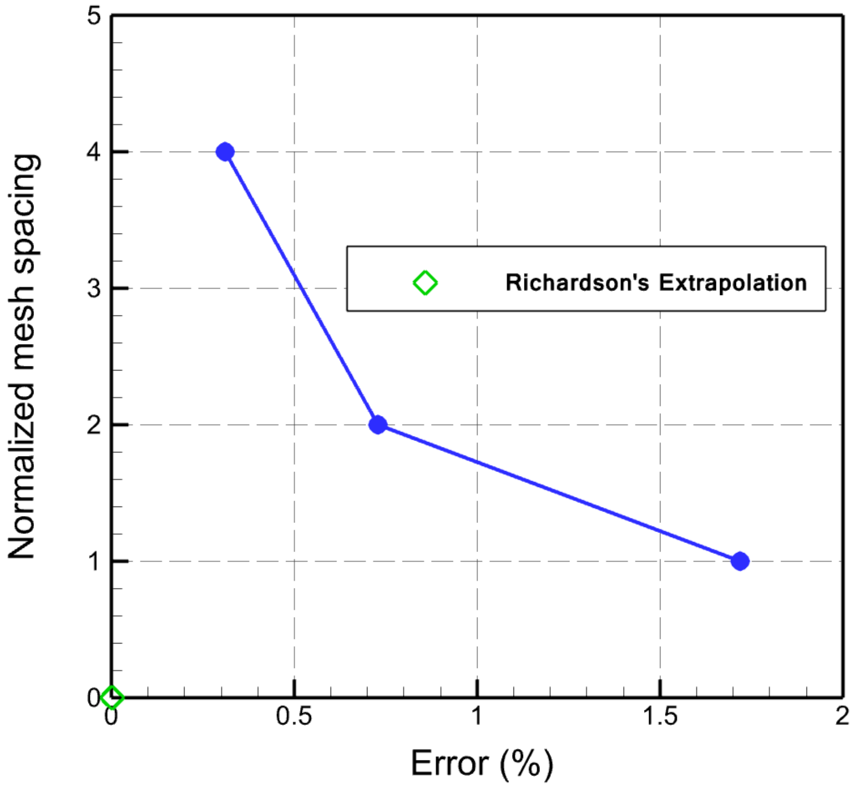

Figure 4-13: Percentage error for a set of three meshes based on Richardson's extrapolation.

A good solution residuals history should be between 10^{-4} and 10^{-6} for well-behaved steady-state simulations (Praisner et al., 2013). However, the flow field within the turbine is subjected to several sources of unsteadiness, such as the interaction of the boundary layer with the main flow and the interaction of the tip leakage flow with the main rotor passage flow. These sources can cause problems to obtain converged steady-state solution. The numerical solution was iterated by OpenFOAM 3.2 Extend and

ANSYS Fluent 18 to convergence, as assessed by the reduction in the residuals by 10^{-5} with respect to their values at the start of the computation. The converged solution typically took 10 hours of computer wall time on 30 HPC cores.

4.6 Averaging of flow properties

To enable the direct comparison between experimental measurements and CFD predictions, the flow state is extracted from the CFD predictions at the same locations as in the experiment shown in Section 4.2. Two approaches are used to calculate and check the pitch-averaged flow properties of 17 circumferential measurement lines. The first approach uses the OpenFOAM 3.2 post processing tools and graphical rendering by Tecplot 2017. The 3D geometry and the flow solution, defined in Cartesian coordinates, are projected in cylindrical coordinates using the Sample dictionary of OpenFOAM 3.2. The sample dictionary allows exporting the 17 radial lines at the required axial measurements plane, such as measurement plane 1 which is located at 8.8 mm behind the stator 1 trailing edge. Similarly, in ANSYS Fluent 18, the flow field properties are obtained using the Line/Rake tool. This requires defining the start and the end of the rake and the number of points located on it.

The second approach uses user-defined functions in Tecplot 2017 to extract the flow quantities and provide a 2-D profile as an average of a fluid property. Figure 4-14 shows an example of the average outlet flow angle, α_1 extracted at measurement plane 1. The example includes using a grid located at 8.8 mm downstream stator 1 with I and J ranges. The I range starts from 246 mm radius to 299 mm radius with a step of 1 mm. The J range covers a one passage pitch which is divided into 17 radial lines. Figure 4-14 shows that the two approaches provide essentially the same pitch averaged results.

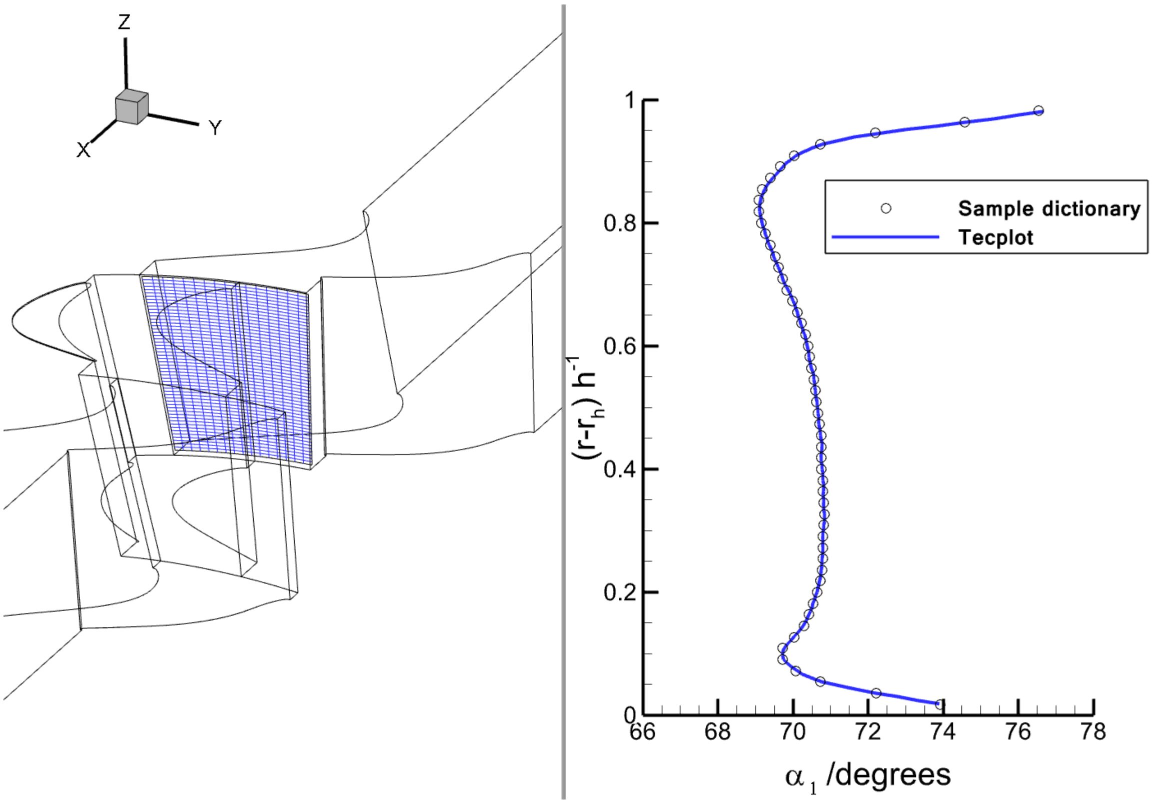

Figure 4-14: A grid used in Tecplot to generate the pitch-averaged flow angle 8.8 mm downstream of stator 1.

Chapter 5

Optimization of the Casing Shape

5.1 Introduction

Computer-based optimization is an established practice in industrial design to maximise the benefits of a newly introduced design feature. The computer-based optimization of the aerodynamics of axial turbines is typically performed with the objective of maximising the stage isentropic efficiency. This work uses the stage total pressure loss, which is closely related to the stage isentropic efficiency, as the objective function to enhance the performance of a representative axial turbine by optimizing the shape of its casing. Computer-based optimization samples the design space by performing a number of physical or numerical experiments in which the objective function, in this case the stage isentropic efficiency, is evaluated. In this application, numerical experiments are performed of the flow through the 1.5 stage Aachen Turbine of Chapter 4 with different realizations of the non-axisymmetric casings of Chapter 3. Since each computational fluid dynamic numerical test is computationally expensive, a surrogate-based model approach is taken. This chapter starts by outlining the conventional design optimization process that is typically used in industry and the specific surrogate-based optimization process that is used in this work. This chapter then presents the numerical optimization procedure of the turbine casing design and how to perform its sensitivity analysis through the quality indicator technique. This is contextualized in the optimization process of the casing design parameter pair (w_{te}, μ) defined in Chapter 3. The optimization design process is implemented using the Automated Process and Optimization Workbench (APOW) software. This computer software is an object-oriented program licensed by GE Power, who acquired Alstom UK Ltd in 2014.

5.2 Conventional optimization process

A design optimization problem is defined as a problem in which design variables need to be determined to achieve the best performance under given constraints. Thus, optimization methods are increasingly applied in industry, since they can provide engineers with cheap, flexible, and automatic means to determine the optimised solution to their design problems before the design is frozen.

The general process of engineering design with optimization is given in Figure 5-1, from Pahl and Beitz (2013). This design process consists of three main steps. The first step is to create an optimization model in a specific mathematical formation, which is also known as a constrained parametric model. This step is the most important one in an optimization design process, as in this step several decisions are to be made, such as the selection of the design variables, of the design objectives, and of the design constraints. The second step is solving the optimization problem. Different methods can be used in this step, such as analytical methods, numerical methods, and graphical methods. The last step is the *a posteriori* analysis of the optimal solution. Several questions about the optimality, feasibility, sensitivity, and the improvement margin may need to be answered in this step.

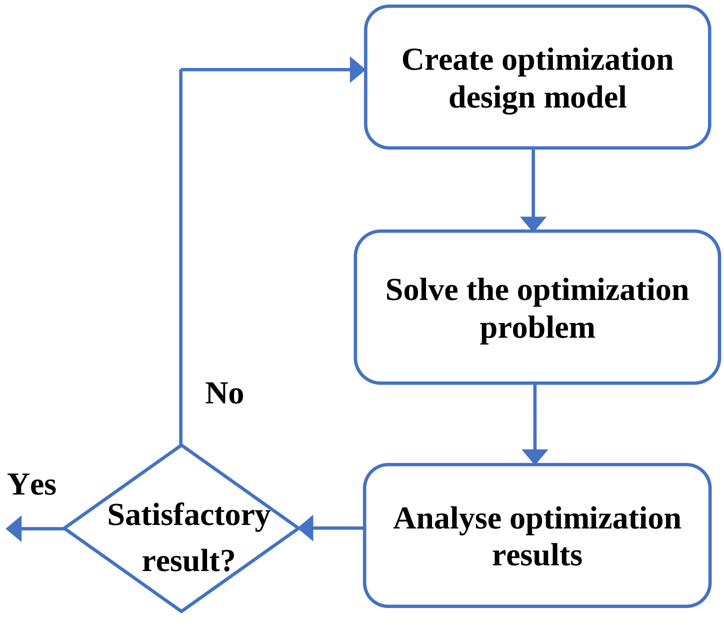

Figure 5-1: The conventional process of optimization in engineering design, adapted from Pahl and Beitz (2013).

As shown in the Figure 5-1, the optimization process is a sequential process with an outer iterative loop. If the design solution is not satisfactory, the designer modifies the optimization model in the first step and repeats the optimization procedure until a satisfactory design is achieved.

In general, optimization is a highly iterative design process requiring many analyses of the model under consideration. In engineering, the main goal of the design process is to create a cost-effective solution that is fit for purpose. Cost is typically a significant driver in the optimization design process. A designer may wish to adopt a thorough optimization method, seeking the best combination of the design variables, but such approach may be unaffordable. For instance, to fully explore the parameter space of 3 discrete variables with 3 levels per variable requires 33 tests. With increasing settings per variable or with more variables, this approach soon becomes intractable. To overcome this problem, cheaper approximating models, referred to as “surrogate models”, are often used. In the next section, the surrogate-based optimization process is introduced, as it can reduce the cost of the design process compared to a more conventional optimization process.

5.3 Surrogate-based optimization process

The increased accuracy of modern Computational Fluid Dynamics (CFD) simulations, both for compressible and incompressible fluids, enable aerospace engineers nowadays to evaluate the performance of a specific design through virtual prototyping (Forrester and Keane, 2009). This has enabled the progressive reduction of costly experimental tests, such as those carried out in wind tunnels. Although the fidelity of computer models has increased, the computing cost has also increased and this has become the main limiting factor in the design optimization process. This has prompted the replacement of expensive computer simulations with alternative cheaper surrogate models (Søndergaard et al., 2003). Surrogate models approximate key design performance metrics that are otherwise computed from more expensive simulations. A surrogate-based analysis and optimization approach was applied to the design of turbine blade profiles by researchers including Madavan et al. (1999), Rai et al. (2000) and Shyy et al. (2001). The key stages in the surrogate-based modelling approach are shown in Figure 5-2, adapted from Queipo et al. (2005). These are the Design of Experiment (DOE), the construction of the surrogate model based on CFD simulations performed at selected locations of the design space, and the model validation.

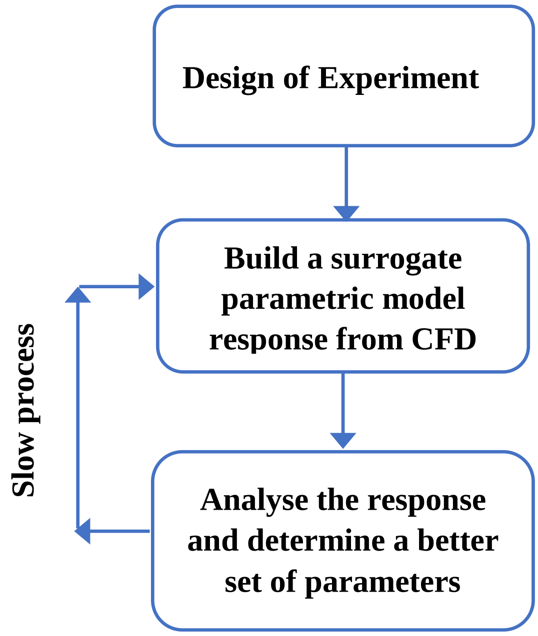

Figure 5-2: Key steps of surrogate-based optimization, adapted from Queipo et al. (2005).

The first strategic decision that has to be made is to define a set of parameters for the approximation method by the design of the experiment (DOE) as shown in Figure 5-2. In this step, a set of sampling points is generated to probe the design space using a specific statistical technique available in DOE. The key challenge is to define the number of sampling points and the way these are distributed so that these may provide a good statistical coverage of the design space. A more extended discussion on the Design of Experiment is presented in Section 5.3.1. The second step is to construct a surrogate model based on a computationally more expensive simulation that is performed at each of the sampling points defined in the DOE. The last step is to analyse a surrogate model response. In this step, four questions are of interest:

- Was the surrogate model appropriately selected?
- Were the design parameters identified in the DOE appropriate?
- How should the surrogate model response be tested for reliability?
- To what extent the model meets the purpose of predicting the performance of the design with acceptable engineering accuracy at an affordable cost?

Figure 5-3 is an extension of the flowchart of Figure 5-2 that is used to answer these questions. In this figure, two activities have been added. The first activity is to create a parametric model using a specific mathematical formulation. The second activity is to sample the parametric model response by CFD simulation. Following the building of a surrogate model from these CFD predictions, a fast inner loop is used. This involves evaluating iteratively the surrogate model response for a set of parameters to identify the parameter values that optimize the response. The set of parameters used in this inner loop is typically a small sub-set of the design parameters defined at the Design of Experiment phase. Once the inner loop identified parameter values that give a response plateau, the inner loop terminates and the surrogate model output is evaluated. The evaluation may lead to either accepting the output or to identifying the requirement for further sampling the parameter space by running further Computational Fluid Dynamic tests. This outer loop is a slower process and it is performed until the response to the four questions in the previous paragraph is satisfactory.

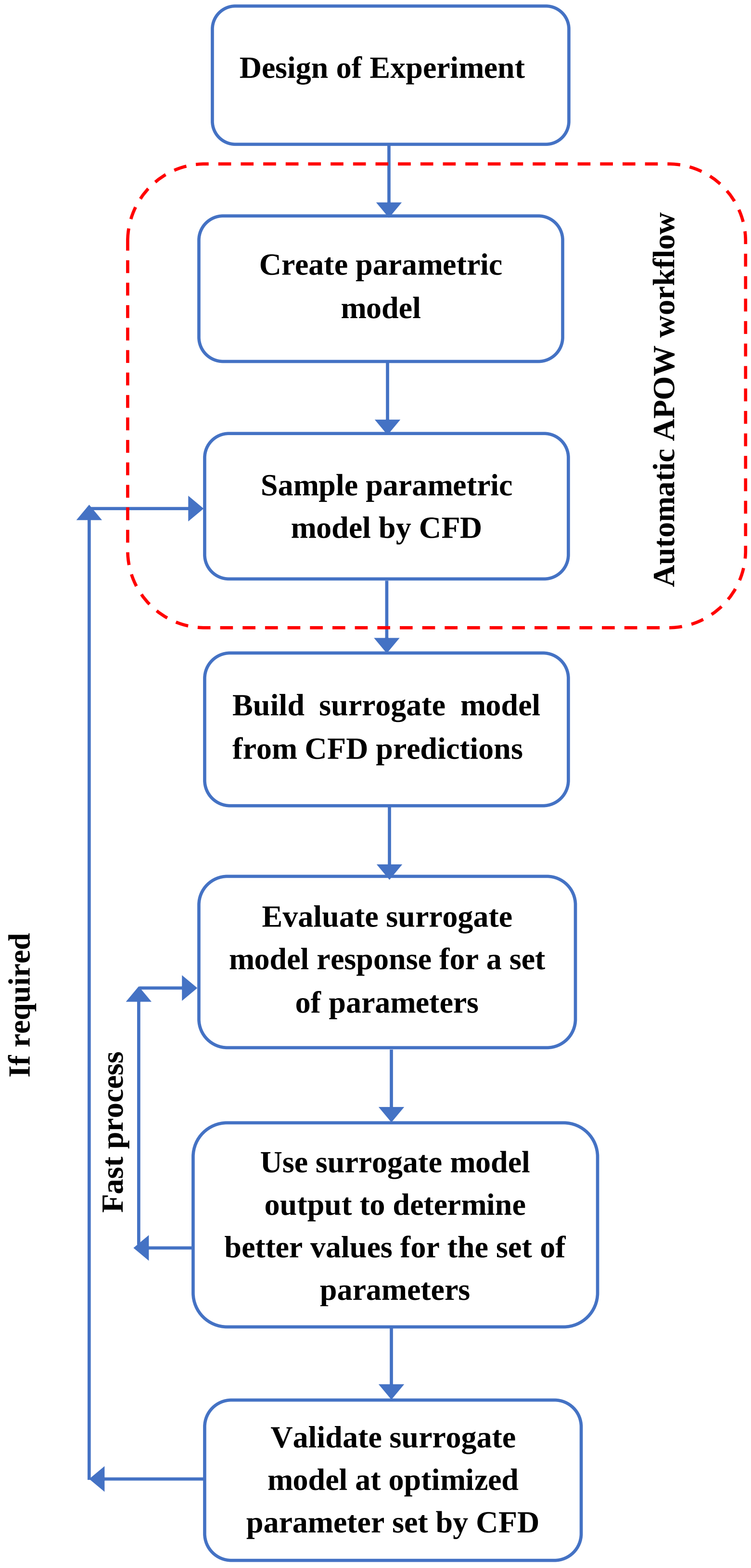

Figure 5-3: Modified surrogate-based optimization flowchart.

5.3.1 Design of experiment (Optimal Latin Hypercube)

Heuristic evolutionary techniques do not provide any basic assumption on the relation between objectives and design variables. A good initial sampling selection, that allows an initial guess on the relations between inputs and outputs, is of great importance for achieving good results and for reducing the optimization effort (Poles et al., 2009). In optimizing a turbine blade, the minimum number of the design samples are usually selected as two to five times the number of design variables (Arabnia, 2012). In this task, the number of samples is severely limited by the computational cost of each sample.

The design of experiment (DOE) is a sampling plan in the design variable space aimed at gaining the most possible knowledge within a given dataset. Complex and costly experimental situations can be mitigated by using an appropriate design of experiment (Eriksson et al., 2008). All factors (design variables) are considered in a minimal number of experiments that are verified with recognized statistical techniques. Five different statistical techniques of DOE are available in APOW. A popular selection for generating a deterministic computer experiment is the Latin Hypercube (McKay et al., 1979). The drawback of this design technique is that there is no guarantee of having a good space filling. This drawback is mitigated by the Optimal Latin Hypercube design of experiment. Therefore, the Optimal Latin Hypercube design of experiment is used in the present work, based upon which the surrogate model is built. This design of experiment can cover the design space more evenly and generate more evenly distributed points than other DOE techniques (Zhao and Cui, 2008). It is a modified statistical method of the Latin Hypercube DOE in which each factor is optimised rather than using a random uniform division for all factors. The factor levels of each factor are then combined to generate an initial random Latin Hypercube Design matrix. An algorithm for generating such design technique can be found in Morris and Mitchell (1995). Morris and Mitchell (1995) report a comparison of this technique with the standard Latin Hypercube DOE using two independent variables with 16 sample points and show the performance advantage of the Optimal Latin Hypercube DOE.

5.3.2 Optimization cost functions

There are many options for the selection of the objective function to be used in the optimization process, which aims to meet some pre-defined design specifications. Panchal et al. (2011) optimised two endwall geometries of an axial turbine cascade. They tested the total pressure loss coefficient and the secondary kinetic energy (SKE) coefficient as the objective functions. They recommend using the total pressure loss coefficient as the objective function, as the SKE reduction was less indicative of the performance of both optimised endwalls.

Different objective functions have been used in the literature for turbine design optimization, including the secondary turbulent kinetic energy, the total pressure loss, the stage efficiency, and the vorticity magnitude. This work follows the recommendation by Panchal et al. (2011) and uses the total pressure loss coefficient to drive the optimization of the casing. The total pressure loss across the upstream half-stage alters the flow exiting it. The change in the flow exiting the upstream stator passage affects the downstream rotor performance. This change in turns typically alters the stage efficiency. Therefore, the total pressure loss coefficient C_{Pt} is used to drive the optimization of the casing by defining two objective functions. The first objective function is the stator row total pressure loss coefficient

$$C_{Pts} = \frac{\overline{\overline{P_{to}}} - \overline{\overline{P_{t1}}}}{\overline{\overline{P_{t1}}} - \overline{\overline{P_{t}}}} \tag{5.1}$$

and the second objective function is the stage total pressure loss coefficient

$$C_{Ptr} = \frac{\overline{\overline{P_{to}}} - \overline{\overline{P_{t2}}}}{\overline{\overline{P_{t2}}} - \overline{\overline{P_{2}}}} \tag{5.2}$$

where subscript 0 denotes the stator inlet plane, subscript 1 denotes the stator exit plane, subscript 2 denotes the rotor exit plane, and (=) denotes a pitchwise and radially averaged quantity.

The objective is to minimise both total pressure loss coefficients. This choice gives quantitative discriminants for comparing between two casing walls based on C_{Pts} and C_{Ptr}. These are the bases for the grooved casing design and optimization process.

5.3.3 Evaluation of the cost function by CFD

The cost functions of Equations (1) and (2) are evaluated at specific combinations of the design parameters, as defined by the Optimal Latin Hypercube technique of Section 6.4.2, by performing numerical experiments, by CFD.

The parametrized casing groove geometry of Chapter 3 is used and the constraints on the parameter ranges are defined. Three main variables are used for the optimization process: the maximum groove depth location along the groove path $\mu\ (x, \theta_g)$, the groove width at the blade leading edge $w_{le}(x,\ \theta_g)$, and the groove width at the blade trailing edge $w_{te}(x,\ \theta_g)$. The groove width at the blade leading edge w_{le} was found to have a small effect on the total pressure loss as shown in Chapter 6, therefore, this parameter is optimized segregated and last.

For a given combination of (μ, w_{le}, w_{te}) defined by the Optimal Latin Hypercube DOE, the corresponding contoured casing surface is generated in MATLAB, as described in Section 5.5. This surface is imported as NURBS in ICEM CFD to define the computational domain, as described in Section 5.5. The computational domain is discretized in ICEM CFD and the resulting unstructured mesh is imported in OpenFOAM, as detailed in Section 5.5. The boundary conditions of Section 4.5 are applied as for the axisymmetric casing geometry and the numerical solution is iterated by OpenFOAM convergence. Equations (5.1) and (5.2) are then evaluated, based on the CFD flow solution, and the results are associated to the given combination of (μ, w_{le}, w_{te}). Specifically, the values returned by equations (5.1) and (5.2) are the values of the cost function sampled at (μ, w_{le}, w_{te}), evaluated by CFD.

5.3.4 Reduced order models (Surrogate models)

The use of surrogate models to perform an optimization process is growing strongly in industry and the most commonly used surrogate models are based either on the Latin Hypercube or on the Optimal Latin Hypercube. Using a surrogate model with an effective interpolation and sampling method reduces the number of CFD simulations that are required to construct a database to a specific confidence level. The surrogate models are constructed using data drawn from high-fidelity models and provide fast approximations of the objective functions within limits at new design points (Queipo et al., 2005). An overview of the surrogate-based analysis and of surrogate models is presented in Queipo et al. (2005). Details on the surrogate modelling techniques available in APOW are given in Alstom (2014). In this work, Kriging modelling (KRG) is used to construct the response surface. The Kriging interpolation technique, or Gaussian process regression, is often used for predicting the value of a real function at some input locations given a limited number of observations of this function (Rullière et al., 2016). The accuracy of the Kriging model has been improved over the last decades so that Kriging is now regarded by some authors as being sufficiently accurate for most applications (Zhang et al., 2014). There is a growing body of literature that documents the use of Kriging for generating reduced-order models for optimizing the design of axial turbines. Alternative approaches include genetic algorithms and adjoint methods. In this work, Kriging was used as it can give a good compromise between the computational cost and the prediction accuracy. It allows to properly capture the complexity of a response surface featuring sharp curvature changes, even in presence of highly irregular distributions of interpolation sampling points (Persico, 2017).

5.3.5 Location of the cost function minimum

The optimization analysis of the response function was performed on the Kriging surrogate model. Provided the Kriging response function is a parametric surface of type $S(u, v)$, continuous to at least first order, then the surface minimum, which represents the lowest total pressure loss coefficient, is identified by the application of a simple steepest descent approach. As the response function parametric surfaces obtained for the casing optimization were of this type, as indicated in Section 6.4.2, this simple approach to locating the surface minimum was appropriate.

Had the response function been discontinuous, alternative techniques for locating the cost function minimum could have been used, such as the Simplex method by Nelder and Mead (1965). This alternative method does not require the response function gradient to be computable (i.e. the response function to be differentiable to first order) as it only requires the evaluation of the function itself for its implementation.

The percentage difference ϵ between the optimal total stage pressure loss coefficient predicted from Kriging, $C_{Ptr-Kriging}$, and from CFD, $C_{Ptr-CFD}$, was calculated as

$$\epsilon = \left(\frac{C_{Ptr-Kriging} - C_{Ptr-CFD}}{C_{Ptr-CFD}}\right) \times 100\% \qquad (5.3)$$

to validate the value of total stage pressure loss coefficient from the Kriging model predicted at the cost function minimum. Here $C_{Ptr-CFD}$ is the stage total pressure loss coefficient determined from an additional CFD computation at the most favourable combination of contoured casing design parameters associated to the cost function minimum. This step is the last step of the flowchart in Figure 5-3, which was used to check whether the Kriging approximation was satisfactory.

5.4 Sensitivity analysis performed by sampling the design space

In the case of a black box computer-based optimization, where the system response function is not known, no proactive sampling strategy can be relied upon to optimize the sampling of the design space. Therefore, it is essential to examine the sampling distribution in the design space *a posteriori* and particularly around any predicted system response optimum (in this case, the predicted pressure loss coefficient minimum). This may lead to adding more samples in the neighbourhood of the predicted system response optimum. The distribution of these additional samples in the design space is therefore informed from results of the previous sample set. This process is commonly known as adaptive sampling. Adaptive sampling is an area of active and sustained research, as documented by the contributions from Sasena et al. (2002), Kulkarni (2006) and Mackman et al. (2013). Different implementations of adaptive sampling is also used in combination with Kriging models to perform an efficient global optimization in Sasena (2002) and in Chen et al. (2014).

The *a posteriori* analysis of the sampling strategy is typically cast in the context of performing a sensitivity analysis of the Kriging model on the sample set. In this work, a sensitivity analysis is performed based on the stage total pressure loss coefficients results. An initial set of 10 points is used to sample the design space using the Optimal Latin Hypercube method as shown in Figure 6-13, Section 6.4.2, Chapter 6. The parameter space constraints, that is the maximum and minimum values in the casing parameters w_{te} and μ, are defined based on previous results obtained from a simple trial and error approach reported in Chapter 6. The workflow of Figure 5-4 is then executed up to the activity "Validate surrogate model at optimized parameter set by CFD". From Figure 6-17, there are only two sampling points in the region around the optimal design point (p^{opt}), which is identified using (C_{Ptr}). This is not conducive to obtaining accurate predictions from the Kriging model in this region. To examine and enhance the accuracy of the Kriging model, a local adaptive sample of 10 points is added to the initial set of 10 points used in the 'Sample parametric model by CFD' activity of Section 5.3.3. The adaptive sample set is also generated using the Optimal Latin Hypercube method and therefore it is not an arbitrary sample. The extent of the re-sampled region was constrained to include (to be tangent to) the 10% stage total pressure loss contour shown in Figure 6-15. This smaller sample space region includes the optimal design point (p^{opt}) from the initial set.

The reduction in the stator row total pressure loss coefficient ΔC_{Pts} is calculated as:

$$\Delta C_{Pts} = \left(\frac{C_{Pts-optimised} - C_{Pts-base}}{C_{Pts-base}}\right) \times 100\% \qquad (5.4)$$

where $C_{Pts-base}$ is the stator row total pressure loss coefficient determined from the CFD predictions with an axisymmetric casing, which is the reference geometry of the Aachen Turbine test case, and $C_{Pts-optimised}$ is the stator row total pressure loss coefficient interpolated by the Kriging model at the most favourable combination of contoured casing design parameters.

Similarly, the reduction in the stage total pressure loss coefficient ΔC_{Ptr} is defined as:

$$\Delta C_{Ptr} = \left(\frac{C_{Ptr-optimised} - C_{Ptr-base}}{C_{Ptr-base}}\right) \times 100\% \qquad (5.5)$$

where $C_{Ptr-base}$ and $C_{Ptr-optimised}$ are the stage total pressure loss coefficients corresponding to the stator row total pressure loss coefficients $C_{Pts-base}$ and $C_{Pts-optimised}$.

Equation (5.5) is evaluated for the initial sample set (10 points), which gives ΔC_{Ptr-10}, and then for the initial and adaptive sample set (20 points), which gives ΔC_{Ptr-20}. The improvement in the stage total pressure loss reduction (δC_{Ptr}) identified by the application of the adaptive sampling is defined as

$$\delta C_{Ptr} = \left(\frac{\Delta C_{Ptr-20} - \Delta C_{Ptr-10}}{\Delta C_{Ptr-10}}\right) \times 100\% \qquad (5.6)$$

A sanity check was performed on the $C_{Ptr-optimised}$ values used in Equations 5.5 by computing ϵ using Equation 5.3. ϵ_1 was computed from $C_{Ptr-optimised}$ as determined from the initial sample of 10 points and ϵ_2 from $C_{Ptr-optimised}$ as determined from the sample of 20 points. ϵ_1 and ϵ_2 were found to be significantly smaller than the performance improvement ΔC_{Ptr} obtained through the optimization process. The values of ϵ_1 and ϵ_2 are reported in Table 6-3.

The result from the optimization procedure for the two different parametric design techniques presented in Chapter 3 is shown and discussed in the Chapter 6. In addition, the result of the sensitivity analysis based on the model quality indicator and on the equations (5.3)-(5.6) are shown and discussed in Chapter 6.

5.5 Implementation of the optimization process

The implementation of the optimization method used in this work is based on the third-party software APOW. APOW is a Java-based software that creates and executes a design and optimisation loop to accomplish an explicit design objective defined by the user. The APOW has many functionalities, ranging from simple processes, such as creating a directory, reading and copying variables, to more complex functionalities, such as defining an Optimal Latin Hypercube sample. The casing design workflow implemented in APOW is shown in Figure 5-4. This is an open loop design workflow in which a black box type optimization approach is implemented. In this context, the black box approach means that no *a priori* topology of the system response is assumed.

The automatic workflow of Figure 5-4 is executed in batch mode for different values of $w(x,\ \theta_g)$ and $\mu\ (x, \theta_g)$ using APOW. The APOW Design of Experiments (DOE) is used to populate the design space, based on the Optimal Latin Hypercube design technique. The optimization analysis of the DOE is performed on a surrogate model. For this purpose, Kriging is selected as the surrogate model type to use.

Different realizations of the turbine passage with a non-axisymmetric casing are then produced based on the values of the design parameters that populate the design space, from the Design of Experiments. As shown in Figure 5-4, this is obtained by first copying a Matlab code file and creating a Linux script for running the Matlab code. The Matlab code evaluates the surface definition function $S(u,v)$ and its dependencies defined in Chapter 3, starting from the values of the design parameters. APOW runs the Linux script which generates, via Matlab, the casing design surfaces as Non-Uniform Rational B-splines (NURBS) and exports them as IGES files. This process gives the user the ability to reduce the number of samples in the Design of Experiment by eliminating combinations of the parameters that are unlikely to provide a performing casing design, based, for instance, on previous studies. The next step is the APOW writer process. Within this step, APOW copies the computational domain of the one and half stage turbine with an axisymmetric casing into the APOW working directory TempDir. Then, APOW creates a .rpl file which includes the instructions for meshing the computational domain in ICEM CFD using the reply facility of ICEM CFD. The next step is to execute ICEM CFD to create the structured mesh and to save it as an ANSYS Fluent .msh file inside the working directory TempDir. This step involves reading the contoured casing surface as a set of three NURBS in ICEM CFD, to delimit the top of the computational domain. The computational domain is then discretized in ICEM CFD by maintaining similar meshing parameters as for the validated 1.5 stage turbine model of Section 4.3.2, to obtain the same mesh quality as for this validation test case. The structured mesh is then converted into an unstructured mesh, as this is the only supported output format accessible through the ANSYS Fluent academic license. The .msh file output is now ready for use by a compatible flow solver.

The next step is to solve the flow field using OpenFOAM to predict the aerodynamic pressure losses. The same boundary conditions are applied as for the validation test case in Section 4.5 and the numerical solution is iterated by OpenFOAM to satisfy the same convergence criteria. This step includes five main processes in the OpenFOAM execution script:

1. Read the unstructured mesh file .msh in OpenFOAM.
2. Check the mesh quality.
3. Define the periodic boundaries and the mixing planes of the computational domain.
4. Divide the computational domain by domain decomposition among serval processors.
5. Run the OpenFOAM flow solver.

The OpenFOAM commands and details on the above steps are reported in Section 4.4. Finally, the stator row total pressure loss coefficients and the stage total pressure loss coefficients are collected as an output file to generate a database which contains the design variables and their corresponding aerodynamic performance. From this database, a Kriging surrogate model is built.

The APOW graphic user interface (GUI) shows the above processes by an activity on the arrow diagram. As APOW progresses through the workflow, the completion status flag of each activity is progressively changed from pending to completed, in real time. Should any activity fail to complete, APOW runs some basic diagnostics and displays on the GUI the nature of the error and in which activity the error has taken place, using user-friendly symbols. This enables troubleshooting the workflow until it runs smoothly without further user intervention.

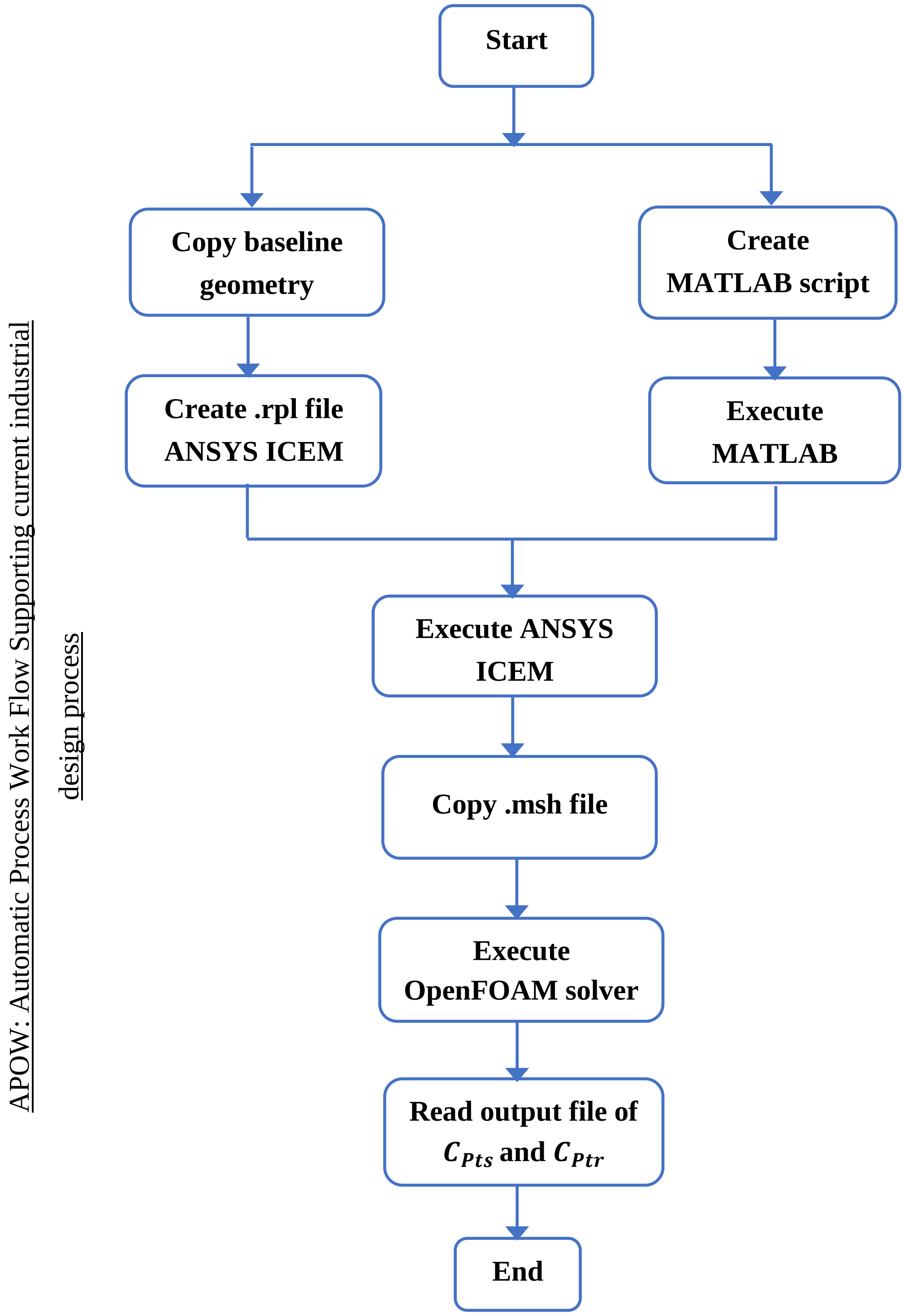

Figure 5-4: Activity on the arrow workflow implemented in APOW for automating the design and optimization of an axial turbine 1.5 stage with a parametric non-axisymmetric casing.

Chapter 6

Results and Discussion

6.1 Introduction

This chapter reports the application of contouring to the casing of the Aachen Turbine upstream stator blade row.

The first part of this chapter presents a CFD model of the Aachen Turbine upstream stator blade row. This model, built in ANSYS Fluent and OpenFOAM 3.2 Extend, is validated and used to perform a feasibility study of a guide groove treatment for the upstream stator casing. The CFD model is then extended to simulate the full one and half stage Aachen Turbine, in OpenFOAM 3.2 Extend. The validation of the extended model is presented, by comparing the outflow from the stator 1, the rotor, and the stator 2, between experiment and CFD. This model is then used to explore the effects of the guide groove treatment on the full one and half stage Aachen Turbine. The performance of four different guide grooves is evaluated by CFD at the Aachen Turbine experimental test conditions, the best configuration is selected, and then this is tested at off design conditions.

Based on the groove geometry parameter space identified in the feasibility study, a computer-based optimization of the contoured casing is performed. For comparison purposes, the same optimization technique is applied to design a contoured casing by the reference diffusion design method reported in Chapter 3. For both designs, the optimization and its sensitivity analysis are implemented using the Automated Process and Optimization Workbench (APOW).

This chapter concludes with a flow analysis that compares the optimized guide groove design applied to the turbine stator casing with the optimized diffusion design.

6.2 CFD model of the Aachen Turbine upstream stator blade row

The upstream stator row of the Aachen Turbine is modelled by CFD. This geometry requires less computational resources than a full stage, it does not use rotating and non-rotating frames of reference and does not require interfacing these domains by mixing planes. The intent is to test whether contouring the casing wall reduces the loss across the stator. This is shown in the literature to be almost a necessary condition for reducing the loss across the full stage.

The upstream stator passage geometry, defined in Chapter 3, is imported in ICEM CFD, where the computational domain is discretized as detailed in Section 4.3.1. An average near-wall resolution of $y^+ \simeq 1$ is achieved. The computational mesh is ported both in ANSYS Fluent 18 and in OpenFOAM 3.2 Extend, where the boundary conditions of Section 4.5 are applied. The flow is modelled as fully turbulent and the RANS $k - \omega$ turbulence model is used in both solvers. This turbulence model was selected based on the work by Wang et al. (2014) who compared different turbulence models and concluded that the $k - \omega$ model better resolves the secondary flow features through a turbine cascade at a similar Reynolds number. RANS flow predictions are obtained to the convergence criteria detailed in Section 4.5.1. The flow predictions are post-processed by Tecplot 2017.

6.2.1 Model validation

A quantitative validation of the baseline flow prediction with an axisymmetric casing cascade passage is sought by comparison against measurements from RWTH Aachen. To enable the direct comparison between experimental measurements and CFD predictions, the flow state is extracted from the CFD predictions at the same locations as in the experiment. These locations are reported in Section 4.2. Figure 6-1 shows the comparison between measured and calculated radial distributions of flow velocities and yaw angle at 8.8 mm behind the stator. These spanwise profiles have been pitch averaged using a simple average as defined in Chapter 4. The agreement between measurements and CFD predictions is good with both ANSYS Fluent and OpenFOAM solvers. The mean absolute error (MAE) and the root mean square error (MRSE) (Hyndman and

Koehler, 2006) are used to quantify the average error in the circumferential velocity profile along the blade height between prediction and experiment.

The MAE is the average of the absolute difference between the CFD predictions and the experimental measurements and it is defined as

$$\text{MAE} = N_{exp}^{-1} \sum_{i}^{N_{exp}} \left| U_{comp,i} - U_{exp,i} \right| \tag{6.1}$$

The RMSE measures the distance between the numerical and the experimental data (Reis, 2013). It is often used as an accuracy assessing tool. The RMSE is defined as

$$\text{RMSE} = \sqrt{N_{exp}^{-1} \sum_{i}^{N_{exp}} \left(U_{comp,i} - U_{exp,i} \right)^2} \tag{6.2}$$

For the OpenFOAM predictions, MAE = 2.14 m/s and MRSE = 3.03 m/s, whereas for the ANSYS Fluent predictions, MAE = 3.26 m/s and MRSE = 3.83 m/s. The error values from the OpenFOAM solver are marginally lower than those from ANSYS Fluent. Whereas in practice these errors are comparable, OpenFOAM was used for further work, as its license is not core count limited.

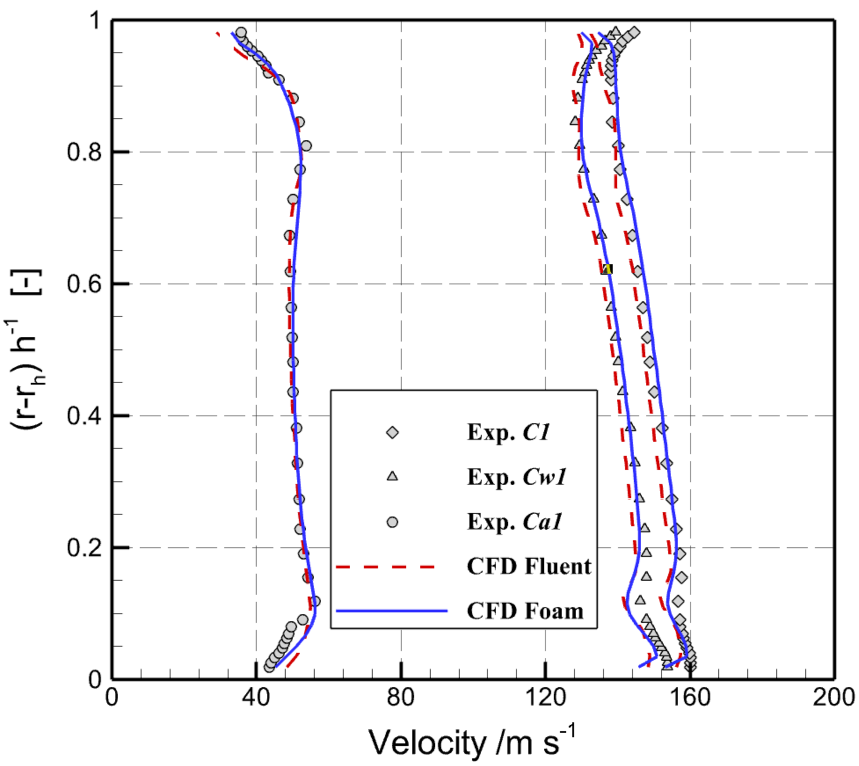

(a)

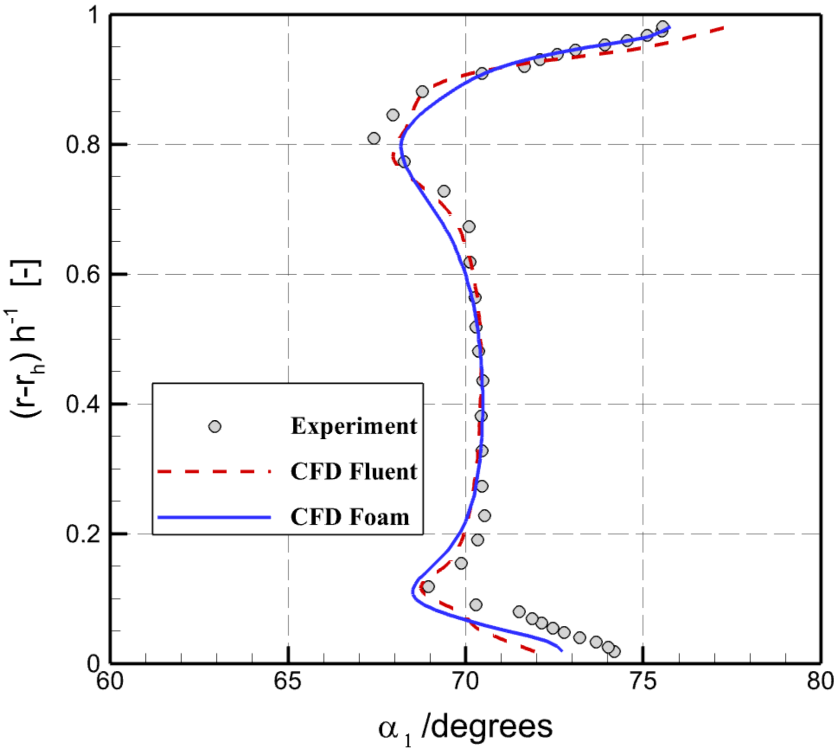

(b)

Figure 6-1: Measured and calculated radial distributions of velocity components and yaw angle at 8.8 mm behind the stator, pitchwise averaged.

It is acknowledged that the total pressure loss is also important for validating the numerical model for both the cascade and the full one and half stage Aachen Turbine. However, the experimental dataset of Walraevens and Gallus (1997) does not include any direct loss measurement. As such, the CFD model is herein validated against measured components of the flow velocity and yaw angles.

Figure 6-2 shows the flow visualization over the axisymmetric casing predicted under the test conditions of Table 4-1and Table 4-3 of Chapter 4 by OpenFOAM 3.2 Extend. Near-surface streamlines are extracted from the steady RANS solution using Tecplot 2017.

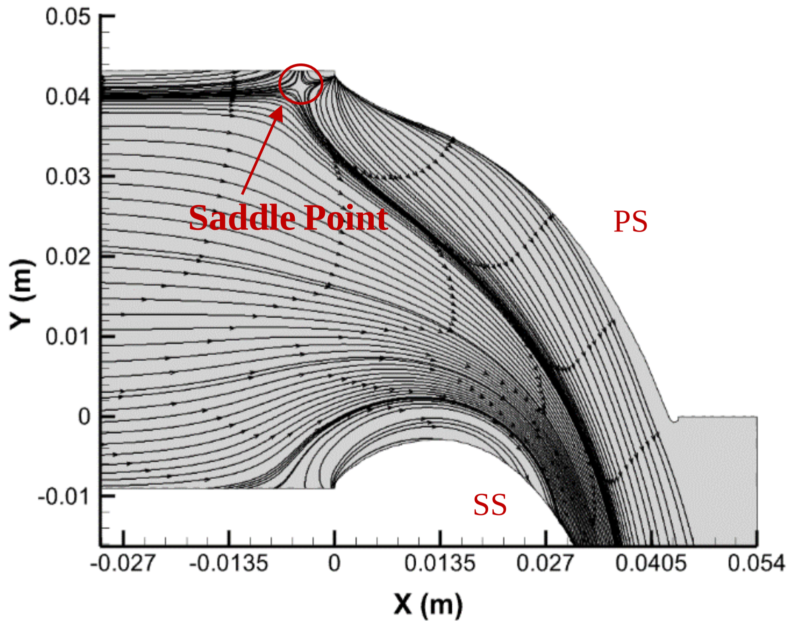

Figure 6-2: Flow visualization over the stator 1 axisymmetric casing showing the separation of the oncoming casing boundary layer (saddle point) by the streamlines.

This visualisation indicates the presence of the flow structures outlined by Langston (2001) that are often observed over turbine casing walls, as reported in the Chapter 2. Specifically, the inflow to the stator cascade blades features a growing boundary layer on the casing wall, along the 143 mm long passage leading edge. The upstream boundary layer bifurcates at the leading edge of the blade, forming a saddle point. The location of this bifurcation is highlighted by the arrow in Figure 6-2. Due to the interaction of the endwall boundary layer and the adverse pressure gradient from the blade potential pressure field, a horseshoe vortex is generated near the junction between the blade leading edge and the endwall.

The horseshoe vortex left and right arms bend downstream into the passage on both pressure and suction sides as shown by ribbons in Figure 6-3. These are shown to visualise both the flow path and the local flow vorticity. The streamlines approach the blade leading edge from the left, as indicated by the white arrow in Figure 6-3 (a). Two streamline rakes are used to visualise the flow path around the blade root, on the suction side and on the pressure side. The rake of streamlines approaching the blade suction side surface, denoted as SS in Figure 6-3 (a), wrap tightly around the blade leading edge, as more clearly shown by the enlargement of Figure 6-3 (b). The three ribbons adjacent to the blade SS appear twisted, whereas the other ribbons further away from the SS surface remain essentially untwisted in Figure 6-3 (b). This indicates the presence of a horseshoe vortex with a suction side branch that is tightly wrapped around the blade and that remains rather compact until about 0.5 axial chords downstream of the blade leading edge, as shown by Figure 6-3 (a).

The rake of streamlines approaching the blade pressure side, shown towards the bottom of Figure 6-3 (a), display a different behaviour. Downstream of the blade leading edge, these streamlines do not follow the pressure side root, but cut across the passage and move towards the blade suction side. As they move towards the blade suction side, Figure 6-3 (a) shows that they start to interact with the rake of streamlines over the suction side.

The twist in the ribbons past the pressure side leading edge, shown in Figure 6-3 (b), indicates that the pressure side arm of the leading edge horseshoe vortex follows these streamlines. By moving across towards the blade suction side, it interacts with the horseshoe vortex suction side branch. This interaction is better appreciated in Figure 6-3 (c) that provides a viewpoint from the passage trailing edge. The ribbons are shown to tangle at about 0.5 axial chords from the blade leading edge and to rise above the casing surface, affecting the main passage flow discharge. This process broadly follows what is depicted in Figure 2-1 of Chapter 2 as the formation of the passage vortex, which is a significant contribution to secondary flow loss in axial turbines.

This flow visualization gives confidence that, from a qualitative viewpoint, the process of interaction of salient near-casing flow structures is resolved in the numerical simulations. This gives some confidence in the use of the numerical model for identifying passive means for suppressing this interaction.

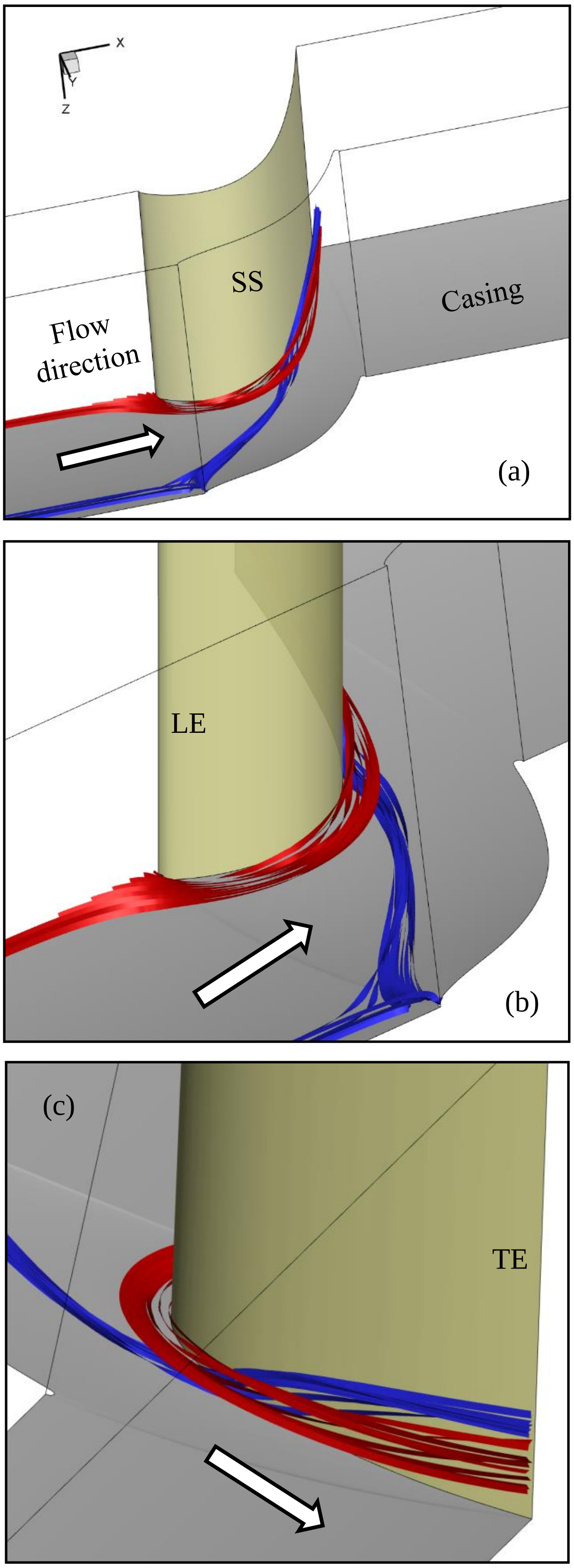

Figure 6-3. Prediction of the flow near the axisymmetric casing visualised by ribbons. (a) blade passage, (b) view from the leading edge, and (c) view from the trailing edge.

6.2.2 Feasibility study of a guide groove treatment for the stator casing

The validated simulations of the RWTH Aachen stator passage flow are used as the baseline for studying the effects of contouring the casing obtained by the new surface definition method described in Section 3.6. This method uses the Beta distribution function to obtain a good surface transition at the outer perimeter of the grooved area. This surface transition is explained in details in Section 3.7. Numerical simulations of the flow through the stator passage with a contoured casing were obtained using the workflow detailed in Section 5.5. A 12 mm constant width groove was applied to the casing. The location of the maximum groove depth was about 50 % of the total groove length. This relatively simple groove geometry was used for testing the feasibility of the guide groove concept, specifically to find out whether the groove had any appreciable effect on the trajectory of the horseshoe vortex and could therefore be further developed as an effective passive flow control device. The predicted flow field was post-processed by Tecplot 2017 to visualise the near-surface flow.

In Figure 6-4, the flow over the contoured turbine casing is visualised by the use of ribbons, which illustrate the vorticity along limit streamlines by the twists in the ribbons. The blade is oriented with the blade height increasing towards the floor of the image, as highlighted by the Cartesian axes inset in Figure 6-4 (a). The ribbons are placed so that they run into the horseshoe vortex that forms near the blade leading edge, marking the path of the horseshoe vortex suction and pressure side branches by their twisted segments. It can be seen that the ribbons approaching the blade towards the pressure side run into the groove and reach the suction side at an axial distance of about x/c = 65% from the blade leading edge, which is farther downstream than in Figure 6-3 (a).

This behaviour is best appreciated in Figure 6-4 (b) where the casing is viewed from the leading edge. The simulation with the grooved casing predicted a reduction in the stator total pressure loss of 2.35% compared with the baseline flow modelled with an axisymmetric casing. This reduction can be attributed to the delayed interaction between the pressure side branch of the horseshoe vortex and the suction side branch, towards the passage trailing edge.

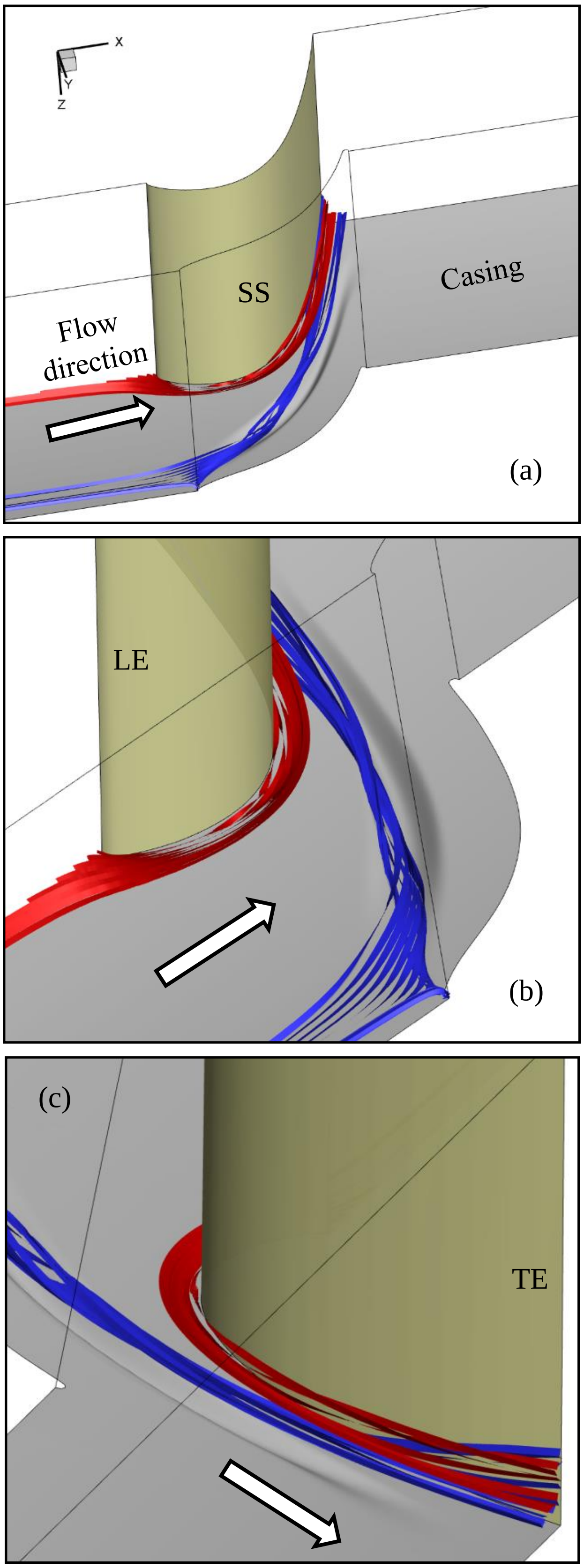

Figure 6-4. Prediction of the flow near the non-axisymmetric casing visualised by ribbons. (a) blade passage, (b) view from the leading edge, and (c) view from the trailing edge.

This interaction is shown more clearly in Figure 6-4 (c), where the casing is viewed from the stator trailing edge plane. The ribbon strands from the blade pressure side move across to the suction side, driven by the pitchwise pressure gradient, crossing the path of the ribbon strands running along the suction side of the pitchwise contiguous blade. This interaction results in some ribbons lifting up towards the centre of the passage, indicating the formation of the passage vortex. Comparing Figure 6-3 (c) and Figure 6-4 (c) shows that a small group of strands appear to lift radially upwards in Figure 6-4 (c), with a second cluster of strands leaving the trailing edge almost parallel to the casing surface. In Figure 6-3 (c), all but two strands lift up from the casing and this is indicative of a larger passage vortex structure in the baseline flow prediction with an axisymmetric casing. In terms of mass flow rate through the cascade, the current design has no significant effect on it as the flow through the throat is subsonic and not choked, so the mass flow rate is not restricted.

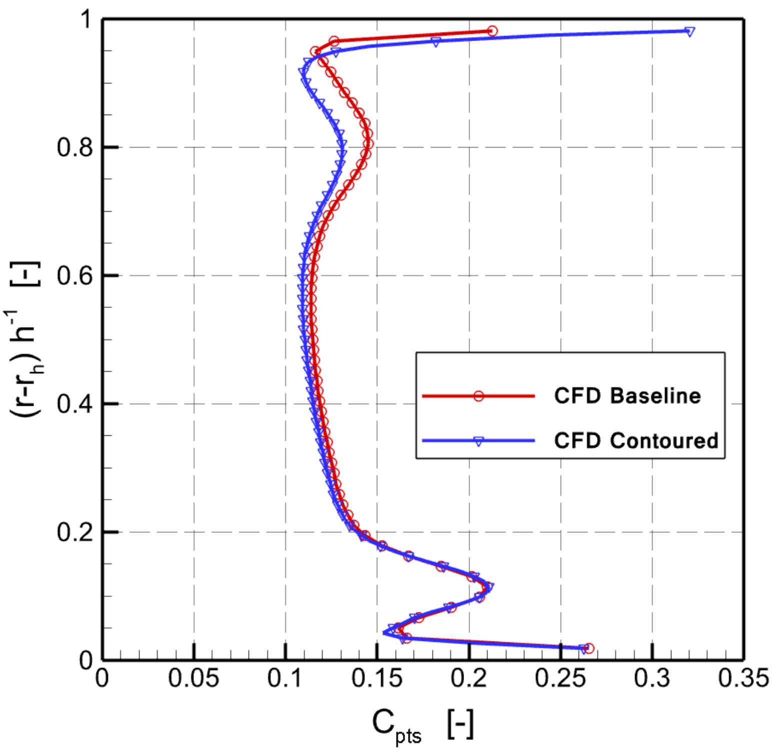

Figure 6-5. Predicted pitch-averaged total pressure loss coefficient along the normalized span at 8.8 mm behind the first stator.

To clarify the outcome of the flow change introduced by the contoured casing, the radial distribution of the pitch-averaged total pressure loss coefficient is determined from the numerical simulations, on the axial plane 8.8 mm behind the upstream stator row. Figure 6-5 indicates that introducing the contoured casing increases the pitch-averaged total pressure loss coefficient very close to the casing, above 95% blade span, whereas it reduces the loss coefficient over the remainder of the blade span. It is observed that this benefit extends down to about 20% blade span, which is relatively far away from the contoured wall. The larger span over which the total pressure loss coefficient reduces out-weighs the near-casing increase, resulting in a net reduction in the total passage pressure loss coefficient of 2.35%.

These predictions have provided evidence that the design approach by the current study works satisfactorily for a turbine stator casing under set point conditions. By adding the groove, the delay in the interaction between the two branches of the horseshoe vortex appears to reduce the passage vortex size and hence the extent of the main passage blockage from this secondary flow feature.

This positive outcome motivated extending the CFD investigation to studying the impact of the new guide groove casing design on a full turbine stage and on the stage outflow to the subsequent blade row. The next section presents the findings from this further work.

6.3 CFD model of the full one-and-half stage Aachen Turbine

6.3.1 Model validation

A RANS model of the one and half stage Aachen Turbine with an axisymmetric casing was built to be used as the baseline for evaluating the effect of contouring the casing. The RANS model used the Aachen Turbine geometry of Chapter 4. One blade passage was modelled by the computational domain of Figure 4-5. The model featured pitchwise periodic boundary conditions and mixing planes at the stator-rotor interfaces, as shown in Figure 4-5. The domain was discretized as detailed in Section 4.3.2, to obtain an average near-wall mesh resolution of $y^+ \simeq 1$ in the wall-normal direction. This condition was checked specifically over the casing where the average value of $y^+ = 1$. Figure 6-16 was obtained from the flow solution. The computational domain and mesh, imported in OpenFOAM 3.2 Extend, were delimited by the boundary conditions of Figure 4-5. The stagnation properties inlet and the pressure outlet boundary conditions used the measured flow state in experiment, reported in Table 4-3. Predictions were obtained with both the RNG k-epsilon model and the k-omega SST model, to evaluate the turbulence model closure influence on the CFD predictions. The convergence criteria of Section 4.5.1 were used for these steady-state simulations.

The one-and-half stage CFD model of the Aachen Turbine was validated by comparison with experiment, following the same procedure as for the validation of the turbine stator cascade in Section 6.2.1. Figure 6-6 (a) compares the radial profiles of pitch-averaged velocity components downstream of the rotor exit plane predicted by the RANS k-ω SST and the RNG k-ε models against the measurements from RWTH Aachen. The velocity profiles are in broad agreement through the centre of the passage, whereas the tangential velocity component appears somewhat under-predicted near the hub. As this investigation is mainly concerned with the effect of the casing wall treatment, the agreement appears satisfactory for the purpose of the current work. This is due to the fact that, whereas a specific inlet boundary layer profile was generated over the casing, using an auxiliary CFD computation as detailed in Section 4.5, the boundary layer thickness over the hub at the computational domain inflow was neglected. This is due to a convergent fairing being used in experiment to mate with the hub wall, as shown in Figure 4-1. The convergent fairing, which was not modelled, is expected to have inhibited the growth of the hub wall boundary layer. This effect was coarsely approximated by neglecting the boundary layer thickness at the computational domain inflow.

Figure 6-6 (b) shows a similar trend, with the numerical predictions giving a high over-turning close to the hub and an overall better agreement with the measurements above 0.4 blade spans. The k-ω SST turbulence closure appears to give predictions marginally closer to the measurements near the casing and therefore the predictions from this model are used in the remainder of this work.

Figure 6-7 compares the radial profiles of pitch-averaged velocity components and yaw angle from CFD at 8.8 mm downstream of the stator 1 against the corresponding experimental measurements from RWTH Aachen. The predicted radial profiles of velocity components in Figure 6-7 (a) and of yaw angle in Figure 6-7 (b) appear to follow closely the corresponding profiles measured by RWTH Aachen, as shown by the different lines substantially overlapping the symbols across the full span.

Figure 6-8 compares the measured and predicted radial profiles of pitch-averaged velocity component and yaw angle at 8.8 mm downstream of the stator 2. The radial profiles of velocity predicted by CFD in Figure 6-8 (a) appear to reasonably follow the corresponding measurements from RWTH Aachen, as shown by the lines running alongside the symbols across the most of the span. The radial distributions of the absolute velocity and of the circumferential velocity component above the hub and the casing, up to 10% of the blade span, is slightly under-predicted. This may be related to the use of a convergent-divergent nozzle in experiment downstream of stator 2, which was not modelled in CFD. Figure 6-8 (b) shows that the radial profile of pitch-averaged absolute outflow angle predicted by CFD is a fairly good match to the corresponding measured profile, across most of the span. At the stator 2 exit, the predicted flow appears to locally under-turn at around 80% of the blade span compared to experiment, by about 2 degrees.

The mean absolute error and the root mean square error defined in Equations (6.1) and (6.2) quantify the average error in the circumferential velocity between the predictions and the reference experimental measurements in Figures 6.6-6.8 (a). These values are listed in Table 6-1 and show that errors are less than 6% of the mean circumferential velocity.

Table 6-1

Mean absolute error and root mean square error between experiment and CFD.

Validation test case	MAE	RMSE
Stator 1	2.28	2.81
Rotor	1.09	1.58
Stator 2	7.1	9.2

The main trends in the experimental profiles appear to be well reproduced by the numerical model. This indicates that the CFD model is likely to be adequate for guiding the endwall casing design, which is the main purpose of this study, even if some discrepancies are acknowledged close the hub at the rotor outlet. For design purposes, it is often adequate to predict the relative change in turbine stage loss rather than predicting its absolute value, so as long as the right trends are captured, the CFD method is likely to be appropriate for driving the design optimization.

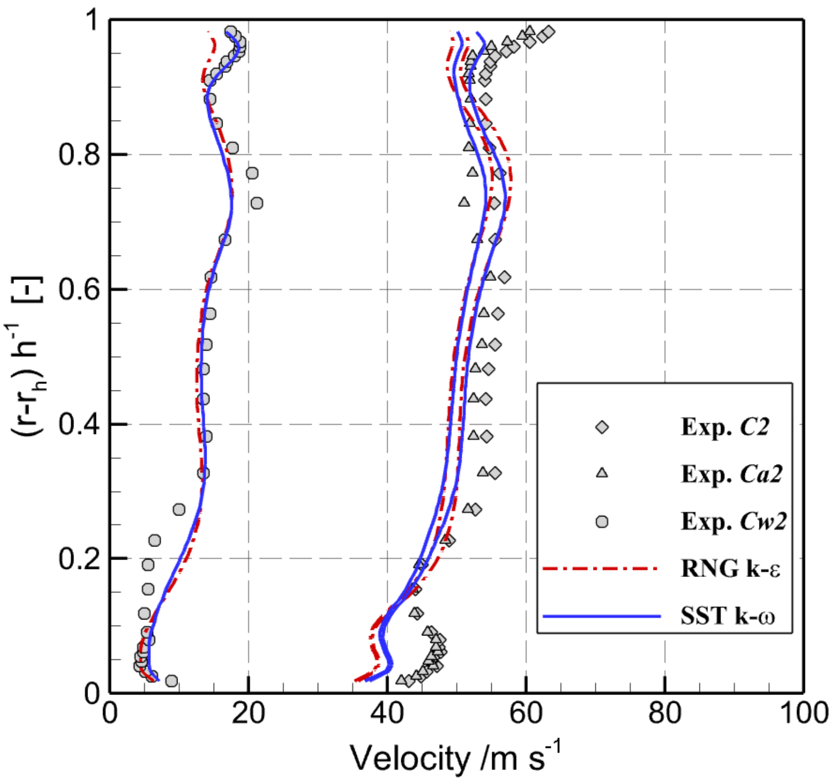

(a)

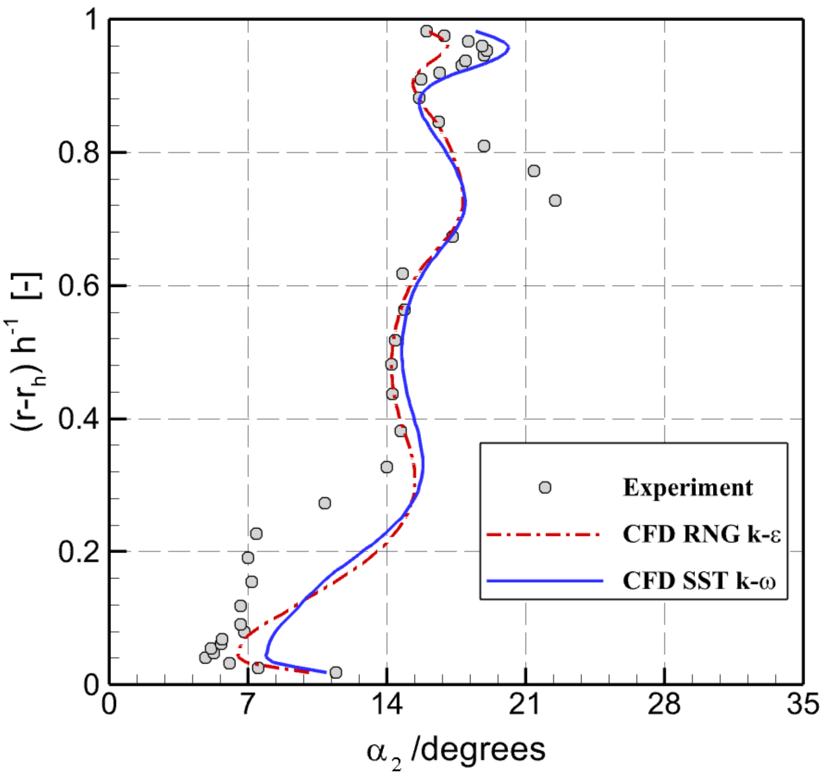

(b)

Figure 6-6: Radial distributions of pitch-averaged (a) velocity components and (b) yaw angle at 8.8 mm downstream of the rotor exit plane.

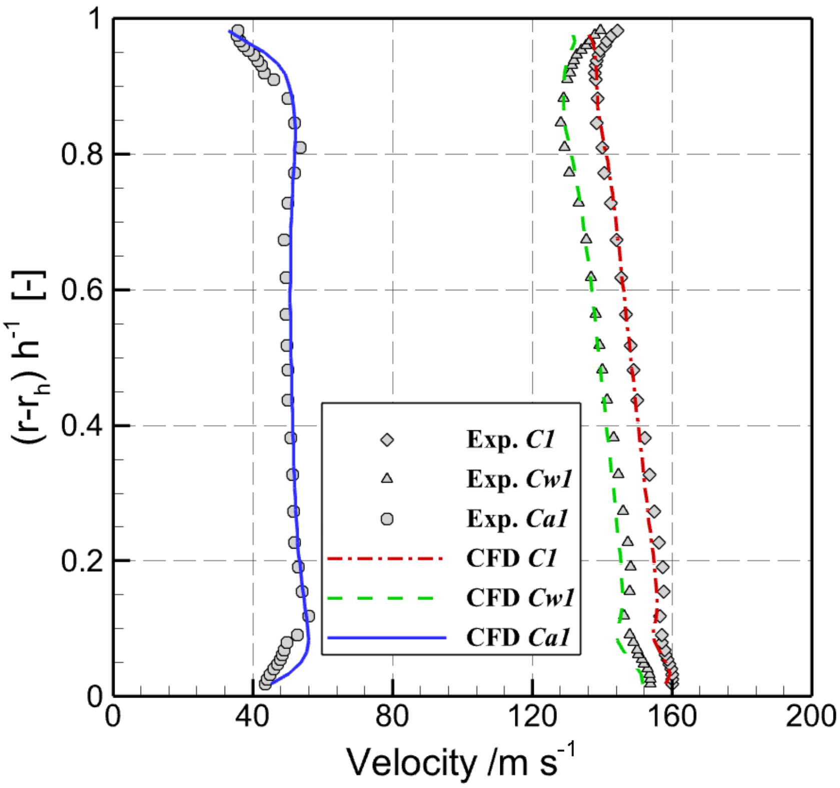

(a)

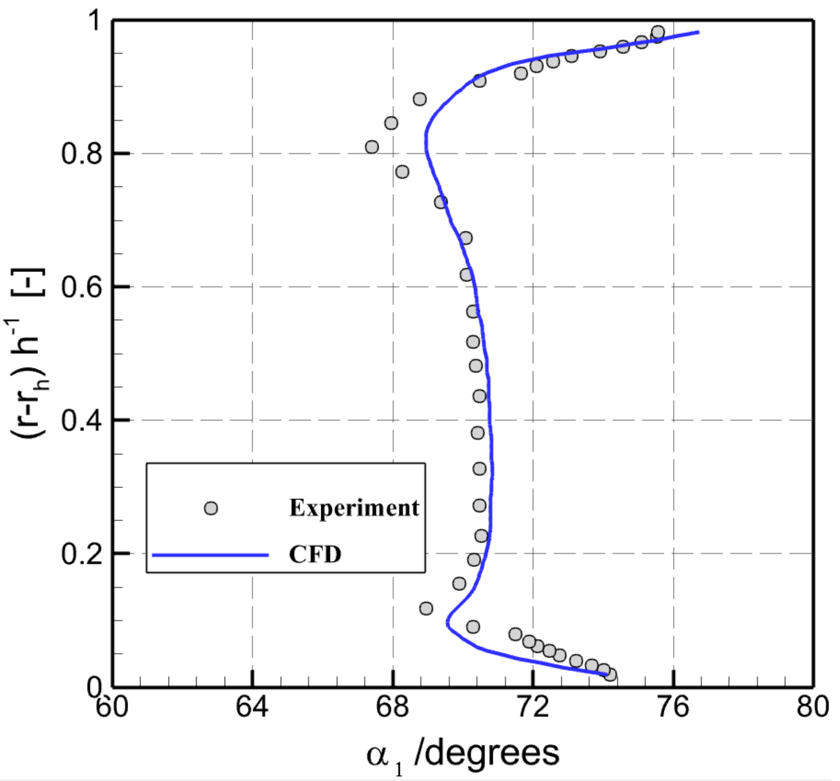

(b)

Figure 6-7: Radial distributions of pitch-averaged (a) velocity components and (b) yaw angle at 8.8 mm downstream of the stator 1 exit plane.

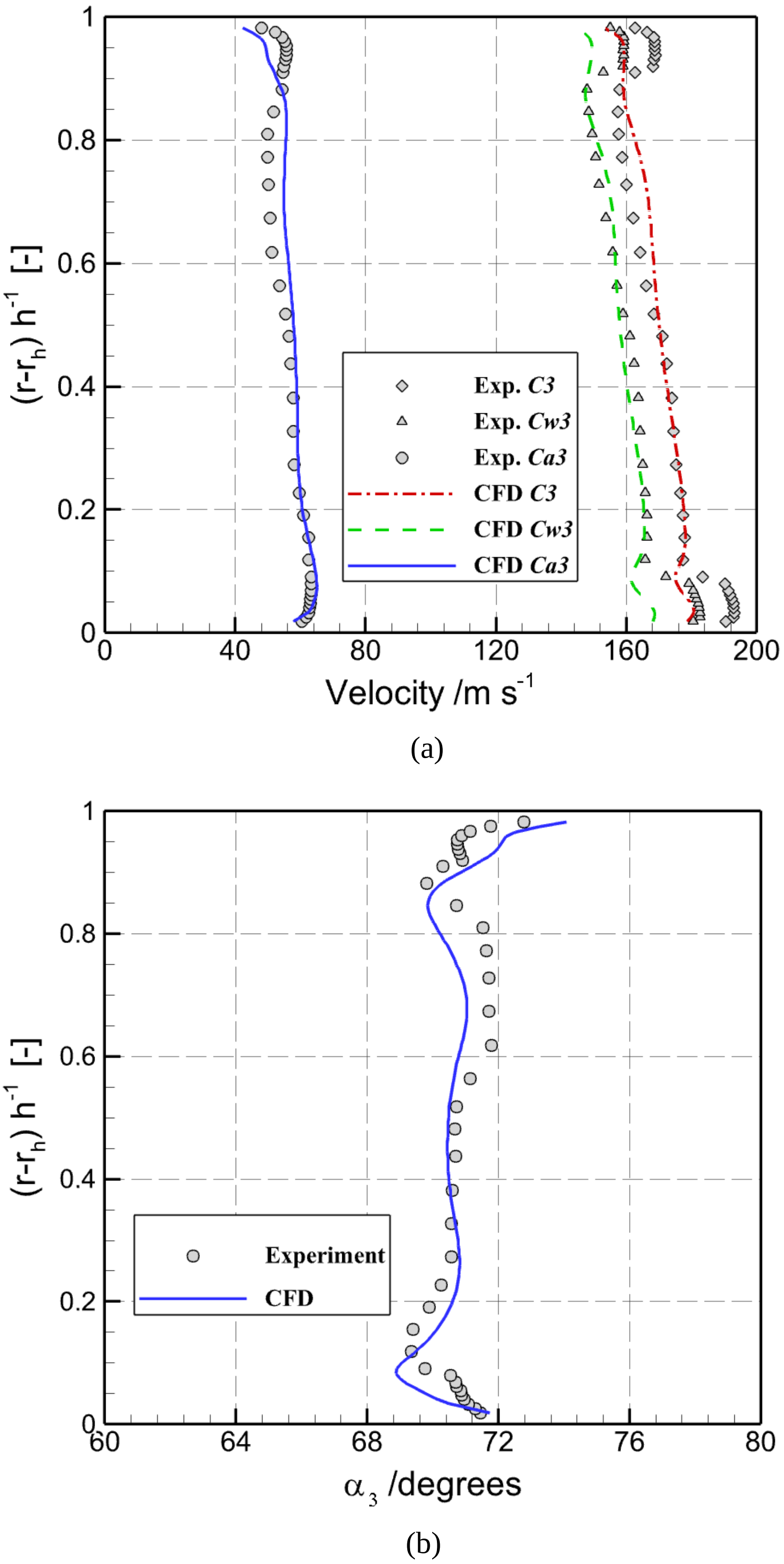

Figure 6-8: Radial distributions of pitch-averaged (a) velocity components and (b) yaw angle at 8.8 mm downstream of the stator 2 exit plane.

6.3.2 Extension of the guide groove feasibility study to the full 1.5 stage Aachen Turbine

The non-axisymmetric stator 1 casing design was applied to the one and half stage Aachen Turbine using the same workflow of APOW that was used to generate the non-axisymmetric turbine stator cascade. A preliminary feasibility study of using the guide groove for improving the flow through the full stage was performed. The aim of this preliminary study was limited to determining whether a guide groove applied to the stator 1 casing would cause measurable and potentially beneficial effects to the flow further downstream. In view of this limited scope, only four casings with different groove shape parameter values were tested. The same boundary conditions discussed in Section 4.5 were used for all four test cases.

Two main variables are used in the parametrization of the non-axisymmetric turbine stator 1 casing with a guide groove: The maximum groove depth location along the groove path $\mu(x, \theta_g)$ and the groove pitchwise width $w(x, \theta_g)$. Three casing geometries were built to test the effect of the groove pitchwise width and one geometry tested the effect of the groove maximum depth location. Case 1 used a constant groove width along the groove path. In Case 2, the groove from Case 1 is widened monotonically up to the mixing plane (1) to twice its starting width. Case 3 starts the groove with a narrower width at the leading edge, which is then expanded to the same width at Case 2 at the trailing edge. The maximum groove depth location along the groove path $\mu\ (x, \theta_g)$ for all three cases was set as 45% of the groove total length. In Case 4, the maximum groove depth location was set at 65% of the groove total length.

6.3.2.1 Stage performance with and without contoured casing

The total pressure loss coefficient C_{Pt} evaluated across the stator, C_{Pts}, and across the stage, C_{Ptr}, was used to evaluate the non-axisymmetric casing design. The comparison of the stator row and stage total pressure loss coefficients obtained from the four cases reported in Table 6-2 shows that a larger reduction in the total pressure loss coefficient is achieved by altering the groove trailing edge width w_{te}, between Case 1 and Case 2, than by altering the groove leading edge width w_{le}, between Case 2 and Case 3. Similarly, a larger reduction in the total pressure loss coefficient is achieved by altering the position of the groove maximum depth μ between Case 3 and Case 4 than by altering the groove leading edge width w_{le}, between Case 2 and Case 3. μ and w_{te} appear to be more significant in determining the stage pressure loss than w_{le}. Case 4 delivers the best total pressure loss reduction. Therefore, the aerodynamic predictions from Case 4 are further analysed by comparison with the validated CFD predictions of the baseline turbine flow with an axisymmetric casing.

The new casing design (Case 4) was then tested numerically at off-design by reducing the rotor speed to 2510 r.p.m. This set point operation was reported by Gallus and Zeschky (1992) as lowering the turbine isentropic efficiency due to higher secondary flow losses.

Table 6-2

Baseline and contoured Aachen Turbine performance

Conditions	**Cases**	ΔC_{Pts} **(%)**	ΔC_{Ptr} **(%)**	**Parameters of the contoured casing**
Design	Case 1	-0.318	-0.159	$w_{LE} = \ w_{TE} = 0.02\, rad, \mu \approx 45\%$
	Case 2	-3.45	-0.628	$w_{LE} = 0.02\, rad,\ w_{TE} = 0.04, \mu \approx 45\%$
	Case 3	-2.88	-0.791	$w_{LE} = 0.006\, rad,\ w_{TE} = 0.04\, rad, \mu \approx 45\%$
	Case 4	-5.844	-1.42	$w_{LE} = 0.006\, rad\ \ w_{TE} = 0.04\, rad, \mu \approx 65\%$
Off design (72% $\dot{\theta}$)	Case 4	-6.276	-1.58	$w_{LE} = 0.006\, rad\ \ w_{TE} = 0.04\, rad, \mu \approx 65\%$

6.3.2.2 Analysis of the contoured casing impact on the passage flow

Having determined that the guide groove can potentially improve the stage performance, it is of interest to study what changes take place in the flow compared to the validated CFD model of the one and half stage Aachen Turbine, which uses an axisymmetric casing. The latter is used as the baseline flow in the flow analysis, which used Tecplot 2017 as the CFD post-processor.

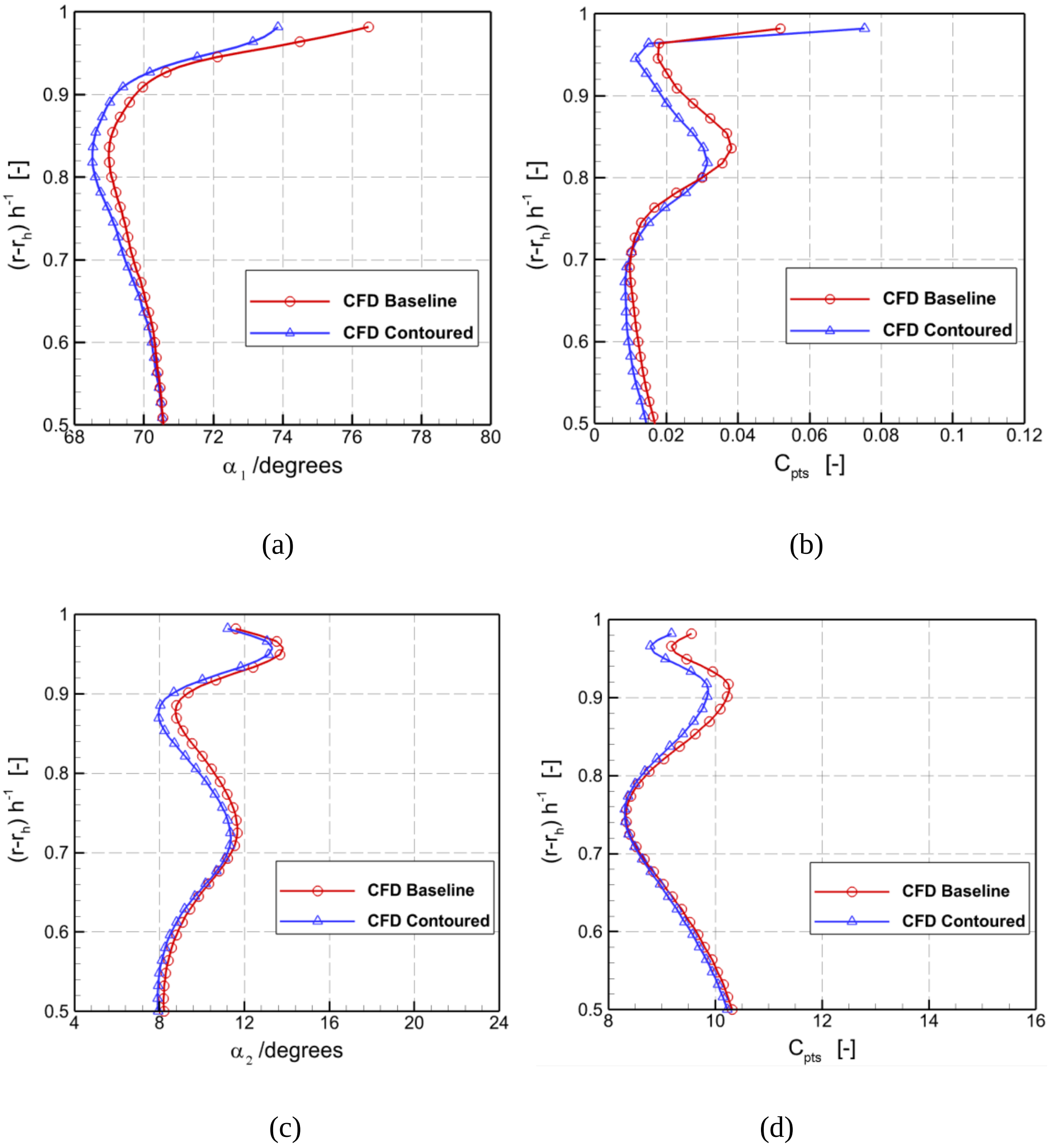

Figure 6-9. Predicted pitch-averaged total pressure loss coefficients and yaw angles along the normalized span. (a,b) stator 1 plane, (c,d) rotor plane.

Figure 6-9 (a-d) show the mid-span to casing radial distributions of the pitch-averaged total pressure loss coefficient C_{Pts} and of pitch-averaged yaw angle α_1, at the stator 1 exit plane and downstream of the rotor exit plane. C_{Pts} and α_1 are compared between the baseline and the contoured casing simulations. The yaw angle distribution in Figure 6-9 (a) is mostly above the 70° design point. This results in overturning near the casing. The reason behind this is the effect of the cross-flow pressure gradient on the casing boundary layer, which more easily turns the less energetic flow compared to the mid-passage. By contouring the casing, Figure 6-9 (a) shows that this overturning is reduced, leading to a more spanwise uniform α_1. This change is associated to a reduction in the total pressure loss coefficient, as shown in Figure 6-9 (b).

The results downstream of the rotor are evaluated in the plane 2 of Figure 4-1, 8.8 mm behind the rotor trailing edge. The reduction in the overturning at the casing behind the stator 1 leads to a small reduction in the pitch-averaged yaw angle at the rotor exit, mainly towards the casing, as shown in Figure 6-9 (c). As a result, the pitch-averaged yaw angle distribution, α_2, appears to be more uniform with the contoured casing, below 0.9 blade span. The radial profile of the total pressure loss coefficient at the rotor exit, shown in Figure 6-9 (d), indicates an improved endwall flow, from a reduction in C_{Ptr} mainly towards the casing. This location of the reduction in total pressure loss coefficient close to the casing suggests a possible reduction in the rotor tip leakage loss. These changes lead to a reduction in the passage total pressure loss coefficient, as reported in Table 6-2.

For a further insight into the through-flow at design and at off-design conditions, Figure 6-10 presents the contours of the total pressure loss coefficients at 8.8 mm behind the stator 1 for both the baseline case and Case 4. Figure 6-10 (a) and (b) show the contours of C_{Pts} at the design point, while Figure 6-10 (c) and (d) show the contours of C_{Pts} off-design. In both figures, there is a core of high total pressure loss coefficient, which corresponds to the passage vortex (PV). The results indicate that the groove in the casing has reduced the passage core size at design and at off design. Figure 6-10 also shows that, at off-design, the new casing geometry provides a total pressure loss reduction comparable to that at the design rotor speed.

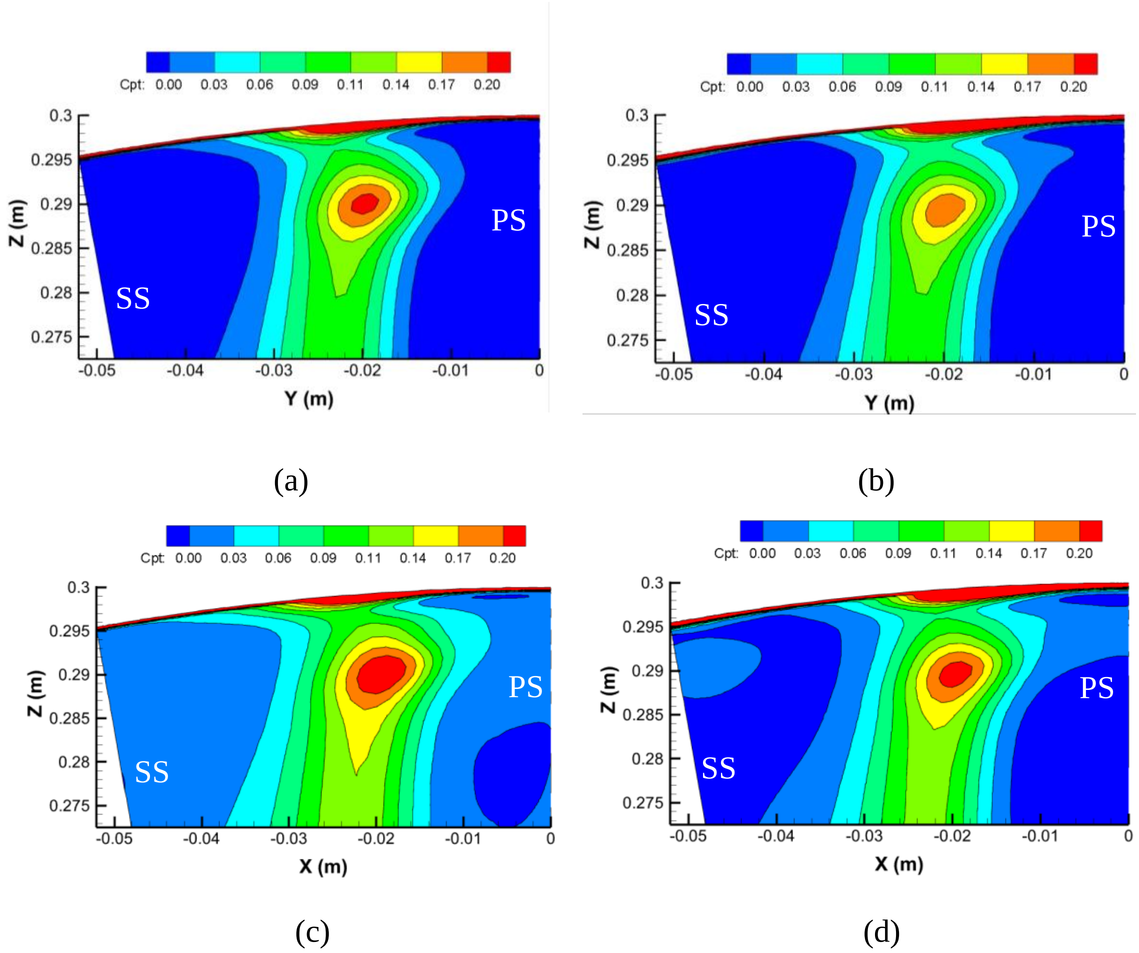

Figure 6-10. Contours of total pressure loss coefficient 8.8 mm behind the stator 1 at the axial stage design point (a, b) and off design (c, d); (a, c) axisymmetric casing, (b, d) contoured casing.

An additional insight into the effects of contouring the stator casing wall on the passage flow is provided by Figure 6-11, which shows contours of axial vorticity at $x = 0.8\,C_x$ at the design point with and without a contoured casing. From Figure 6-11, contouring the casing reduces the axial vorticity magnitude over the casing wall, which is indicative of a lower strain rate in the casing boundary layer. This would be consistent with a reduction of the passage cross-flow, from the pressure side to the suction side, that sees a longer and more tortuous path over the contoured casing than over the axisymmetric casing.

Contouring also appears to benefit the interaction between the suction side corner vortex, labelled as V_{cv} in Figure 6-11, and the endwall flow. With an axisymmetric wall, same sign axial vorticity from the casing appears to feed the corner vortex. With the contoured wall, this process is reduced. This may result in a lower streamwise growth rate of the corner vortex. This confirms that the presence of the groove has changed the secondary flow structure in the endwall region. Off-design, a similar pattern is obtained as in Figure 6-11.

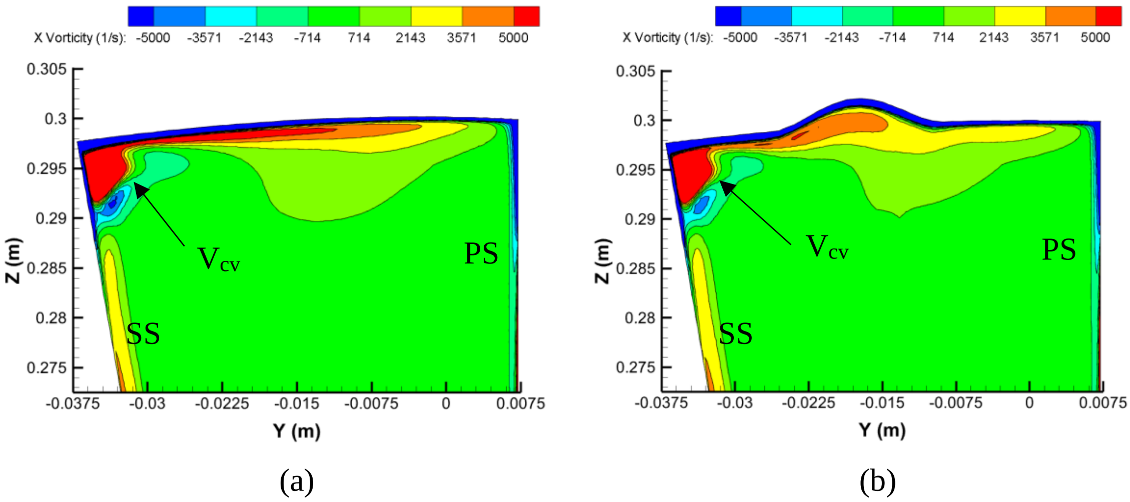

Figure 6-11. Contours of axial vorticity through stator 1 at 0.8 axial chords from the blade leading edge at the Aachen Turbine design conditions; (a) axisymmetric casing and (b) contoured casing.

The 3-D flow inside the rotor passage is dominated by the interaction of secondary flows from stator 1 with the passage vortex and the tip leakage vortex of the unshrouded rotor blade. Figure 6-12 shows the entropy distributions at the rotor passage exit with and without the contoured casing. It can be seen that the entropy 'core' that forms near the blade suction side tip reduces in peak value in Figure 6-12 (b) compared to Figure 6-12 (a). This is likely to indicate a reduction in the tip leakage vortex strength that in turns reduces the flow over-turning, as shown in Figure 6-9 (c).

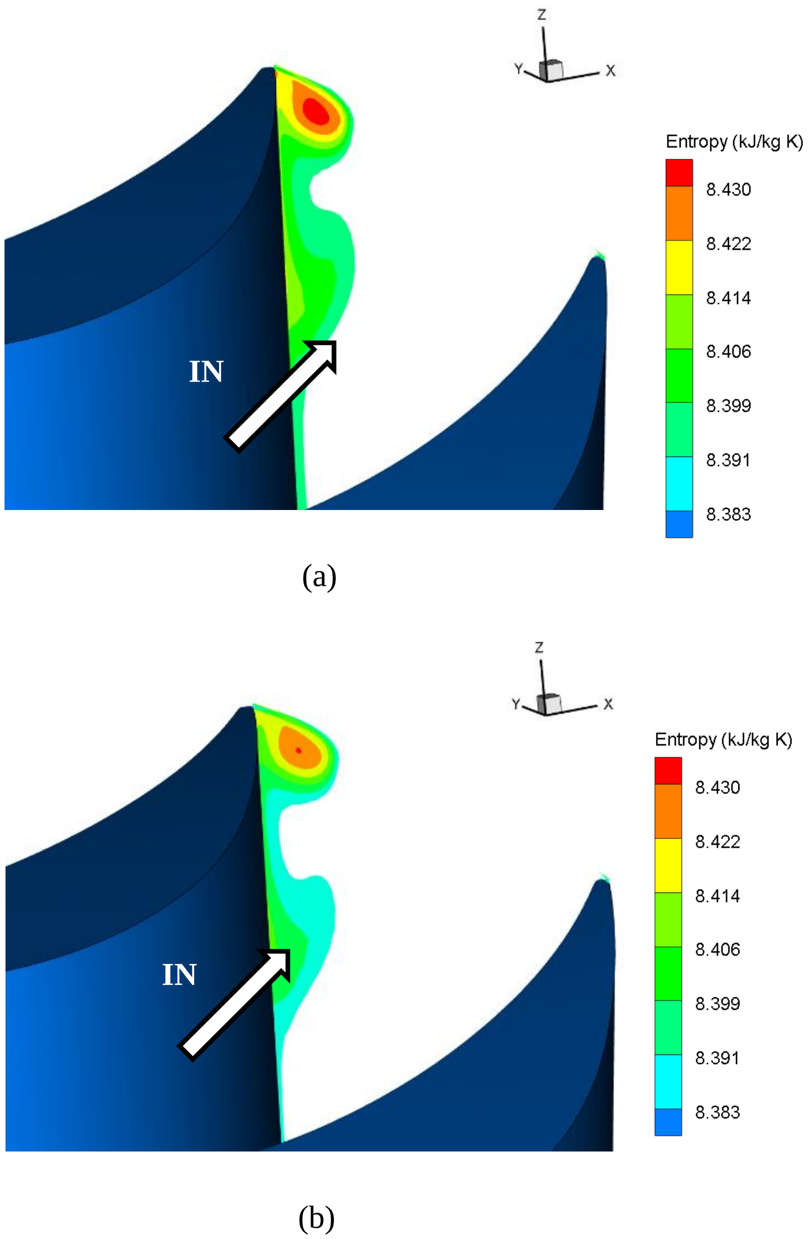

Figure 6-12. Entropy distributions at the rotor passage exit at the Aachen Turbine design conditions; (a) axisymmetric casing and (b) contoured casing.

6.4 Computer-based optimization of the contoured casing for the Aachen Turbine

It is of interest to explore a computer-based design process for axial turbines in which the casing geometry is optimized using modest user intervention within an acceptable timescale. To this end, the workflow of Section 5.5 in Chapter 5 is adopted and implemented by the Automated Process and Optimization Workbench (APOW) software. The optimization procedure is detailed in Chapter 5.

6.4.1 Optimization objectives

The optimization results are presented based on the new casing design for the two objective functions mentioned in details in Chapter 5. The second objective function that is the stage total pressure loss coefficients is selected for the optimization of the groove design and for the design optimization sensitivity analysis.

6.4.2 Design of experiment

In the optimization workflow of Chapter 5, knowledge is built into the surrogate model by performing numerical experiments. Each numerical experiment samples the parameter space of the contoured wall and returns a value of the total pressure loss. Therefore, each sample requires a full one and half stage CFD simulation. The number of samples is limited by the computational cost of each sample. A set of 10 sampling points is used by the Optimal Latin Hypercube design technique to populate the design space. The bounds in the casing parameters w_{te} and μ were set based on the result from the initial feasibility study in Section 6.3.2. Figure 6-13 shows the resulting sample spread, stated in terms of the groove width at the trailing edge w_{te} and of the axial location of maximum groove depth, μ. The changes in the response function, which is the stator row total pressure loss coefficient, are studied for different values of w_{te} and μ. Kriging in Figure 6-14 provides a continuous response function from a discrete sample of computational fluid dynamics estimates of the stator total pressure loss C_{Pts}. It enables to develop an insight of how the design parameters w_{te} and μ influence the performance of the turbine across the full extent of the parameter space and to identify regions of high performance, with acceptable sensitivity. From the Kriging results of Figure 6-14, a region of low C_{Pts} was identified over the range 0.025 radians $\leq w_{te} \leq$ 0.05 radians and $0.4 \leq \mu \leq 0.8$.

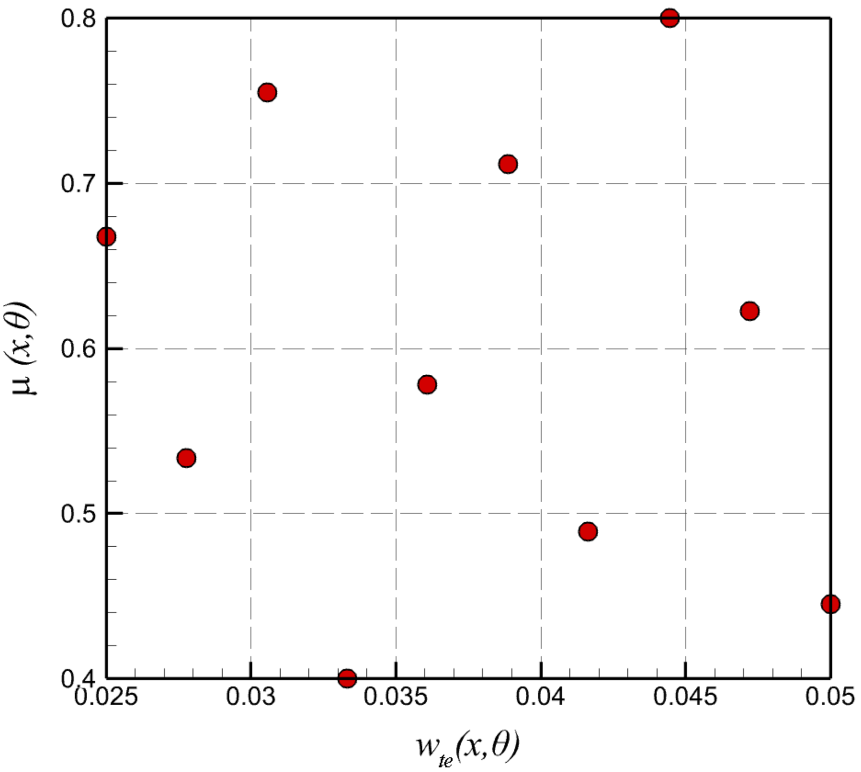

Figure 6-13: Initial sampling using the Optimal Latin Hypercube.

It is of interest to explore the flow features characterising this parameter space, which are explored in the next section. The optimum values of the design variables (w_{te}, μ) corresponding to the minimum value of C_{Pts} shown in Figure 6-14 are (0.0402, 0.66). It will be seen in the next section that these (w_{te}, μ) optimum values differ from the ones obtained by minimising the stage pressure loss coefficient C_{Ptr}.

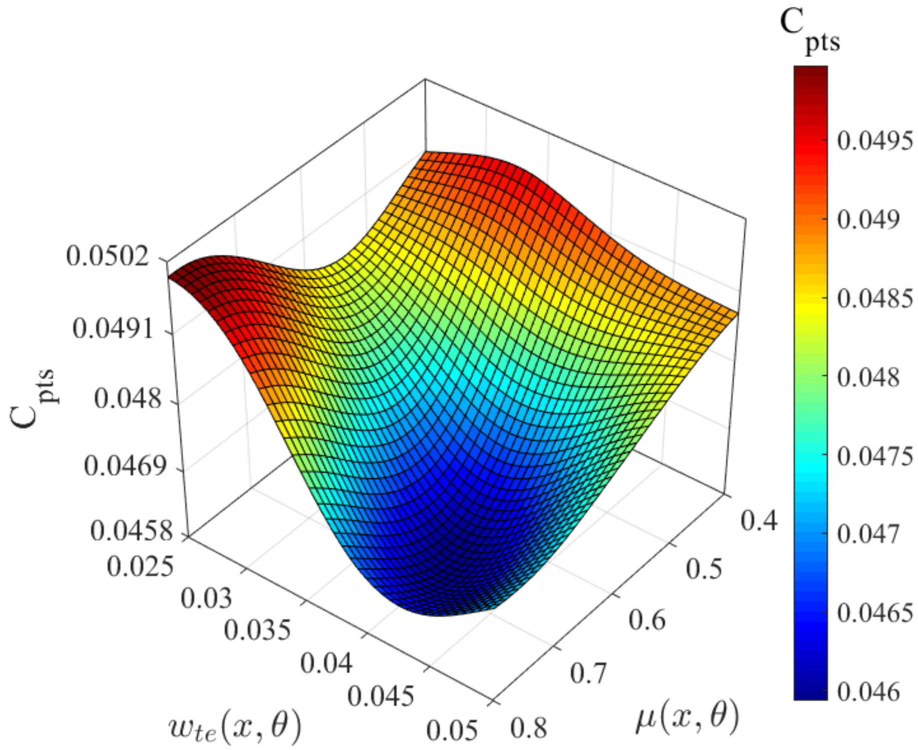

(a)

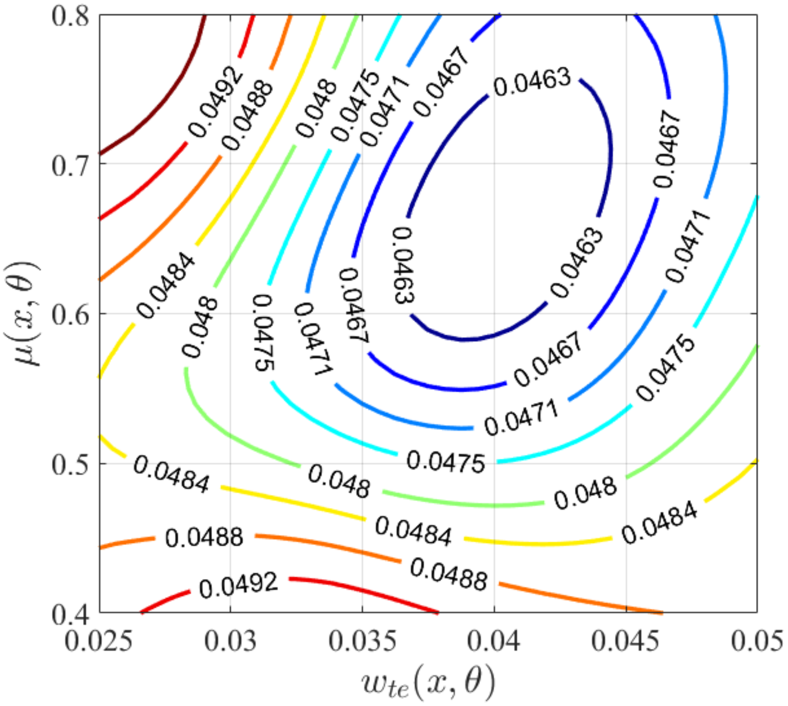

(b)

Figure 6-14: Optimization of the casing groove using 10 sampling points based on the stator row total pressure loss coefficient. Response function rendered as (a) 3D carpet plot and (b) by contours on the (w_{te}, μ) plane.

The optimization of the design variables is now considered using C_{Ptr} as the penalty function, since this relates more directly to the full stage performance and hence to the turbine efficiency. Figure 6-15 shows the response function of the optimization method, stated in terms of the stage total pressure loss coefficient. The same parameter space sampling of 10 points is used as for Figure 6-14. The optimized (w_{te}, μ) values identified by using the C_{Ptr} minimum in Figure 6-15 are (0.05, 0.6504).

The groove maximum depth position for reducing the average total pressure loss across the upstream stator, C_{Pts}, is 0.66 and it is similar to that for reducing the average total pressure loss across the stage, C_{Ptr}, 0.6504, with the difference being 0.0096. There is a greater difference between the trailing edge groove width that reduces more effectively the upstream stator loss, 0.0402, and the one that lowers more effectively the stage loss, 0.05. This difference arises from the knowledge that the design parameters that produced the best performance from a blade row are not necessarily the same parameters that lead to the best performance of the turbomachine, since the exit flow conditions affect the performance of the downstream blade rows. This difference evidences that the optimization of the aerodynamics through an axial turbine is a whole-turbine problem, in which the coupling between blade rows cannot be neglected, as stated by (Hadade and di Mare, 2016) and by (Na and Liu, 2015).

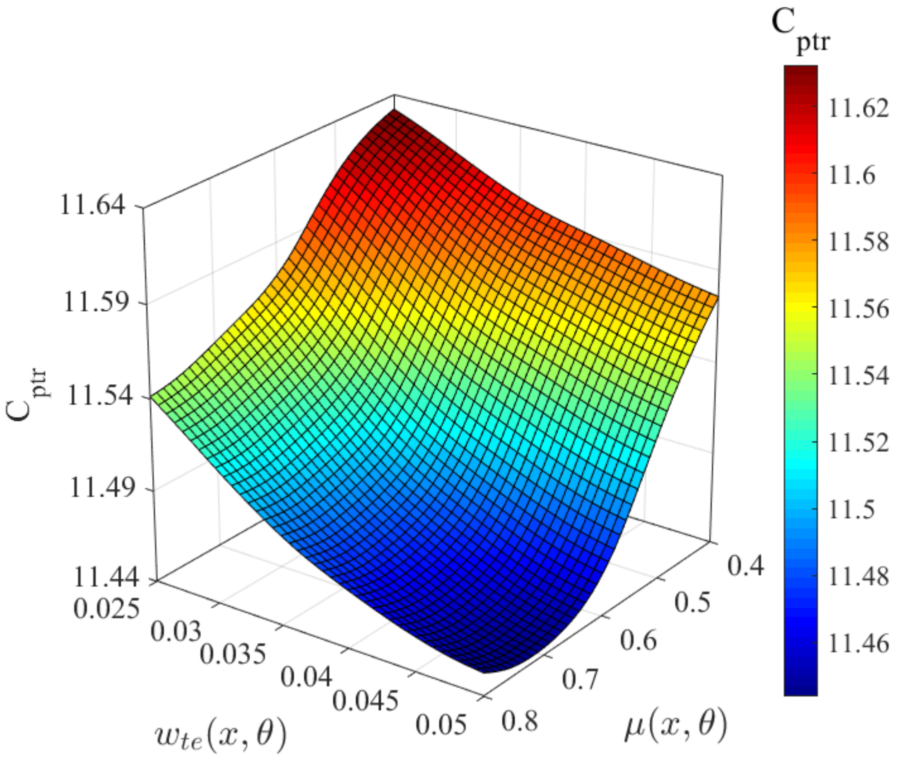

(a)

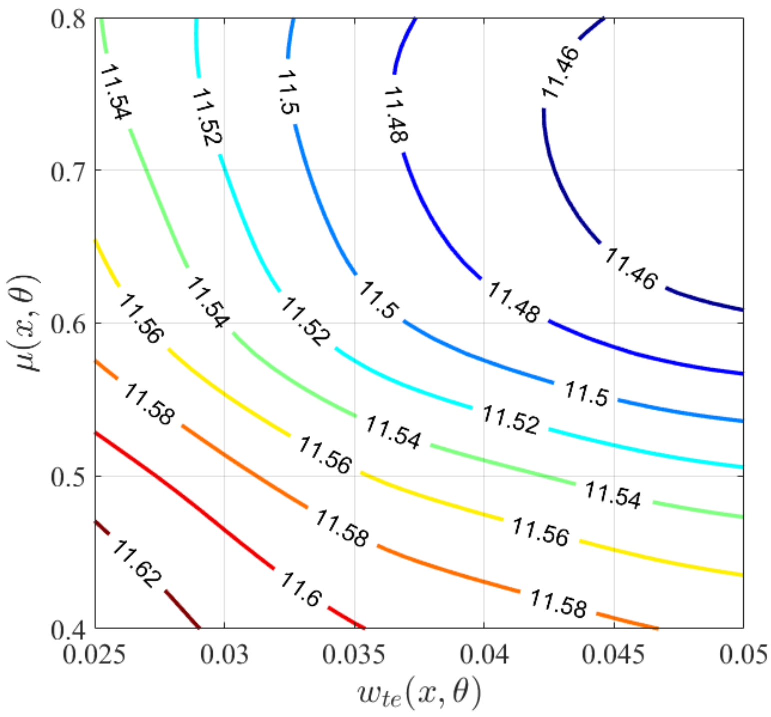

(b)

Figure 6-15: Optimization of the casing groove using 10 sampling points based on stage total pressure loss coefficient. Response function rendered as (a) 3D carpet plot and (b) by contours on the (w_{te}, μ) plane. w_{te} in radians.

In the optimization process, it is important to check whether an appropriate near-wall spatial resolution is maintained as different casing contour geometries are modelled. Figure 6-16 shows the average value of the first interior cell wall-normal normalized height y^+ over the casing, from the 10 CFD solutions with the (w_{te}, μ) combinations of Figure 6-13. These CFD solutions are shown by the filled circles in Figure 6-16. The average value of y^+ of the optimized casing, with w_{te}= 0.05 and μ = 0.06504, is shown by the filled diamond. Figure 6-16 shows that a near-wall resolution of $y^+ \approx 1$ is achieved and maintained through the optimization process. This is the same y^+ magnitude as that was used by Menter et al. (2003) for modelling a turbine stator guide vane.

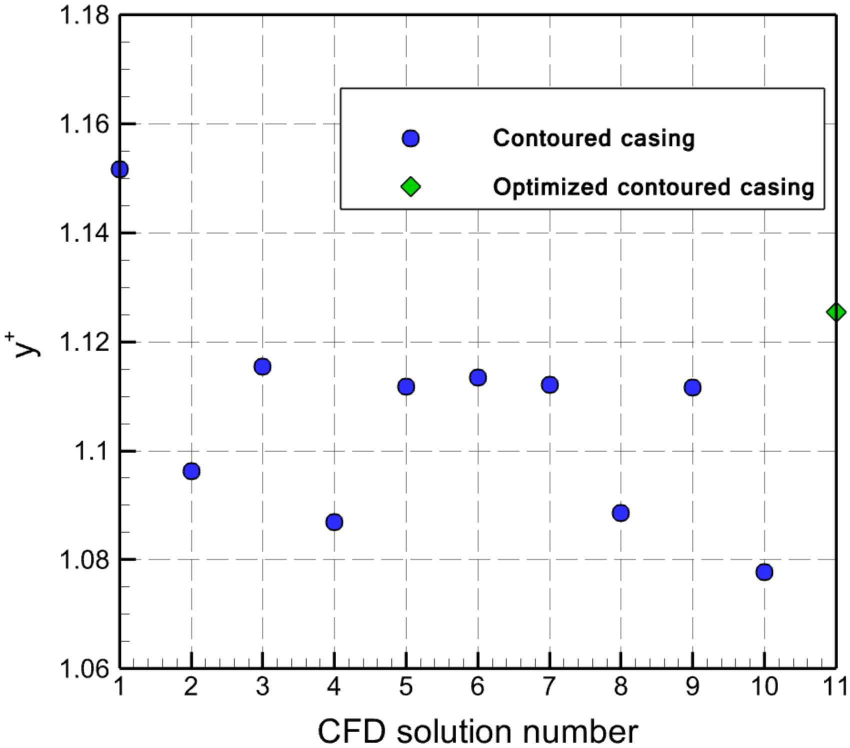

Figure 6-16: Average value of y^+ over the casing, for different non-axisymmetric casing parameter values.

6.4.3 Sensitivity analysis and quality indicator

A sensitivity analysis on the optimized geometry from Section 6.4.2 is performed by the adaptive sampling method detailed in Section 5.4. Figure 6-17 shows the initial and the adaptively selected samples that are generated using the Optimal Latin Hypercube. The green filled circle represents the geometry parameters for the casing optimized from the set of 10 samples of Figure 6-13. The geometry parameters for the casing optimized by applying adaptive sampling is shown by the green filled triangle.

The response function obtained from combining the initial and the adaptively selected samples (20 points) is shown in Figure 6-18. By comparing Figure 6-15 (a) and Figure 6-18 (a), it is possible to appreciate that adding the 10 additional samples shown by the blue filled triangles in Figure 6-17 appears to have increased the definition of the shape of the response function C_{Ptr} in the neighbourhood of the lowest C_{Ptr} value, denoted by p^{opt} in Figure 6-17. There appears to be a steeper valley in Figure 6-18 (a) defining this C_{Ptr} minimum, suggesting a greater div (C_{Ptr}), which is indicative of a greater localization of the C_{Ptr} minimum in the (w_{te}, μ) space. The (w_{te}, μ) location of the optimal value from Figure 6-18 is shown in Figure 6-17 to be slightly different than that from Figure 6-15.

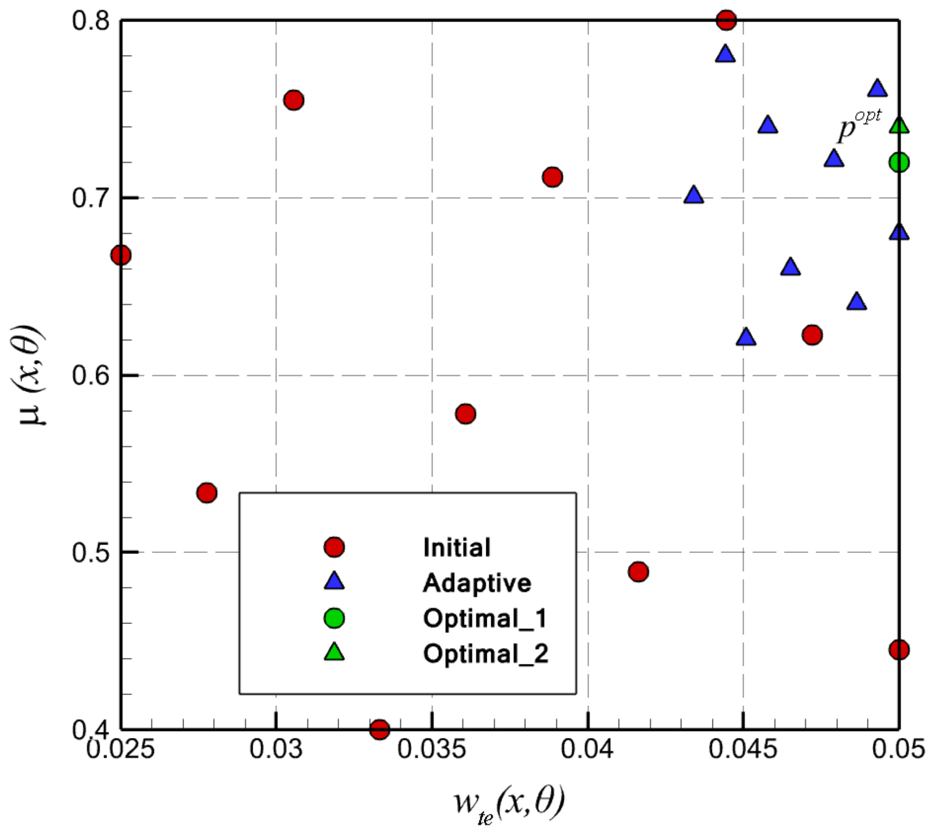

Figure 6-17: Initial and adaptive sampling using the Optimal Latin Hypercube.

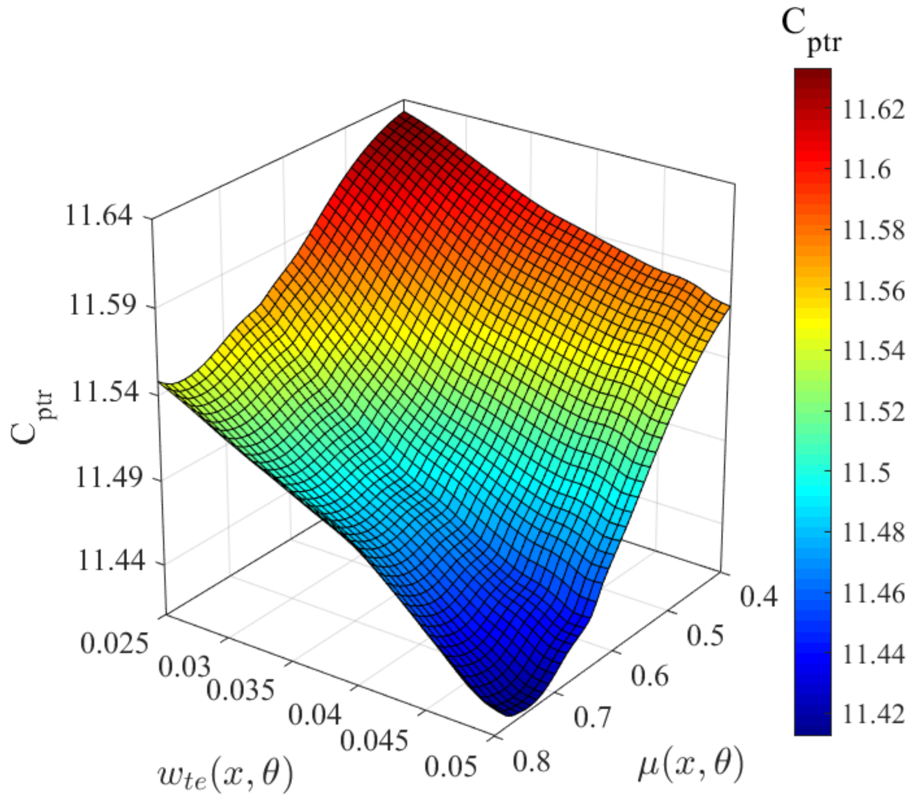

(a)

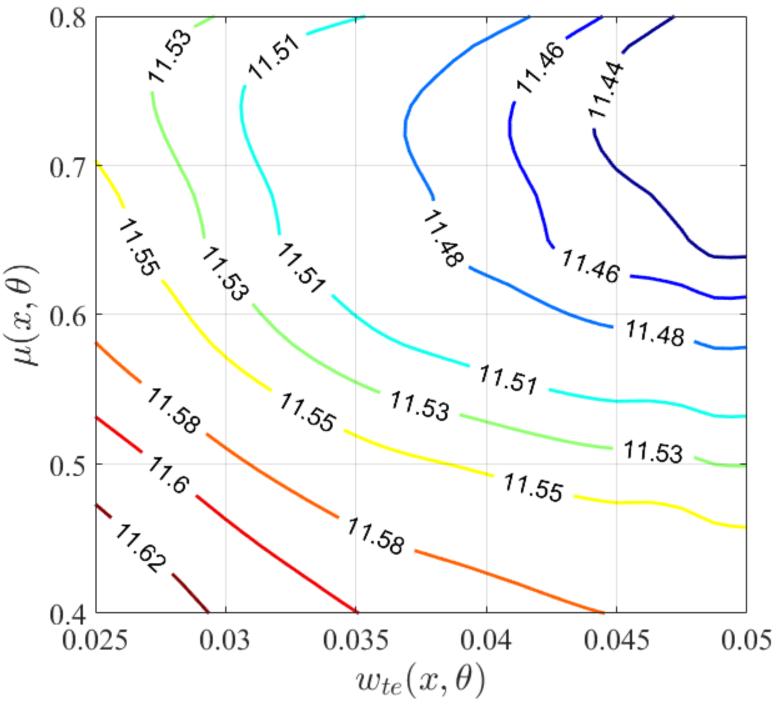

(b)

Figure 6-18: Optimization of the casing groove using 20 sampling points, based on the stage total pressure loss coefficient. 10 points are from the adaption procedure.

Figure 6-19 (a) plots the predicted values against the observed values of the response function C_{Ptr}. Each prediction is obtained by generating a Kriging model using 9 out of 10 points from the set used in Figure 6-15 and computing the C_{Ptr} at the tenth point. The predicted value is C_{Ptr} as determined from this Kriging model and the observed value is C_{Ptr} as determined from CFD. This test is designed to explore the sensitivity of the Kriging model on the sampling of the (w_{te}, μ) parameter space. Figure 6-19 shows a linear fit through the data, by the continuous red line. This line lies very close to the bisector of the first quadrant, which indicates that the Kriging model estimates consistently values close to the ones from the CFD. The 50% confidence interval band, determined from the norm of the regressed residuals, is shown by the dashed lines. This band is shown to be reasonably narrow around the C_{Ptr} at (p^{opt}) and is 0.22% of C_{Ptr}. With the adaptive sampling procedure, Figure 6-19 (b) shows that, by repeating this sensitivity analysis with 19 out of 20 points, the 50% confidence interval band width reduces to 0.17% of C_{Ptr}. It is concluded that the dependence of C_{Ptr} predicted by Kriging on the specific selection of the points that inform the Kriging model is slightly reduced with 20 points and there appears to be little scope for increasing the number of sampling points beyond 20 to seek further large improvements in this agreement. There is a 50% probability that using a different sampling will result in a Kriging model that predicts a C_{Ptr} falling in the bands shown in Figure 6-19.

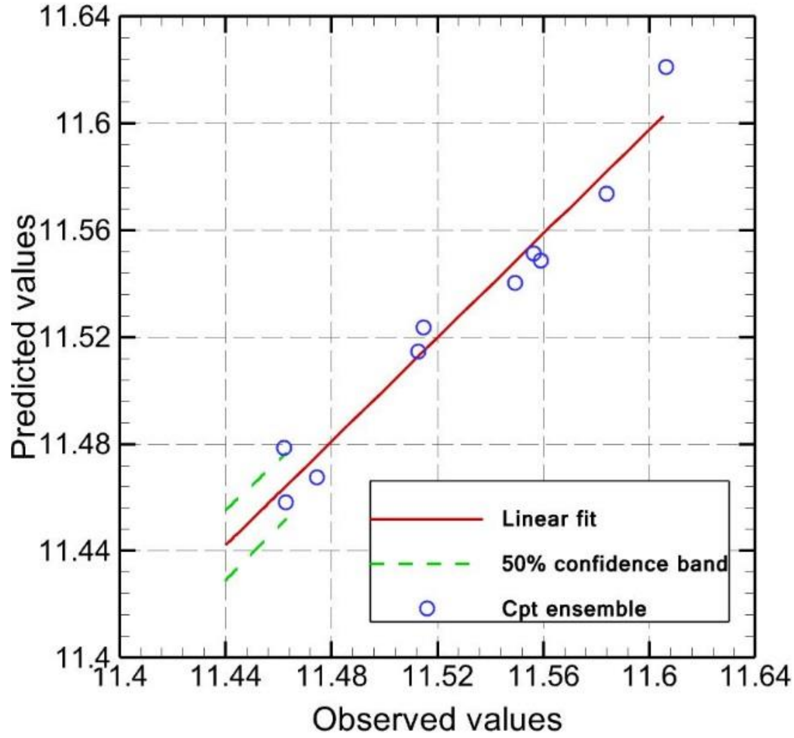

(a)

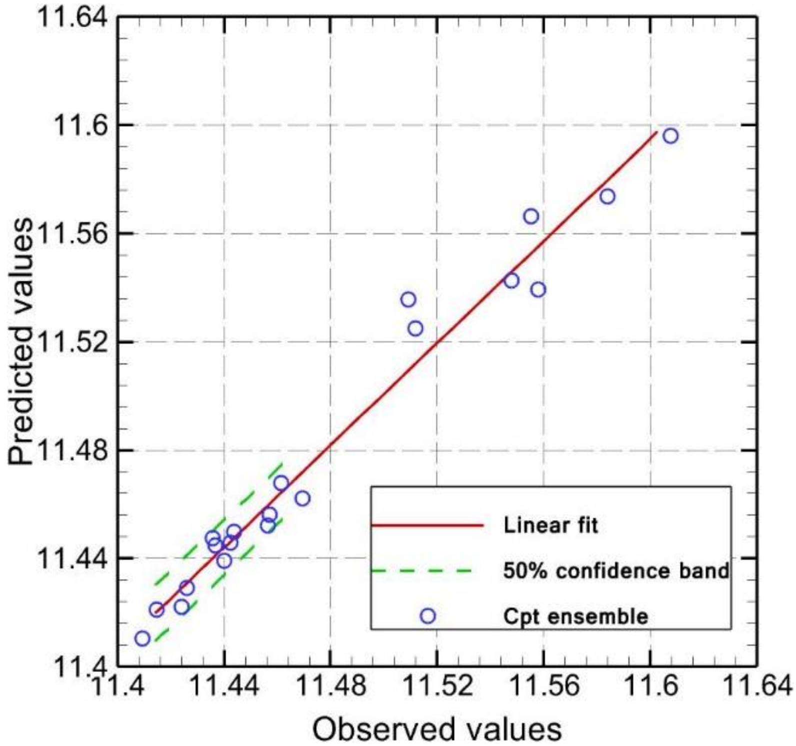

(b)

Figure 6-19: Observed and predicted values of the stage total pressure loss coefficient.

The minima of C_{Ptr} predicted from the Kriging models were verified by running CFD simulations at the (w_{te}, μ) of p^{opt}. These simulations predicted C_{Ptr} values very close to the ones from the Kriging models. The difference with the 10-point sample model was 0.2125 %, which is arguably too small to be verified in experiment. With a 20-point adaptive sample, the difference was 0.00276 % and therefore essentially immaterial. The percentage differences between the optimal stage total pressure loss prediction from Kriging and from CFD for both sets confirm a good model data fit. The values of Table 6-3 are calculated based on the definitions for δC_{Ptr}, ϵ_1 and ϵ_2 in Section 5.4.

Table 6-3

Response function percentage improvement and error in the reduced order models (Kriging).

Response function	Baseline	Optimal_1	Optimal_2	δC_{Ptr} %	ϵ_1 %	ϵ_2 %
ΔC_{Ptr}	11.6205	11.4139	11.4067	3.5	0.2125	0.00276

From Figure 6-19 and Table 6-3, the adaptive sampling has shown to be able to improve the selection of p^{opt} over the initial design of 10 points, but the 3.5 % δC_{Ptr} performance gain is rather small. This improvement is arguably worth the additional computational cost of the 20-point sample, which is about double the one from the 10-point sample. Therefore, for future studies, the simple 10-point sampling is recommended as adequate for optimizing the diffusion surface casing design parameters.

The feasibility study in Section 6.3.2 indicated that larger beneficial changes to the stage average total pressure loss can be achieved by varying μ and w_{te} than by changing w_{le}, which motivated the optimization of the contoured endwall with respect to μ and w_{te}. It is now of interest to explore whether further reductions in the stage total pressure loss can be obtained by tuning the groove width at the leading edge w_{le}. The casing with the guide groove optimized for μ and w_{te} using the 20-point samples is taken as the reference geometry. Five different values of leading edge groove width w_{le} are examined for this geometry. Table 6-4 shows the stage total pressure loss coefficients predicted by CFD with the five different leading edge groove widths. The leading edge groove width used in the optimization of Figure 6-18 delivers the lowest stage pressure loss coefficient among the five CFD simulations. It can be seen that the w_{le} has a smaller effect on the stage performance compared to other two variables used in the optimization process. Figure 6-20 and Table 6-4 show that the maximum change in the value of C_{Ptr} over the five CFD simulations is 0.0087. This is quite small compared to the change in C_{Ptr} obtained by varying μ and w_{te} in the optimization process, as shown in Figure 6-18.

This result seems to confirm the findings from the feasibility study reported in Section 6.3.2, which is that μ and w_{te} are the leading parameters in the design optimization process of the guide groove casing, with w_{le} being a comparatively less influential design variable.

Table 6-4

Effect of the groove pitchwise width at the leading edge on the average stage total pressure loss coefficient.

w_{le} / radians	0.004	0.006	0.1	0.15	0.021
C_{Ptr}	11.4073	11.401	11.4067	11.4097	11.4071

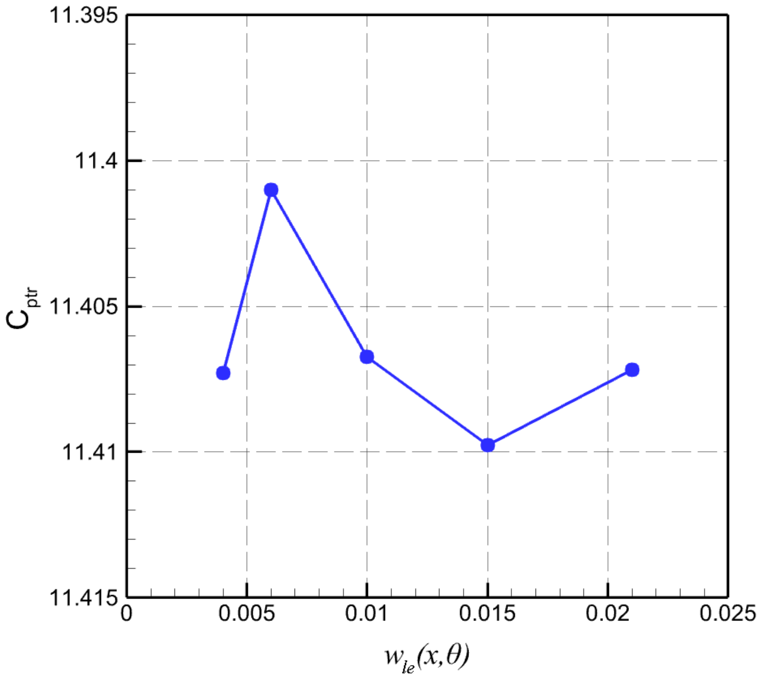

Figure 6-20: Effect of the groove pitchwise width at the leading edge on the average stage total pressure loss coefficient.

Figure 6-21 (a) shows the response function C_{Ptr} obtained from Kriging by varying R_3 and R_5 defined in Section 3.5.2 and shown in Figure 3-15. These points define axially the contoured casing designed by the controlled diffusion design method of Sun et al. (2014). The lowest C_{Ptr} is shown in Figure 6-21 (a) to be given with R_3 and R_5 set at approximately the same values of +3 mm. This generates a hump close to the blade suction side that mitigates the circumferential pressure gradient over the turbine casing passage. A similar mitigation was identified in Sun et al. (2014) using the static pressure coefficient distribution. Figure 6-21 (b) reports the accuracy of the Kriging model for this regression, using the same technique as that for Figure 6-19. Close to the lowest value of C_{Ptr}, the 50 % confidence band appears to be sufficiently narrow to give confidence in the predicted minimum value of C_{Ptr} from the Kriging model used for optimizing R_3 and R_5.

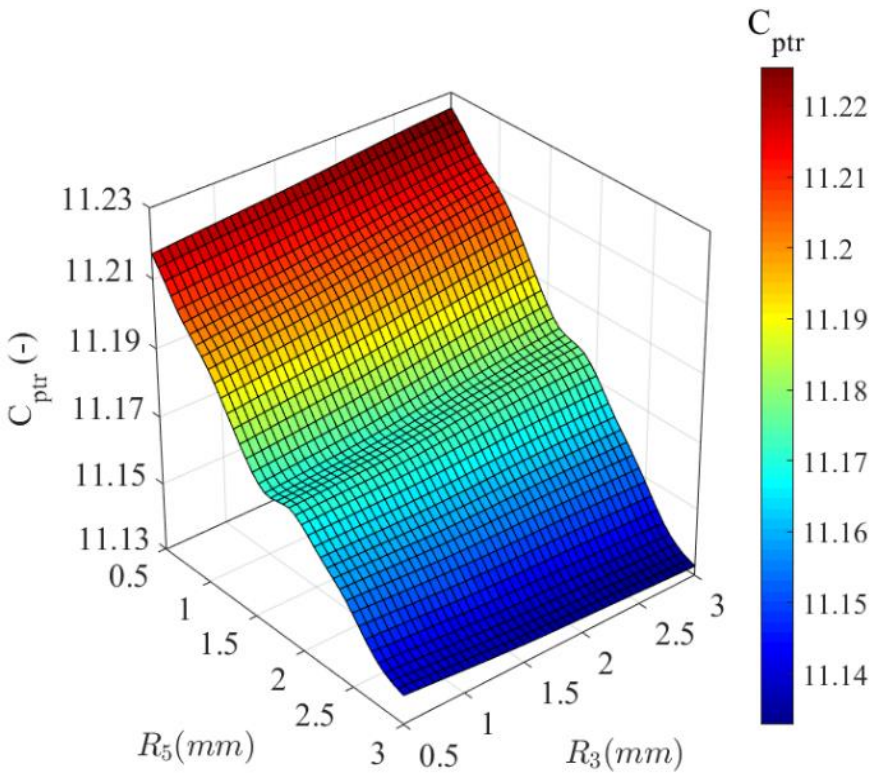

(a)

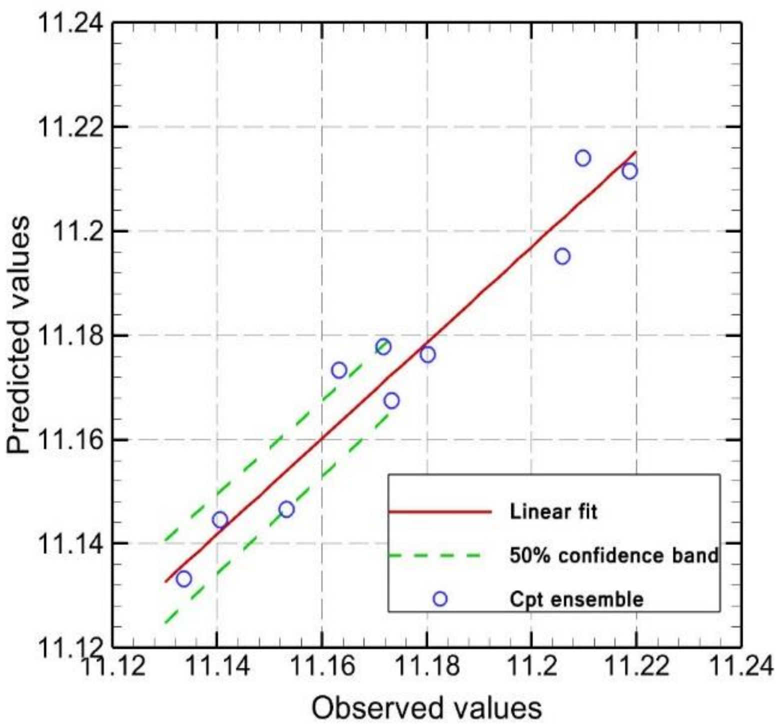

(b)

Figure 6-21: Optimization of the casing designed by the controlled diffusion method of Sun et al. (2014): (a) Kriging model response, (b) model quality indicator.

As mentioned in Chapter 4, each CFD solution used in the optimization process typically takes 10 hours of computer wall time on 30 HPC cores. Therefore, the wall time used for obtaining each response function was about 200 hours for the guide groove design and 100 hours for the diffusion design, as the CFD solutions were run sequentially, due to the available computational resources. Running the solutions in parallel would have reduced the wall time.

6.5 Flow analysis

6.5.1 Pitch-averaged blade row outflow

The validated simulation of the one and half stage Aachen Turbine flow passage was used as the baseline for studying the effects of the optimized casing. Figure 6-22 (a) shows radial distributions of the pitch-averaged yaw angle α_1 at the upstream stator exit plane, from the mid-span to the casing. Corresponding distributions of stage total pressure loss coefficient C_{Ptr} are shown in Figure 6-22 (b). The α_1 and C_{Ptr} profiles are shown from the baseline, the optimized groove, and the diffusion casing simulations. The yaw angle distribution in Figure 6-22 (a) is mostly above the $70°$ design point for all three casing types. This results in overturning near the casing. This is due to the cross-flow pressure gradient on the casing boundary layer, which more easily turns the less energetic near-wall flow compared to the mid-passage flow. The contribution to the stage total pressure loss coefficient from the mid-span up to 0.9 blade span is predicted to be lowest by the diffusion casing design in Figure 22 (b). However, the optimized groove casing design is shown to be the most effective in reducing the flow over-turning close to the casing, resulting in the most spanwise uniform yaw angle among the three designs.

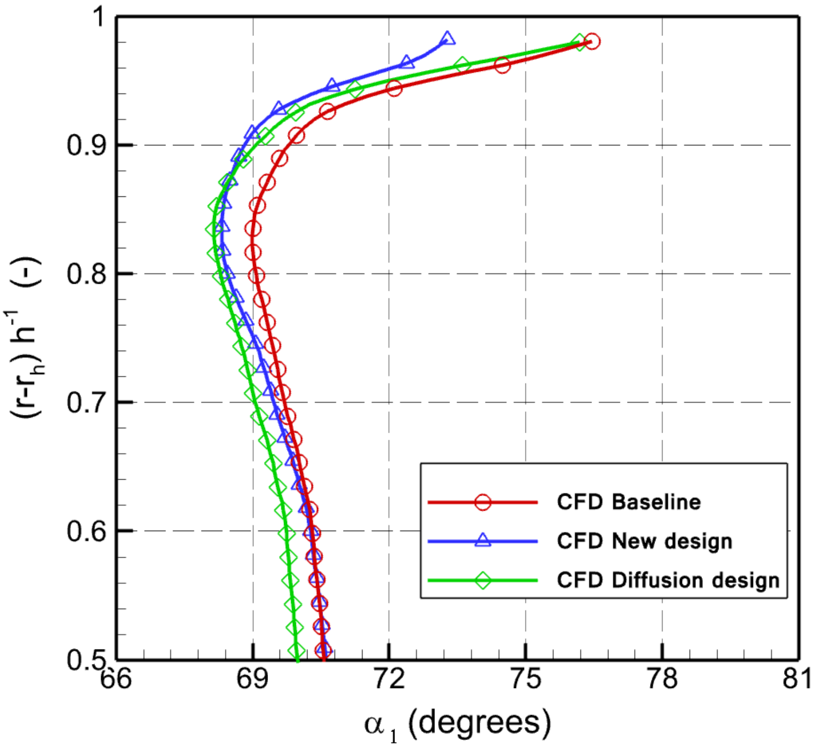

(a)

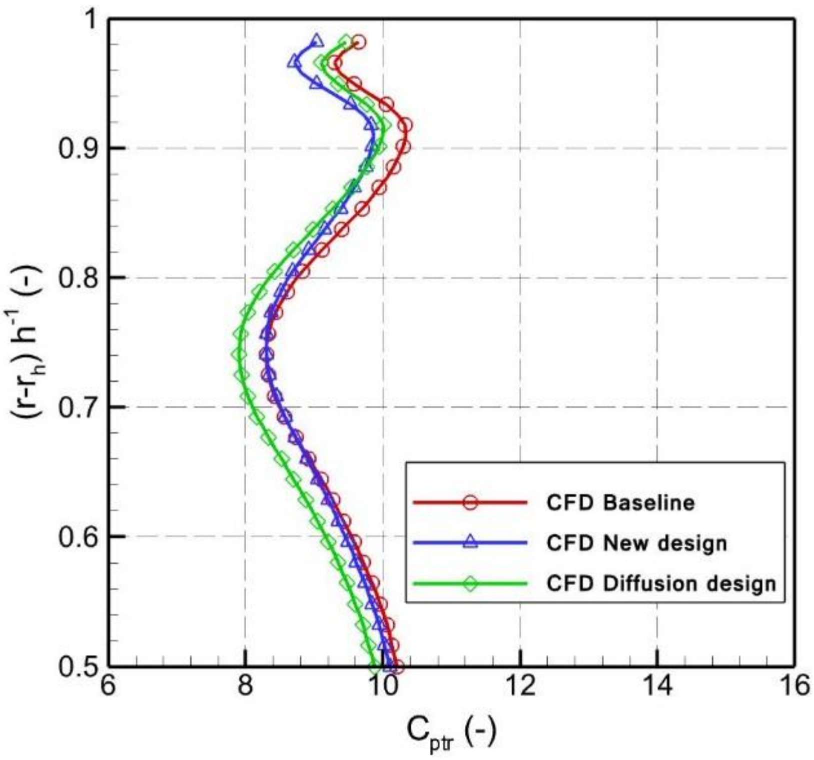

(b)

Figure 6-22: Predicted pitch-averaged radial distributions of (a) yaw angle 8.8 mm downstream of the stator 1 exit plane, and of (b) stage total pressure loss coefficient 8.8 mm downstream of the rotor exit plane.

Further away from the casing, between 50% and 70% of the blade height, Figure 6-22 (a) shows that the α_1 radial distributions from the axisymmetric and the optimized groove casing configurations are similar to one another, whereas the diffusion casing design gives a lower turning. This results in a change in the inlet angle to the rotor that in turns most probably reduces the specific work output. The lower work rate extraction from the working fluid reduces the main flow total pressure drop across the rotor. This partially explains the lower C_{Ptr} predicted between 50% and 80% of the blade span with the diffusion casing design compared to the other two configurations, shown in Figure 6-22 (b). At mid-span, α_1 with the diffusion casing design is predicted to be below the design turning angle of 70° and it is lower than α_1 from the other two test cases. The under-turning of the flow at 50% blade span explains why the diffusion casing design reduces C_{Ptr} at mid-span to a greater extent than the guide groove casing design, as shown in Figure 6-22 (b).

The coefficient of secondary kinetic energy C_{ske} was also evaluated 8.8 mm downstream of the rotor exit plane and it is shown in Figure 6-23. C_{ske} is defined as in Ingram et al. (2002) as

$$C_{ske} = \frac{U_{sec}^2 + U_r^2}{U_{ups}^2} \tag{6.3}$$

where U_{ups} is the reference stage inlet velocity, $U_{sec} = U\sin(\alpha - \alpha_{mid})$, and $U_r = U\sin\beta$. α_{mid} is the rotor exit flow angle evaluated at the blade mid-span in the stationary frame of reference and β is the rotor exit flow angle in the moving (rotor) frame of reference.

In Figure 6-23, the region of high C_{ske} between 65 % and 85 % span shows the presence of a rotor casing passage vortex whereas the region of high C_{ske} between 90 % and 98 % span identifies the presence of tip leakage. An increase in the secondary kinetic energy coefficient is predicted by using the optimized diffusion design at these span-wise locations compared to the baseline case. The C_{ske} remains higher than the baseline across the remainder of the blade span, as shown in Figure 6-23. Conversely, the optimized guide groove design is shown in Figure 6-23 to reduce the secondary kinetic energy coefficient across the span, compared to both the baseline and the optimized diffusion designs.

These changes in the coefficient of secondary kinetic energy were found to mirror the changes in the isentropic stage efficiency of the turbine. Specifically, the optimized groove casing was predicted to increase the stage isentropic efficiency by 1.13 % compared to the baseline axisymmetric casing. The isentropic stage efficiency of the turbine using the diffusion design method was predicted to marginally decrease, by 0.05 %. This appears to point to the importance of the flow over-turning highlighted in Figure 6-22 (a) close to the casing, which the optimized groove casing design appears to be able to mitigate whereas the diffusion design casing appears not to mitigate. The isentropic stage efficiency was calculated using (Turton, 2012):

$$\eta_{stage} = \frac{1-\frac{T_{t2}}{T_{t0}}}{1-\left(\frac{P_{t2}}{P_{t0}}\right)^{\frac{\gamma-1}{\gamma}}} \tag{6.4}$$

where T_t is the average total temperature and P_t is the average total pressure. The subscripts 0 and 2 denote the axial planes identified in Figure 4-1 and used in the calculation the total pressure loss coefficients.

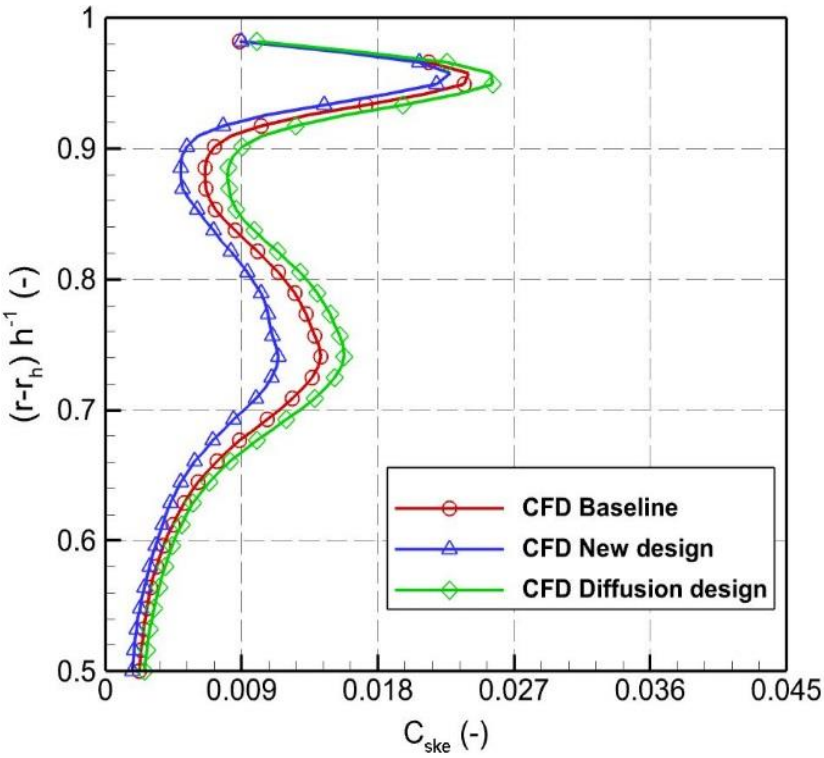

Figure 6-23: Predicted secondary kinetic energy coefficient pitch-averaged along the normalized span at 8.8 mm behind the rotor.

At the off design condition, a comparable improvement to the design stage efficiency was obtained by introducing the optimized groove casing. Introducing the optimized groove casing design is predicted to increase the isentropic stage efficiency by 0.97 %, while a marginal improvement of 0.085 % is predicted by introducing the optimized diffusion design. It may be possible to obtain a more substantial increase in the isentropic stage efficiency by enhancing the optimized diffusion design process by using the adaptive sampling of Section 6.4.3. However, this improvement may still not be as large as the one predicted by using a guide groove design. Performance gains are confirmed to occur both at design and at off design conditions using the optimized groove casing.

6.5.2 Flow patterns at axial planes through the stator and rotor passages

A further insight into the effects of contouring the stator casing wall on the passage flow is provided by Figure 6-24. This figure compares the contours of axial vorticity $\overline{\omega}_x = \omega_x U_{ups}^{-1} c$ with the axisymmetric and with the contoured casings, 8.8 mm downstream of the stator 1 exit plane. Figure 6-24 shows that the optimized groove casing design reduces the positive axial vorticity magnitude (+$\overline{\omega}_x$) located at y = -0.046 m and z = 0.295 m over the casing wall, which is indicative of a lower strain rate in the casing boundary layer. This would be consistent with a reduction of the passage cross-flow, from the pressure side to the suction side, which sees a longer and more tortuous path over the optimized groove contoured casing than over either the axisymmetric casing or the diffusion designed casing. The groove contoured casing design also appears to mitigate and raise the minimum axial vorticity ($-\ \overline{\omega}_x$) associated to the casing passage vortex at y = -0.018m and z = 0.286 m. The diffusion casing design shows a reduction in the size and peak magnitude of (+$\overline{\omega}_x$) of an area of high positive axial vorticity centred at y = -0.0125 and z = 0.294 compared to the baseline axisymmetric casing. This flow area appears to benefit less from the groove contoured casing design, which appears to mitigate the peak magnitude (+$\overline{\omega}_x$) of but not the size of this region.

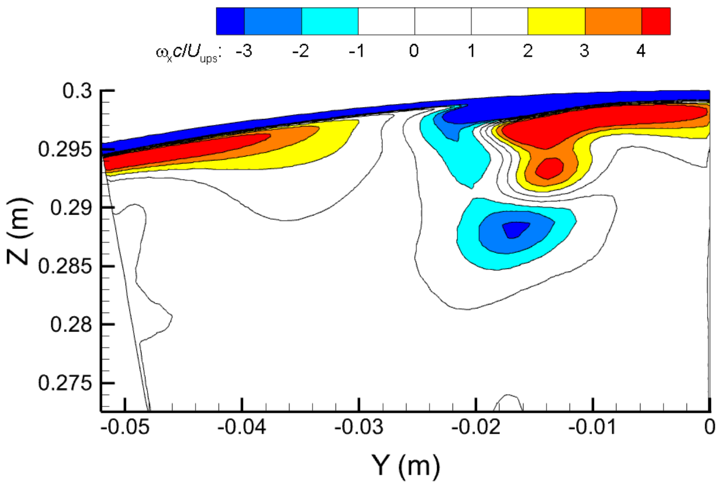

(a)

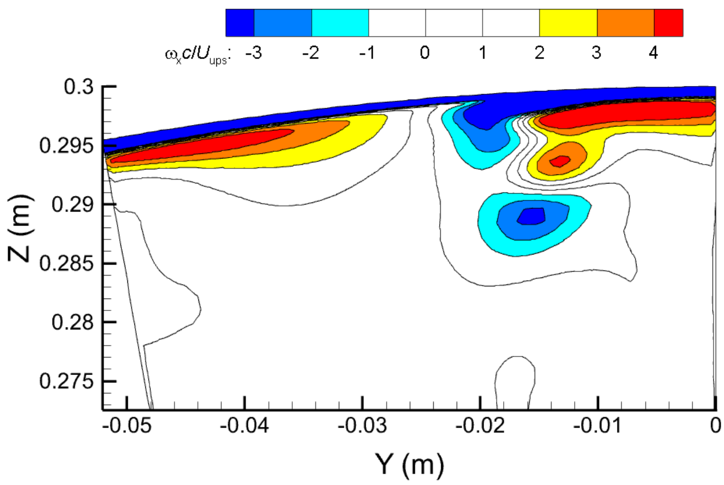

(b)

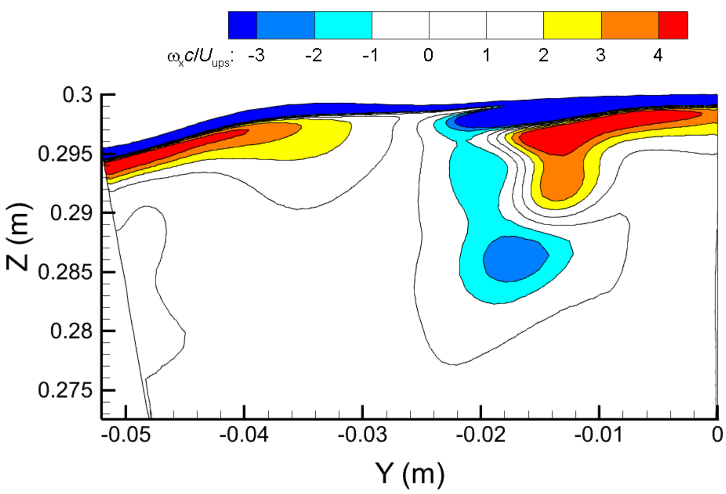

(c)

Figure 6-24: Contours of axial vorticity 8.8 mm downstream of the stator 1 exit plane. (a) axisymmetric casing, (b) diffusion casing, and (c) optimized groove casing.

It is of interest to study how the normalized turbulent kinetic energy changes through the stage as the casing is modified from the baseline axisymmetric design to a contoured casing. To this end, the normalized turbulent kinetic energy behind the mixing plane 1 and close to the rotor blade leading edge was evaluated. The contours of normalized turbulent kinetic energy of Figure 6-25 show that the contouring affects the turbulent kinetic energy approaching the rotor close to the casing. Specifically, there is a slight difference in the turbulent kinetic energy close to the casing between the axisymmetric casing and the diffusion design. A more pronounced change in the normalized turbulent kinetic energy distribution is obtained with the optimized groove casing design, by which the region of elevated turbulent kinetic energy near the casing is reduced in radial size. This reduction is consistent with the reduction in the axial vorticity upstream of the mixing plane 1 that was shown in Figure 6-24. As a flow structure with secondary motion moves from the stator to the rotor, it is typically cut through the rotating blades. In the simulation, this process is modelled by the conversion of axial vorticity into entropy through the mixing planes. Mitigating the secondary flow structures would lead to a reduction in the entropy generation across the mixing plane and this offers a plausible explanation for the trends shown in Figure 6-24 and in Figure 6-25.

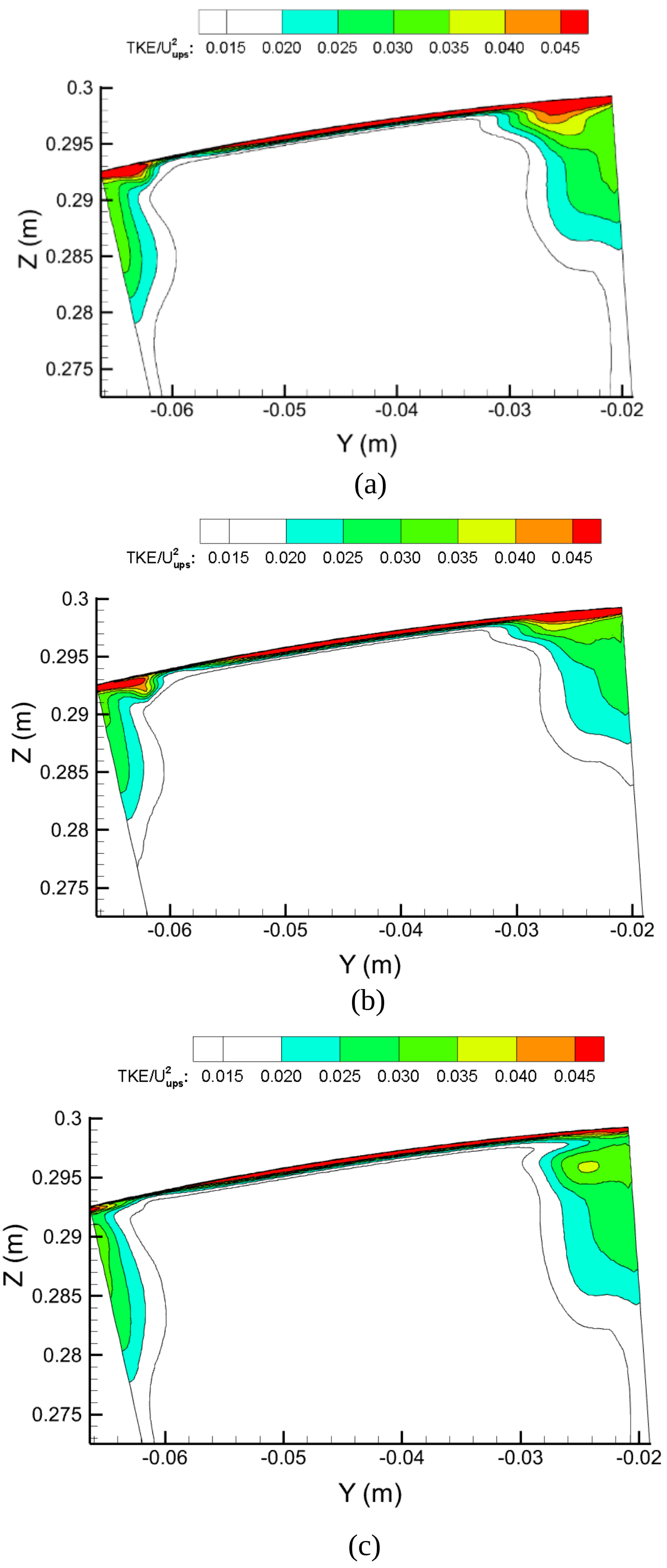

Figure 6-25: Contours of normalized turbulent kinetic energy downstream of the mixing plane 1. (a) Axisymmetric casing, (b) diffusion casing, and (c) optimized groove casing.

6.5.3 Flow pattern at the casing

It is of interest to explore the effect of contouring on the static pressure distribution over the casing, since changes to the casing static pressure can significantly influence the secondary flows (Ingram et al., 2005), (Saha and Acharya, 2008), (Luo et al., 2011), (Hu and Luo, 2014), (Schobeiri and Lu, 2014) and (Shahpar et al., 2017). Design approaches that exploit this method include three-dimensional blading, axial lean, and compound circumferential blade lean, in addition to casing treatments. Therefore, the static pressure distribution over the casing is analysed following a similar approach as in Schobeiri and Lu (2014).

Figure 6-26 shows by contours the static pressure distribution on the casing predicted by the three endwall geometries: the axisymmetric casing, the optimised diffusion casing, and the optimised groove casing. As the flow expands through the passage, Figure 6-26 shows that the static pressure decreases to a minimum value where indicated by the black arrow and then increases towards the passage exit. This area of flow diffusion generates an unwanted adverse pressure gradient that makes the flow over the blade suction surface more prone to separation. Figure 6-26 shows that the suction side boundary layer sees almost the same exit pressure, as indicated by the similar placement of the contour level indicated by the dashed arrows in Figure 6-26 (a), (b), and (c). Figure 6-26 (c) shows that the optimized groove casing generates a static pressure minimum of lower magnitude located further upstream compared to the axisymmetric design and the diffusion casing design. This reduces the adverse pressure gradient, mitigating the secondary flow structure growth. The diffusion design is shown in Figure 6-26 (b) to broaden the area of low static pressure over the blade suction side compared to the axisymmetric casing. The static pressure minimum occurs further downstream, which reduces the blade surface over which the flow diffuses. This is a positive feature, however, proximal to the suction side trailing edge, the flow undergoes a more rapid diffusion to meet the pressure equilibrium condition from the pressure side flow. While this latter diffusion is undesirable, Figure 6-24 (b) shows that the resulting stator outflow streamwise vorticity is still lower and therefore better than with an axisymmetric casing.

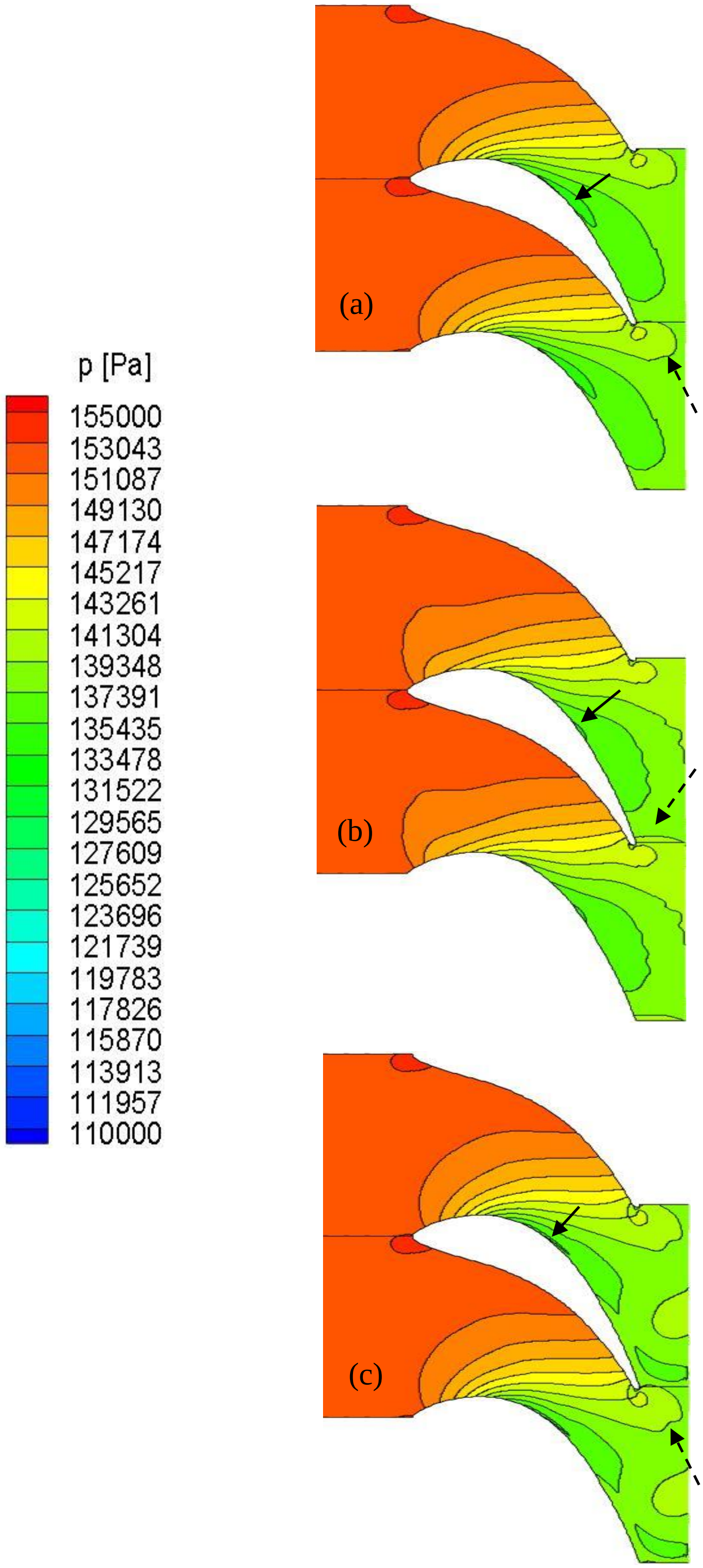

Figure 6-26: Contours of static pressure in the cascade plane close to the casing. (a) Axisymmetric casing, (b) diffusion casing, and (c) optimized groove casing.

6.5.4 Flow pattern on the rotor bade tip

To gain a further understanding of the rotor tip leakage flow with three different stator 1 casing designs, the static pressure distribution over the rotor blade tip is considered, as in Hilfer et al. (2012). The axisymmetric casing and the optimized diffusion casing designs display similar normalized distributions of static pressure $\bar{p} = 2p\rho_{ups}^{-1} U_{ups}^{-2}$ in Figure 6-27, which are characterized by a pressure minimum well localized at about 70% axial chords from the leading edge. The optimized groove design has a less localized pressure minimum where the pressure is higher than that of the other two cases. This is indicative of a reduction in the pressure gradient over the blade tip, from the pressure side to the suction side, which in turn may reduce the tip leakage strength, as also indicated by the change in the radial distribution of the secondary kinetic energy coefficient shown in Figure 6-23.

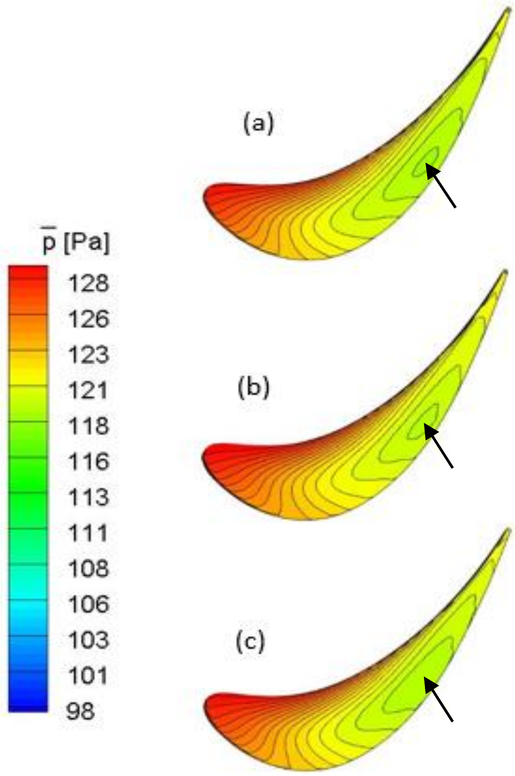

Figure 6-27: Contours of static pressure on the rotor blade tip for different stator 1 casing designs. (a) Axisymmetric casing, (b) optimized diffusion casing, and (c) optimized groove casing.

Chapter 7

Conclusions

This work has provided an important contribution to the concerted effort of the University of Leicester turbomachinery research group, headed by Dr Aldo Rona, engaged in finding new ways for improving the performance of axial flow turbines. It complements axial turbine hub design optimization research by Obaida (2017) and axial compressor casing optimization research by Kawase (2018). Specifically, this work has presented the proof of concept of an improved design process for turbines with a contoured casing. A steady RANS axial turbine model was validated against benchmark measurements of the Aachen Turbine, from RWTH Aachen. This model was then used for testing the effectiveness of different casing treatments. The current research work produced the following contributions:

- A new design for the turbine casing is introduced by a novel surface definition method.
- The new design uses a comparatively small number of free parameters that are shown by numerical modelling to give attractive increases in the stage isentropic efficiency.
- Limited work has been reported on using non-axisymmetric end-walls at the stator casing and on its interaction with the tip leakage flow. Therefore, this work provides further insight into the underlying flow dynamics.
- An efficient optimization workflow is developed with an improved adaptive sampling technique for obtaining more accurate predictions from a Kriging model.

Chapter 7 presents the main outcomes of this investigation, discusses the significance of the findings, and makes suggestions for further research.

7.1 A flow structure driven non-axisymmetric casing design

The literature indicates important gaps in the knowledge of endwall designs for axial turbines. There is currently no widespread consensus around a specific endwall treatment being best for enhancing the performance of axial turbines. Additionally, in the optimization process of a turbine, the number of the design variables is still large. This makes the optimization process computationally expensive. This work makes progress towards addressing these important knowledge gaps.

A new non-axisymmetric casing was introduced, based on a novel surface definition method that draws from observations of the typical secondary flow pattern over the casing. The new casing design technique is focused on manipulating specific flow structures directly. The ensuing change affects the surrounding pressure field. A set of parametric equations was used with the Beta distribution function to design the smooth casing groove path, which is a first application of the Beta distribution function to the contouring of a turbomachine casing. The Beta distribution was used as it avoids by construction any mismatch in the surface radial height at the outer perimeter of the grooved area. It was shown to improve the surface transition between the grooved area and the remainder of the casing compared to using a Normal distribution as in Reutter et al. (2013).

7.2 An effective casing design optimization workflow

A computer-based optimization workflow for the design of the turbine casing has been developed and implemented in batch mode using Automated Process and Optimization Workbench (APOW) software. This workflow was shown to be able to take advantage of the advances in the casing surface definition from Chapter 3 in its optimization design loop. Specifically, the casing surface parametrization of Section 3.6 has both a lower set of parameters and produces topologically smooth interfaces with the rest of the passage geometry, compared to some alternative parametrizations used in previous work. The casing designs modified in this work were optimized using the total pressure loss across the full stage as the target function, since this related directly to the full stage performance and hence to the turbine efficiency. The optimization design sensitivity was evaluated by using a formal quality indicator metric coded in APOW. The results from the optimization and from its sensitivity analysis gave confidence that a good predictive ability was obtained by the Kriging surrogate model used in the design process. The low cost overhead of the Kriging model and its robustness are attractive for accelerating the design iterations used in industry for turbomachines.

Whereas in this work the application of adaptive sampling led to modest improvements in performance with respect to judiciously selected initial sampling, the adaptive sampling technique appears to be an interesting approach in its own right. This approach has the potential to identify more optimal configurations in problems where the response function has greater complexity in shape, a complexity that may not be known *a priori* and that the adaptive sampling should be able to uncover.

One limitation of this work is that it used just one technique, the adaptive sampling approach, for establishing the sensitivity of the stage loss on the parametrized casing shape. Given the relatively small changes in stage loss obtained in the neighbourhood of the optimal shape parameters, the author did not attempt the implementation of any alternative sensitivity analysis process available in literature.

7.3 The implications of the new casing on the stage flow and on the subsequent blade row

An analysis of the predicted flow through the Aachen Turbine was presented to verify the effectiveness of the design in mitigating secondary flow structures and their associated loss. The analysis highlighted the following flow pattern: The incoming boundary layer separated, creating a horseshoe vortex at the blade leading edge. The pressure side arm moved across towards the suction side, merging with the suction side and creating the passage vortex. By delaying the onset of this interaction, reducing the passage vortex size and hence its associated loss were reduced. This was achieved by adding a parametric smooth groove designed by the Beta distribution to guide the horseshoe vortex pressure side arm. Understanding the flow field nature with and without the contoured casing was important to understand how best to control the secondary flows. In general, the new casing design was shows to improve the stator 1 exit flow field by making it more radially uniform and by reducing the overturning close to the casing. That in turns led to an increase in the stage isentropic efficiency. The new design process was shown by steady multi-row 3D RANS modelling to produce aerodynamic performance gains with respect to the equivalent turbine stage with either an axisymmetric casing or with a non-axisymmetric casing designed by a more established controlled diffusion method.

The 3-D flow inside the rotor passage was shown to be characterized by the interaction of secondary flows from stator 1 with the passage vortex and the tip leakage vortex of the unshrouded rotor blade. The results from the entropy distribution and the total pressure loss coefficients indicated a reduction in the tip leakage vortex strength that in turns reduced the local flow over-turning, compared to the equivalent stage with an axisymmetric casing.

7.4 Commercial and environmental impact potentials

The computer-driven process developed in this thesis appeals to the industrial design of turbomachines due to its autonomy, as it required modest user intervention once it was set up. The industry-wide adoption of this technology would have significant economic and environmental impacts. Appendix A provides a first-estimate assessment for the economic and environmental impacts that are within reach. By modelling a representative gas turbine cycle for power generation, sized on a class of turbines in current use, using the commercial software Cycle Tempo, the author was able to provide estimates for the changes in the fuel consumption and in the emissions from this cycle. These appear to be sufficiently attractive for investing in the consolidation of the design processes and of the technology, for treating turbine casing walls, that are proposed in this thesis.

The automated optimization and component performance gains support the growth of the turbomachinery industry, a global business forecast as growing to 4.16 billion US$ in 2020. The savings in fuel consumption and in CO_2 emissions from using a more efficient turbine with the contoured endwall have a good potential for playing an import role to providing a more affordable and sustainable energy supply while progressing towards the United Nations Framework Convention on Climate Change (UNFCCC) emissions targets.

7.5 Further research recommendations

The numerical predictions in this thesis demonstrated the feasibility and potential of the new casing design to reduce the secondary flow losses and hence improve the stage efficiency of axial flow turbine at design and at off design. It is acknowledged that this investigation was limited to one axial turbine and to numerical tests. Some suggestions for further work are now presented, aimed at addressing these limitations.

- The current study should be followed by an experimental research programme, to provide confirmation of the performance gains predicted by CFD. The test rig at RWTH Aachen appears to be a natural choice for such an endeavour.

- The new casing design workflow could be adapted to the equivalent design process of axial compressors. A feasibility study could be performed on the applicability of the surface definition and optimization process to axial compressor designs.

- The flow physics of the contoured casing can be further investigated by performing a time-resolved simulation of the full one and half stage Aachen Turbine. Performing Large Eddy Simulations of the axisymmetric and optimised groove casing should allow further understanding of how the contoured casing works and of its development capabilities. This analysis would complement well the steady RANS numerical investigation presented in this thesis.

- The diffusion casing design was fixed to the same height of 3 mm as the guide groove height, to provide a fair comparison with the new casing design of this work. It is recommended to include the height of the diffusion casing as a design variable with other two design variables suggested in this work, for future design optimization work.

- The current developed design could be combined with fillet radii or, more generally, with three-dimensional blading. This could give further reduction in the secondary flows and hence further improve the performance of the axial turbine.

Appendix A

Casing Treatment Impact on the Thermodynamic Cycle of a Gas Turbine

Gas turbine power generation systems are widely used in Iraq due to their quick start-up and shut-down capabilities. The commercial software Cycle – Tempo is used to evaluate the change in the thermodynamic cycle performance that can be achieved by using power turbines with the new contoured casing of Chapter 3. This is determined by increasing the stage isentropic efficiency of the axial gas turbine that drive the axial compressor in the thermodynamic cycle. This analysis aims to assess any improvements in both the natural gas specific fuel consumption and in the reduction in CO_2 emissions that can be achieved using the axial turbine fitted with the optimized non-axisymmetric casing of Chapter 3.

The simple thermodynamic gas cycle shown in Figure A. 1 is selected to assess the impact of the turbine casing design. This cycle models typical gas power plants in current use, such as SGT5-2000E (Siemens, 2008). This thermodynamic cycle also features in combination with other thermodynamic processes, such as cogeneration and reheat, in hybrid power plants such as combined cycle power plants or solar gas turbine power plants. Recently, Iraq was supplied by GE Power with 56 gas turbines for various projects, which generate about 7600 MW to support the expansion of the country's energy infrastructure and help drive future economic growth (Worldwide, 2016). Thus, the total fuel consumption and CO_2 emissions are going to increase unless these are mitigated by appropriate technological advances that can make the Iraqi energy supply more sustainable.

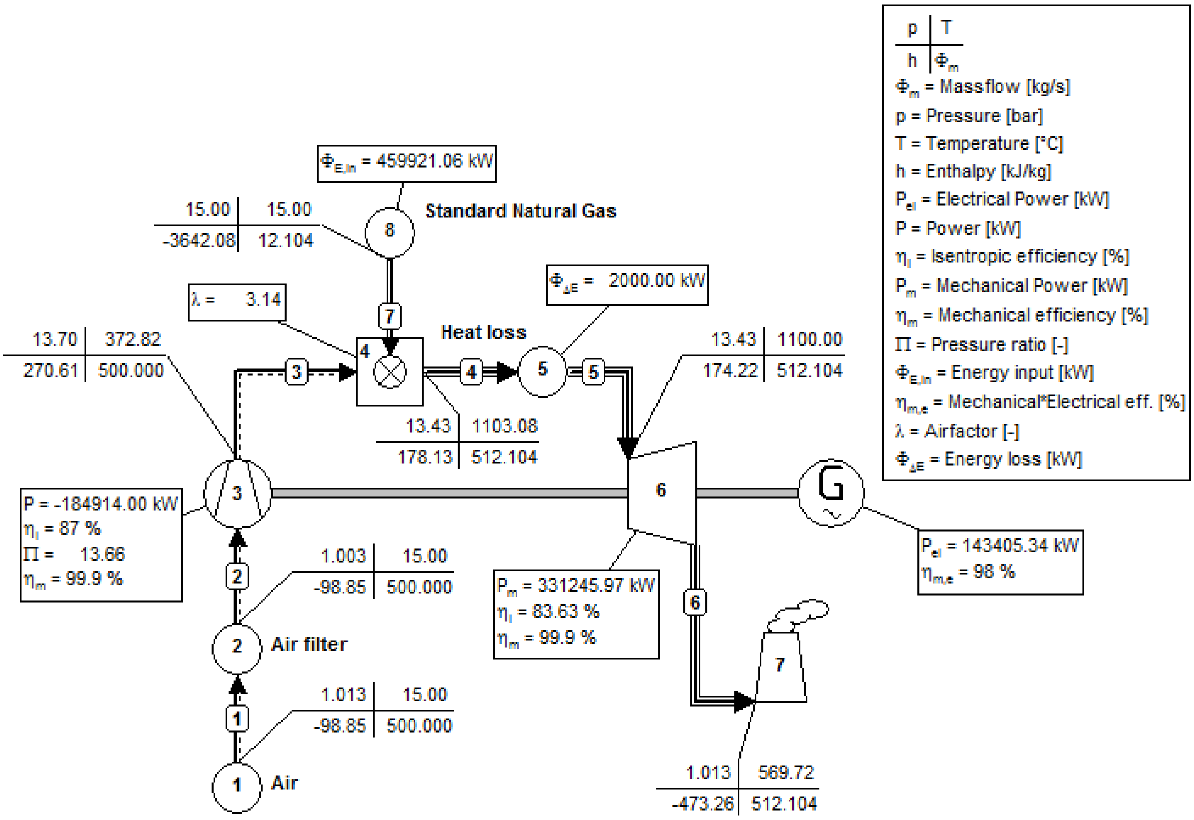

Figure A. 1: Gas turbine cycle with contoured casing at design conditions.

The Aachen Turbine modified by the contoured endwall of Chapter 3 is used for modelling the gas turbine in the cycle schematic of Figure A. 1. The turbine model is run in the cycle at its design condition with a stage isentropic efficiency of 83.63 % and a mechanical efficiency of 99.9 %, which is the same mechanical efficiency used by Woudstra and Van der Stelt (2002). The Natural Gas (NG) is modelled as having the composition of Table A.1, with calorific value of fuel CV_f of 37999 kJ/kg (Woudstra and Van der Stelt, 2002).

Table A. 1

Typical natural gas composition.

Natural gas component	Chemical symbols	Mole Fraction (%)
Nitrogen	N_2	14.32
Oxygen	O_2	0.01
Carbon dioxide	CO_2	0.89
Methane	CH_4	81.29
Ethane	C_2H_6	2.87
Propane	C_3H_8	0.38
i-Butane	C_4H_{10}	0.15
n-Butane	C_5H_{12}	0.04
i-Pentane	C_6H_{14}	0.05

According to the molar chemical balance stated by equation 1, one kmol of fuel generates 0.0328 kmol of CO_2:

$$0.0005\, C_6H_{14} + 0.0004\, C_5H_{12} + 0.0015\, C_4H_{10} + 0.0038\, C_3H_8 + 0.0287\, C_2H_6 + 0.8129\, CH_4 + 0.0089\, CO_2 + 0.0001\, O_2 + 0.1432\, N_2 + Y[0.79\, N_2 + 0.21\, O_2] \rightarrow 0.0328\, CO_2 + 0.0725\, H_2O + 0.1362\, O_2 + 0.7495\, N_2 \quad (1)$$

The thermal efficiency of the cycle in Figure A.1 η_{th} is defined as the ratio of the net work output W_{net} to the total heat supplied Q_f, where $W_{net} = W_{turbine} - W_{compressor}$ and $Q_f = m_f \times CV_f$, where m_f is the mass of the fuel supplied. The specific fuel consumption of a thermal system defined as $SFC = m_f/W_{net}$. Table A. 2 shows a comparison of various performance parameters of the thermodynamic gas cycle with and without the modified turbine. This includes the turbine at design and at off design conditions. Table A. 2 shows that the thermal efficiency of the gas power plant cycle was increased by 3.15 % at design condition by using a contoured endwall. A comparable improvement was obtained at off design conditions, where the thermal efficiency by rose 2.91 %. At design conditions, 1 kg of NG generates 0.077601 kg of

CO_2. As the thermal cycle uses a mass flow rate of fuel of 12.104 kg/s, it emits 0.939277 kg/s of CO_2, equivalent to 29621.05 tonnes of CO_2/year. By reducing the specific fuel consumption by 3.058 %, the corresponding reduction in CO_2 is 906 tonnes of CO_2/year. The modified gas turbine at off design conditions was found to reduce the specific fuel consumption by 2.88 %, which represents a potential reduction in CO_2 of 802.8389 tonnes of CO_2/year.

In conclusion, the gas turbine cycle model presented in this section has shown that improvements in the performance of a simple gas cycle for electrical power generation can be achieved by improving the isentropic efficiency of the axial turbine used in the cycle. The positive implication was a potential reduction in both CO_2 emissions and the amount of the burnt fuel of the gas turbine. The makes a positive contribution towards making the gas turbine cycle more environmentally sustainable, by reducing the pollution from the gas turbine cycle to the atmosphere.

Table A. 2

Comparison of the performance parameters of the gas cycle of Figure A. 1 at design and at off design conditions.

Performance parameters	Design conditions		Off design conditions	
	Standard GTC	Standard GTC with modified turbine	Standard GTC	Standard GTC with modified turbine
Cycle thermal efficiency (%)	30.227	31.18	28.37	29.19
Net work output (kW)	139019.09	143405.3	130479.5	131255.8
Specific fuel consumption (kg/kWh)	0.313442	0.303855	0.3257	0.3164
CO_2 emmsions (tonnes/year)	29621.051	28715.05	28612.97	27810.6

Appendix B

Publications

[1] Kadhim, H., Rona, A., Gostelow, J. P. & Leschke, K. (2018). Optimization of the non-axisymmetric stator casing of a 1.5 stage axial turbine. *International Journal of Mechanical Sciences*, 136, pp. 503-514.

[2] Kadhim, H. T. & Rona, A. (2018). Design optimization workflow and performance analysis for contoured end-walls of axial turbines. *Energy*, 149, pp. 875-889.

[3] Kadhim, H. T. & Rona, A. (2018). Off-design performance of a liquefied natural gas plant with an axial turbine of novel endwall design. *Applied Energy*, 222, pp. 830-839.

[4] Kadhim, H.T., Rona, A., Gostelow, J.P., Leschke, K. Mitigating secondary flows in a 1½ stage axial turbine by a guide groove casing. *The Aeronautical Journal*. Under review.

[5] Kadhim, H. T., Rona, A., Obaida, H. M. & Gostelow, J. P. (2017). Numerical study of the flow past an axial turbine stator casing and perspectives for its management. ASME Turbo Expo 2017: Turbomachinery Technical Conference and Exposition. ASME Paper GT2017-63055.

[6] Kadhim, H.T., Rona, A., Gostelow, J.P., Leschke, K. (2017). Mitigating secondary flows in a1½ stage axial turbine by a guide groove casing. Proceedings of the 23rd ISABE conference, International Society of Air-breathing Engines, paper 22565, Manchester, UK, 03-08 September 2017.

[7] Kadhim, H. T., Rona, A., Obaida, H. M. & Leschke, K. (2017). The Performance of a 1.5 stage Axial Turbine with a Non-Axisymmetric Casing at Off-Design Conditions. Energy Procedia, 142, pp. 1185-1191.

[8] Kadhim, H. T. & Rona, A. (2017). Perspectives on the Treatment of Secondary Flows in Axial Turbines. Energy Procedia, 142, pp. 1179-1184.

References

ACHARYA, S. & MAHMOOD, G. (2006). Turbine Blade Aerodynamics. *The Gas Turbine Handbook.* Morgantown: National Energy Technology Laboratory (NETL)-DOE, pp. 363-390.

AL JUBORI, A., DAABO, A., AL-DADAH, R. K., MAHMOUD, S. & ENNIL, A. B. (2016). Development of micro-scale axial and radial turbines for low-temperature heat source driven organic Rankine cycle. *Energy Conversion and Management*, 130, pp. 141-155.

AL JUBORI, A. M., AL-DADAH, R. K., MAHMOUD, S. & DAABO, A. (2017). Modelling and parametric analysis of small-scale axial and radial-outflow turbines for Organic Rankine Cycle applications. *Applied Energy*, 190, pp. 981-996.

ALSTOM 2014. *The ALSTOM Process & Optimisation Workbench, User Manual*. (version 4.0): GE Power.

ANSYS INC. (2011). *ANSYS FLUENT User's Guide.* Release 14.0.

ARABNIA, M. (2012). *Aerodynamic shape optimization of axial turbines in three dimensional flow.* PhD thesis, Concordia University.

BARIGOZZI, G., FRANCHINI, G., PERDICHIZZI, A. & QUATTRORE, M. (2010). Endwall film cooling effects on secondary flows in a contoured endwall nozzle vane. *Journal of Turbomachinery*, 132(4), pp. 041005-9.

BEAUDOIN, M., NILSSON, H., PAGE, M., MAGNAN, R. & JASAK, H. (2014). Evaluation of an improved mixing plane interface for OpenFOAM. *IOP Conference Series: Earth and Environmental Science*. IOP Publishing, Paper No. 022004.

BENNER, M. W., SJOLANDER, S. A. & MOUSTAPHA, S. H. (1997). Measurements of secondary flows in a turbine cascade at off-design incidence. *International Gas Turbine and Aeroengine Congress and Exhibition: Aircraft Engine; Marine; Turbomachinery; Microturbines and Small Turbomachinery*, USA. ASME Paper 97-GT-382.

BLOXHAM, M. J. & BONS, J. P. (2010). Combined blowing and suction to control both midspan and endwall losses in a turbomachinery passage. *ASME Turbo Expo 2010: Power for Land, Sea, and Air,* USA. ASME Paper GT2010-23552.

BRENNAN, G., HARVEY, N., ROSE, M., FOMISON, N. & TAYLOR, M. (2003). Improving the efficiency of the Trent 500-hp turbine using nonaxisymmetric end walls-Part I: Turbine design. *Journal of turbomachinery*, 125(3), pp. 497-504.

CAO, Z., LIU, B., YANG, X. & LI, M. (2014). The application of 3D blading and non-axisymmetric hub endwall contouring in a dual-stage axial flow counter-rotating compressor. *International Journal of Energy Science*, 4(3), pp. 91.

CFD ONLINE. 2005. Specifying nonuniform boundary condition. *https: //www.cfd-online.com/Forums/openfoam-solving/specifying-nonuniform-boundary-condition*. [Accessed 29.09.2017].

CHEN, Z., QIU, H., GAO, L., LI, X. & LI, P. (2014). A local adaptive sampling method for reliability-based design optimization using Kriging model. *Structural and Multidisciplinary Optimization*, 49(3), pp. 401-416.

CHERNOBROVKIN, A. & LAKSHMINARAYANA, B. (1999). Turbulence modeling and computation of viscous transitional flows for low pressure turbines. *Journal of Fluids Engineering*, 121(4), pp. 824-833.

CHUNG, J., SIMON, T. & BUDDHAVARAPU, J. (1991). Three-dimensional flow near the blade/endwall junction of a gas turbine: application of a boundary layer fence. *ASME 1991 International Gas Turbine and Aeroengine Congress and Exposition*, USA. ASME Paper 91-GT-045.

COULL, J. D. (2017). Endwall loss in turbine cascades. *Journal of Turbomachinery*, 139(8), pp. 081004-12.

DA LIO, L., MANENTE, G. & LAZZARETTO, A. (2016). Predicting the optimum design of single stage axial expanders in ORC systems: Is there a single efficiency map for different working fluids? *Applied Energy*, 167, pp. 44-58.

DENTON, J. D. (1993). The 1993 IGTI Scholar Lecture: Loss Mechanisms in Turbomachines. *Journal of Turbomachinery*, 115(4), pp. 621-656.

DEPARTMENT FOR BUSINESS, E. A. I. S. 2017. Updated energy and emissions projections 2016. London: The UK Department for Business, Energy and Industrial Strategy (BEIS).

DEVORE, J. L. (2015). *Probability and Statistics for Engineering and the Sciences*. USA, Cengage Learning.

DHILIPKUMAR, P. D. (2016). *Effect of endwall fluid injection on passage vortex formation in a first stage nozzle guide vane passage.* MSc thesis, Virginia Polytechnic Institute and State University.

DOSSENA, V., PERDICHIZZI, A. & SAVINI, M. (1999). The influence of endwall contouring on the performance of a turbine nozzle guide vane. *Journal of Turbomachinery*, 121(2), pp. 200-208.

DU, P. & NING, F. (2016). Validation of a novel mixing-plane method for multistage turbomachinery steady flow analysis. *Chinese Journal of Aeronautics*, 29(6), pp. 1563-1574.

DUNN, D., VON BACKSTRÖM, T. & SNEDDEN, G. (2015). An unsteady numerical analysis of a generic non-axisymmetric turbine endwall in a 1½ stage turbine test rig. *The Aeronautical Journal*, 119(1211), pp. 109-119.

ERIKSSON, L., JOHANSSON, E., WOLD, N. K.-., WIKSTRÖM, C. & WOLD, S. (2008). *Design of Experiments: Principles and Applications.* Sweden, Umetrics Academy.

FORRESTER, A. I. & KEANE, A. J. (2009). Recent advances in surrogate-based optimization. *Progress in Aerospace Sciences*, 45(1), pp. 50-79.

FUNAZAKI, K., ENDO, T. & TANUMA, T. (1996). Reduction of secondary flow effects in a linear cascade by use of an air suction from the endwall. *ASME 1996 Turbo Asia Conference,* Indonesia. ASME Paper 96-TA-51.

GALLUS, H. E. & ZESCHKY, J. (1992). Secondary flow and losses in a turbine rotor at off-design conditions. *Cieplne Maszyny Przepływowe (CMP)*, Poland.

GERMAIN, T., NAGEL, M., RAAB, I., SCHÜPBACH, P., ABHARI, R. S. & ROSE, M. (2010). Improving efficiency of a high work turbine using nonaxisymmetric endwalls- part I: Endwall design and performance. *Journal of Turbomachinery*, 132(2), pp. 021007-9.

GIER, J., ARDEY, S., EYMANN, S., REINMÖLLER, U. & NIEHUIS, R. (2002). Improving 3D flow characteristics in a multistage LP turbine by means of endwall contouring and airfoil design modification: Part 2-numerical simulation and analysis. *ASME Turbo Expo 2002: Power for Land, Sea, and Air*, The Netherlands. ASME Paper GT2002-30353.

GOSTELOW, J. P., MAHALLATI, A., CARSCALLEN, W. & RONA, A. (2012). Encounters with vortices in a turbine nozzle passage. *International Journal of Rotating Machinery*, 2012(2012), pp. 1-10.

HADADE, I. & DI MARE, L. (2016). Modern multicore and manycore architectures: Modelling, optimisation and benchmarking a multiblock CFD code. *Computer Physics Communications*, 205, pp. 32-47.

HARTLAND, J. C., GREGORY-SMITH, D. G., HARVEY, N. W. & ROSE, M. G. (1999). Nonaxisymmetric Turbine End Wall Design: Part II-Experimental Validation. *Journal of Turbomachinery*, 122(2), pp. 286-293.

HARVEY, N., BRENNAN, G., NEWMAN, D. & ROSE, M. (2002). Improving turbine efficiency using non-axisymmetric end walls: Validation in the multi-row environment and with low aspect ratio blading. *ASME Turbo Expo 2002: Power for Land, Sea, and Air*, The Netherlands. ASME Paper GT2002-30337.

HARVEY, N. W., ROSE, M. G., TAYLOR, M. D., SHAHPAR, S., HARTLAND, J. & GREGORY-SMITH, D. G. (2000). Nonaxisymmetric turbine end wall design: Part I-Three-dimensional linear design system. *Journal of Turbomachinery*, 122(2), pp. 278-285.

HERMANSON, K. & THOLE, K. (2002). Effect of nonuniform inlet conditions on endwall secondary flows. *Journal of Turbomachinery*, 124(4), pp. 623-631.

HILFER, M., INGRAM, G. & HOGG, S. (2012). Endwall profiling with tip clearance flows. *ASME Turbo Expo 2012: Turbine Technical Conference and Exposition*, Denmark. ASME Paper GT2012-68488.

HU, S. & LUO, H. (2014). Endwall contouring optimization in a high pressure turbine vane with consideration of rim seal flow. *ASME Turbo Expo 2014: Turbine Technical Conference and Exposition*, Germany. ASME Paper GT2014-26587.

HYNDMAN, R. J. & KOEHLER, A. B. (2006). Another look at measures of forecast accuracy. *International Journal of Forecasting*, 22(4), pp. 679-688.

INGRAM, G., GREGORY-SMITH, D. & HARVEY, N. (2005). The benefits of turbine endwall profiling in a cascade. *Proceedings of the Institution of Mechanical Engineers, Part A: Journal of Power and Energy*, 219(1), pp. 49-59.

INGRAM, G., GREGORY-SMITH, D., ROSE, M., HARVEY, N. & BRENNAN, G. (2002). The effect of end-wall profiling on secondary flow and loss development in a turbine cascade. *ASME Turbo Expo 2002: Power for Land, Sea, and Air*, The Netherlands. ASME Paper GT2002-30339.

INGRAM, G. L. (2003). *Endwall profiling for the reduction of secondary flow in turbines.* PhD thesis, Durham University.

JASAK, H. & BEAUDOIN, M. (2011). OpenFOAM Turbo tools: From general purpose cfd to turbomachinery simulations. *ASME-JSME-KSME 2011 Joint Fluids Engineering Conference*, Japan. ASME Paper AJK2011-05015.

KAWAI, T., SHINOKI, S. & ADACHI, T. (1989). Secondary flow control and loss reduction in a turbine cascade using endwall fences. *JSME international journal*, 32(3), pp. 375-387.

KAWASE, M. & RONA A. (2017). Flow structure driven end-wall contouring for a highly loaded axial compressor. Proceedings of the 23rd ISABE Conference, Paper No. 21351, Manchester, UK.

KIM, I., KIM, J., CHO, J. & KANG, Y.-S. (2016). Non-axisymmetric endwall profile optimization of a high-pressure transonic turbine using approximation model. *ASME Turbo Expo 2016: Turbomachinery Technical Conference and Exposition*, South Korea. ASME Paper GT2016-57970.

KULKARNI, A. (2006). *Adaptive sampling based sampling strategies for the DACE surrogate model for expensive black-box functions.* AE 497 B.Tech. Project, Indian Institute of Technology.

KUMAR, K. N. & GOVARDHAN, M. (2011). Secondary flow loss reduction in a turbine cascade with a linearly varied height streamwise endwall fence. *International Journal of Rotating Machinery*, 2011(2011), pp. 1-16.

KUNDU, P. K., COHEN, I. M. & DOWLING, D. R. (2012). *Fluid Mechanics.* Elsevier Inc.

LANGSTON, L. (2001). Secondary flows in axial turbines—a review. *Annals of the New York Academy of Sciences*, 934(1), pp. 11-26.

LUO, J., MCBEAN, I. & LIU, F. (2011). Optimization of endwall contours of a turbine blade row using an adjoint method. *ASME 2011 Turbo Expo: Turbine Technical Conference and Exposition*, Canada. ASME Paper GT2011-46163.

LYNCH, S. P., SUNDARAM, N., THOLE, K. A., KOHLI, A. & LEHANE, C. (2011). Heat transfer for a turbine blade with nonaxisymmetric endwall contouring. *Journal of Turbomachinery*, 133(1), pp. 011019-9.

MA, Z. (2011). *Non-Gaussian statistical models and their applications.* PhD Thesis, KTH - Royal Institute of Technology.

MACKMAN, T., ALLEN, C., GHOREYSHI, M. & BADCOCK, K. (2013). Comparison of adaptive sampling methods for generation of surrogate aerodynamic models. *AIAA Journal*, 51(4), pp. 797-808.

MADAVAN, N. K., RAI, M. M. & HUBER, F. W. (1999). Neural net-based redesign of transonic turbines for improved unsteady aerodynamic performance. *AIAA/SAE/ASME/ASEE 35th Joint Propulsion Conference*, Los Angeles. Paper No. 99–2522.

MCKAY, M. D., BECKMAN, R. J. & CONOVER, W. J. (1979). Comparison of three methods for selecting values of input variables in the analysis of output from a computer code. *Technometrics*, 21(2), pp. 239-245.

MENTER, F., FERREIRA, J. C., ESCH, T. & KONNO, B. (2003). The SST turbulence model with improved wall treatment for heat transfer predictions in gas turbines. *Proceedings of the international gas turbine congress*, Tokyo. Paper No. IGTC2003-TS-059.

MENTER, F. R. (1994). Two-equation eddy-viscosity turbulence models for engineering applications. *AIAA Journal*, 32(8), pp. 1598-1605.

MERONI, A., ANDREASEN, J. G., PERSICO, G. & HAGLIND, F. (2017). Optimization of organic Rankine cycle power systems considering multistage axial turbine design. *Applied Energy*, pp. Article in Press.

MIYOSHI, I., HIGUCHI, S. I. & KISHIBE, T. (2013). Improving the performance of a high pressure gas turbine stage using a profiled endwall. *ASME Turbo Expo 2013: Turbine Technical Conference and Exposition*, USA. ASME Paper GT2013-95148.

MORRIS, M. D. & MITCHELL, T. J. (1995). Exploratory designs for computational experiments. *Journal of Statistical Planning and Inference*, 43(3), pp. 381-402.

MOSER, N., STEINHOFF, P. & JOOS, F. (2013). Experimental and numerical investigations of flowpath profiling on secondary flow losses in a turbine control stage. *ASME Turbo Expo 2013: Turbine Technical Conference and Exposition*, USA. ASME Paper GT2013-94737.

NA, Z. & LIU, B. (2015). Numerical investigation of non-axisymmetric endwalls in a high pressure axial flow turbine. *ASME Turbo Expo 2015: Turbine Technical Conference and Exposition*, Canada. ASME Paper GT2015-42970.

NELDER, J. A. & MEAD, R. (1965). A simplex method for function minimization. *The Computer Journal*, 7(4), pp. 308-313.

NIEWOEHNER, J., POEHLER, T., JESCHKE, P. & GUENDOGDU, Y. (2015). Investigation of nonaxisymmetric endwall contouring and three-dimensional airfoil design in a 1.5 stage axial turbine-Part II: Experimental validation. *Journal of Turbomachinery*, 137(8), pp. 081010-12.

OPENFOAM (2014). *The Open Source CFD Toolbox, User Guide.* Version 2.3.0.

PAHL, G. & BEITZ, W. (2013). *Engineering design: a systematic approach.* New York, Springer Science & Business Media.

PANCHAL, K., ABRAHAM, S., EKKAD, S. V., NG, W., BROWN, B. J. & MALANDRA, A. (2011). Investigation of effect of endwall contouring methods on a transonic turbine blade passage. *ASME 2011 Turbo Expo: Turbine Technical Conference and Exposition*, Canada. ASME Paper GT2011-45192.

PERSICO, G. (2017). Evolutionary optimization of centrifugal nozzles for organic vapours. *Journal of Physics: Conference Series*. IOP Publishing, Paper No. 012015.

PIEGL, L. & TILLER, W. (2012). *The NURBS book.* USA, Springer Science & Business Media.

POEHLER, T., GIER, J. & JESCHKE, P. (2010). Numerical and experimental analysis of the effects of non-axisymmetric contoured stator endwalls in an axial turbine. *ASME Turbo Expo 2010: Power for Land, Sea, and Air*, UK. ASME Paper GT2010-23350.

POEHLER, T., NIEWOEHNER, J., JESCHKE, P. & GUENDOGDU, Y. (2015). Investigation of nonaxisymmetric endwall contouring and three-dimensional airfoil design in a 1.5-stage axial turbine-Part I: Design and novel numerical analysis method. *Journal of Turbomachinery*, 137(8), pp. 081009-11.

POLES, S., FU, Y. & RIGONI, E. (2009). The Effect of Initial Population Sampling on the Convergence of Multi-Objective Genetic Algorithms. *Multiobjective Programming and Goal Programming: Theoretical Results and Practical Applications.* Berlin: Springer Berlin Heidelberg, pp. 123-133.

PRAISNER, T. J., ALLEN-BRADLEY, E., GROVER, E. A., KNEZEVICI, D. C. & SJOLANDER, S. A. (2013). Application of nonaxisymmetric endwall contouring to conventional and high-lift turbine airfoils. *Journal of Turbomachinery*, 135(6), pp. 061006-8.

PUETZ, F., KNEER, J., SCHULZ, A. & BAUER, H.-J. (2015). A new test facility to investigate film cooling on a non-axisymmetric contoured turbine endwall: Part I- Introduction and aerodynamic measurements. *ASME Turbo Expo 2015: Turbine Technical Conference and Exposition*, Canada. ASME Paper GT2015-42272.

QUEIPO, N. V., HAFTKA, R. T., SHYY, W., GOEL, T., VAIDYANATHAN, R. & TUCKER, P. K. (2005). Surrogate-based analysis and optimization. *Progress in aerospace sciences*, 41(1), pp. 1-28.

RAI, M. M., MADAVAN, N. K. & HUBER, F. W. (2000). Improving the unsteady aerodynamic performance of transonic turbines using neural networks. *Proceedings of the 38th AIAA aerospace sciences meeting and exhibit*, USA. NASA/TM-1999-208791.

REIS, A. J. F. (2013). *Validation of NASA rotor 67 with openFOAM's transonic density-based solver.* Nova University of Lisbon, Portugal.

REISING, S. & SCHIFFER, H.-P. (2009). Non-axisymmetric end wall profiling in transonic compressors—part I: Improving the static pressure recovery at off-design conditions by sequential hub and shroud end wall profiling. *ASME Turbo Expo 2009: Power for Land, Sea, and Air*, USA. Volume 7: Turbomachinery, Parts A and B, ASME Paper GT2009-59133.

REUTTER, O., HEMMERT-POTTMANN, S., HERGT, A. & NICKE, E. (2014). Endwall contouring and fillet design for reducing losses and homogenizing the outflow of a compressor cascade. *Proceedings of the ASME Turbo Expo*, Germany. ASME Paper GT2014-25277.

REUTTER, O., HERVÉ, S. & NICKE, E. (2013). Automated optimization of the non-axisymmetric hub endwall of the rotor of an axial compressor. *10th European Conference on Turbomachinery Fluid dynamics & Thermodynamics*, Finland. ETC10, pp. 1-11.

ROACHE, P. J. (1994). Perspective: a method for uniform reporting of grid refinement studies. *Journal of Fluids Engineering*, 116(3), pp. 405-413.

ROSE, M. G. (1994). Non-axisymmetric endwall profiling in the HP NGV's of an axial flow gas turbine. *ASME 1994 International Gas Turbine and Aeroengine Congress and Exposition*, Netherlands. ASME Paper 94-GT-249.

RULLIÈRE, D., DURRANDE, N., BACHOC, F. & CHEVALIER, C. (2016). *Nested Kriging estimations for datasets with large number of observations.*

SAHA, A. K. & ACHARYA, S. (2008). Computations of turbulent flow and heat transfer through a three-dimensional nonaxisymmetric blade passage. *Journal of Turbomachinery*, 130(3), pp. 031008-10.

SANDERS, D., O'BRIEN, W., SONDERGAARD, R., POLANKA, M. & RABE, D. (2009). A mixing plane model investigation of separation and transitional flow at low reynolds numbers in a multistage low pressure turbine. *47th AIAA Aerospace Sciences Meeting including The New Horizons Forum and Aerospace Exposition*, Florida. Paper No. AIAA 2009-1467.

SASENA, M., PARKINSON, M., GOOVAERTS, P., PAPALAMBROS, P. & REED, M. (2002). Adaptive experimental design applied to an ergonomics testing procedure. *ASME DETC Conference*, Canada. ASME Paper DETC2002/DAC-34091.

SASENA, M. J. (2002). *Flexibility and efficiency enhancements for constrained global design optimization with kriging approximations.* PhD thesis, University of Michigan.

SCHOBEIRI, M. (2005). *Turbomachinery flow physics and dynamic performance.* Germany, Springer.

SCHOBEIRI, M. & LU, K. (2014). Endwall contouring using continuous diffusion: a new method and its application to a three-stage high pressure turbine. *Journal of Turbomachinery*, 136(1), pp. 011006-10.

SCHUEPBACH, P., ABHARI, R., ROSE, M., GERMAIN, T., RAAB, I. & GIER, J. (2010). Improving efficiency of a high work turbine using nonaxisymmetric endwalls-Part II: Time-resolved flow physics. *Journal of Turbomachinery*, 132(2), pp. 021008.

SCHÜPBACH, P. (2009). *Influence of rim seal purge flow on the performance of an end wall profiled axial turbine.* PhD thesis, Swiss Federal Institute of Technology (ETH).

SHAHPAR, S., CALONI, S. & DE PRIEAGLLE, L. (2017). Automatic design optimization of profiled endwalls including real geometrical effects to minimize turbine secondary flows. *Journal of Turbomachinery*, 139(7), pp. 071010-11.

SHYY, W., PAPILA, N., VAIDYANATHAN, R. & TUCKER, K. (2001). Global design optimization for aerodynamics and rocket propulsion components. *Progress in Aerospace Sciences*, 37(1), pp. 59-118.

SIEMENS, A. 2008. Siemens Gas Turbines over 100 MW. Germany: Siemens AG, Energy Sector.

SIEVERDING, C. (1985). Recent progress in the understanding of basic aspects of secondary flows in turbine blade passages. *Journal of Engineering for Gas Turbines and Power*, 107(2), pp. 248-257.

SIEVERDING, C. & BOSCHE, V. D. (1983). The use of coloured smoke to visualize secondary flows in a turbine-blade cascade. *Journal of Fluid Mechanics*, 134, pp. 85-89.

SNEDDEN, G. C., DUNN, D. I., INGRAM, G. & GREGORY-SMITH, D. (2010). Performance of a generic non-axisymmetric end wall in a single stage, rotating turbine at on and off-design conditions. *ASME Turbo Expo 2010: Power for Land, Sea, and Air*, UK. ASME Paper GT2010-22006.

SØNDERGAARD, J., MADSEN, K. & NIELSEN, H. B. (2003). *Optimization using surrogate models-by the Space Mapping technique.* PhD thesis, Technical University of Denmark.

SONG, Y., SUN, X. & HUANG, D. (2017). Preliminary design and performance analysis of a centrifugal turbine for Organic Rankine Cycle (ORC) applications. *Energy*, 140, pp. 1239-1251.

SUN, H., LI, J., SONG, L. & FENG, Z. (2014). Non-axisymmetric turbine endwall aerodynamic optimization design: Part I-Turbine cascade design and experimental validations. *ASME Turbo Expo 2014: Turbine Technical Conference and Exposition*, Germany. ASME Paper GT2014-25362.

TALLMAN, J. & LAKSHMINARAYANA, B. (2001a). Numerical simulation of tip leakage flows in axial flow turbines, with emphasis on flow physics: Part I-Effect of tip clearance height. *Journal of Turbomachinery*, 123(2), pp. 314-323.

TALLMAN, J. & LAKSHMINARAYANA, B. (2001b). Numerical simulation of tip leakage flows in axial flow turbines, with emphasis on flow physics: Part II-Effect of outer casing relative motion. *Journal of Turbomachinery*, 123(2), pp. 324-333.

TANG, H., LIU, S. & LUO, H. (2014). Design optimization of profiled endwall in a high work turbine. *ASME Turbo Expo 2014: Turbine Technical Conference and Exposition*. ASME Paper GT2014-26190.

TANG, H., LIU, S., LUO, H. & HOU, W. (2015). Unsteady effects of profiled endwalls on a 1.5 stage axial turbine. *ASME Turbo Expo 2015: Turbine Technical Conference and Exposition*, Canada. ASME Paper GT2015-43871.

TURGUT, Ö. H. & CAMCI, C. (2015). A nonaxisymmetric endwall design approach and its computational assessment in the NGV of an HP turbine stage. *Aerospace Science and Technology*, 47, pp. 456-466.

TURTON, R. K. (2012). *Principles of Turbomachinery.* London, Springer Science & Business Media.

VAN LEER, B. (1979). Towards the ultimate conservative difference scheme. V. A second-order sequel to Godunov's method. *Journal of Computational Physics*, 32(1), pp. 101-136.

WALRAEVENS, R. E. & GALLUS, H. E. 1997. European Reasarch Community on Flow Turbulence and Combustion; ERCOFTAC SIG on 3D turbomachinary flow preditions; Test Case 6: 1-1/2 stage axial flow turbine. *Seminar and Workshop on 3D Turbomachinary flow prediction.* Aachen, Germany.

WANG, H. P., OLSON, S. J., GOLDSTEIN, R. J. & ECKERT, E. R. G. (1997). Flow visualization in a linear turbine cascade of high performance turbine blades. *Journal of Turbomachinery*, 119(1), pp. 1-8.

WANG, S.-S., SUN, H., DI, J., MAO, J.-R., LI, J. & CAI, L.-X. (2014). High-resolution measurement and analysis of the transient secondary flow field in a turbine cascade. *Proceedings of the Institution of Mechanical Engineers, Part A: Journal of Power and Energy*, 228(7), pp. 799-812.

WILCOX, D. C. (1998). *Turbulence modeling for CFD.* 1st Ed. California, DCW industries Inc.

WILCOX, D. C. (2006a). *Companion Software: Turbulence Modeling for CFD.* 3rd Ed., California, DCW Industries, Inc.

WILCOX, D. C. (2006b). *Turbulence Modeling for CFD.* 3rd Ed., California, DCW Industries, Inc.

WORLDWIDE, D. A. G. T. 2016. GE In huge Iraq power deal - Diesel & gas turbine worldwide. https://dieselgasturbine.com/ge-huge-iraq-power-deal. [Accessed 01/11/2017].

WOUDSTRA, N. & VAN DER STELT, T. (2002). Cycle-Tempo: a program for the thermodynamic analysis and optimization of systems for the production of electricity, heat and refrigeration. *Energy Technology Section, Delft University of Technology*, The Netherlands.

YAKHOT, V. & ORSZAG, S. A. (1986). Renormalization group analysis of turbulence. I. Basic theory. *Journal of Scientific Computing*, 1(1), pp. 3-51.

ZHANG, Z., DEMORY, B., HENNER, M., FERRAND, P., ÉD ÉRIC GILLOT, F., BEDDADI, Y., FRANQUELIN, F. & MARION, V. (2014). Space infill study of Kriging meta-model for multi-objective optimization of an engine cooling fan. *ASME Turbo Expo 2014: Turbine Technical Conference and Exposition*, Germany. ASME Paper GT2014-25281.

ZHAO, M. & CUI, W.-C. (2008). Application of the optimal Latin hypercube design and radial basis function network to collaborative optimization. *Journal of Marine Science and Application*, 6(3), pp. 24-32.